KU LEUVEN

ARENBERG DOCTORAL SCHOOL
Faculty of Engineering Technology

UNIVERSITY OF BRASILIA
Faculty of Technology

Fretting fatigue under variable amplitude loading

André Luis Pinto

Supervisors:
Prof. dr. J. A. Araújo
Prof. dr. ir. R. Talemi

Dissertation presented in partial fulfillment of the requirements for the degree of Doctor of Engineering Technology (PhD) from KU Leuven and Doctor of Mechanical Science from University of Brasilia

September 2022

Fretting fatigue under variable amplitude loading

André Luis PINTO

Examination committee:
Prof. dr. T. Doca, chair
Prof. dr. J. A. Araújo, supervisor
Prof. dr. ir. R. Talemi, supervisor
Prof. dr. ir. K. Gryllias
Prof. dr. F. C. Castro
Prof. dr. J. V. Valeo
(Universidad de Sevilla)

Dissertation presented in partial fulfillment of the requirements for the degree of Doctor of Engineering Technology (PhD) from KU Leuven and Doctor of Mechanical Science from University of Brasilia

September 2022

© 2022 KU Leuven – Faculty of Engineering Technology
Uitgegeven in eigen beheer, André Luis Pinto, Gebroeders De Smetstraat 1, B-9000 Ghent (Belgium)

Alle rechten voorbehouden. Niets uit deze uitgave mag worden vermenigvuldigd en/of openbaar gemaakt worden door middel van druk, fotokopie, microfilm, elektronisch of op welke andere wijze ook zonder voorafgaande schriftelijke toestemming van de uitgever.

All rights reserved. No part of the publication may be reproduced in any form by print, photoprint, microfilm, electronic or any other means without written permission from the publisher.

Preface

This thesis dissertation should serve as a comprehensive guideline for fretting fatigue tests under variable amplitude loading. In other words, it focuses on improving the understanding of experimental fretting fatigue tests and numerical methodology for the life assessment of components under variable loading conditions. The primary motivation for this research is the lack of literature on this topic. Although constant amplitudes are almost an exception in real applications and not the rule, few studies have been conducted considering fretting fatigue under variable amplitude loading. This was mainly due to the limitations of the first fretting test apparatus. Therefore, the few existing tests were based on the use of S-N curves generated by fretting fatigue tests performed on one actuator fretting fatigue device (thus bulk and fretting loads are coupled), the use of Miner's damage rule, and uniaxial fatigue analysis to estimate life. Recent advances in the experimental area have allowed for tests with more complex loading configurations. This motivated the realization of this work. The current Ph.D project aims to carry out a comprehensive set of fretting fatigue tests under variable amplitude loading. So that could be possible to study the effects of the loading sequence on the total life and propose a robust numerical approach capable of accurately estimating the life.

From a more personal point of view, this work represents the individual efforts of a researcher in search of his personal and intellectual development, however, supported and encouraged mainly by his advisors. The thesis can be considered as the compilation of the main findings made throughout the entire doctorate. The publications that are part of this manuscript are the result of a progressive evolution that played an imperative role in my personal development. The exposure and analysis of the main physical phenomena involved in this study were only possible due to the established proficiency in numerical modeling, and the ability to perform tests such as traction, fatigue, crack propagation, and fretting fatigue. In addition, it can be said that all models and numerical predictions were verified and validated with our experimental data or the ones available in the literature. This contributes to the authenticity and reliability of the work presented.

Firstly, I would like to express my sincere gratitude to several people without whom this work would not have been possible. In particular, my supervisors: José Alexander Araújo and Reza Talemi for enabling, conceptualizing, and reviewing this research. Next, I would like to thank my colleagues: Gabriel M. J. Almeida and Raphael A. Cardoso for their collaboration and assistance in the experimental and numerical works respectively. Of course, I strongly appreciate the support and patience of my friends and family, especially my parents José Luis Pinto and Alíce Araújo Graciano Pinto, my brother José L. P. Júnior and sister-in-law Jaqueline P. S. Pinto, and our little Dimitri who just arrived. Above all, I thank God for the opportunity to live this experience and leave my share of contributions to science. I would also like to dedicate this work to my grandfather Armando D. Graciano and one of my biggest supporters who unfortunately left us this year, my dear grandmother Marina Araújo Graciano.

Abstract

Generally, the fretting fatigue problem is treated with constant amplitude loading. However, this condition is not the reality for industrial applications. Although there are few studies on fretting fatigue under variable amplitude loadings, they use a simplistic approach to life estimation (unable to capture the effects of the complex multiaxial and non-proportional stress field that exists under the contact interface) and only the bulk fatigue load has its amplitude alternating. The objective of this work is to propose a numerical methodology for the life assessment of components subjected to fretting fatigue under variable amplitude loading and to study the effects of these loads. For this, experimental tests were carried out by applying H-L (High-Low) and L-H (Low-High) loading blocks to the tangential load, that is, the contact normal load and the amplitude of the bulk fatigue load were kept constant while the tangential load has its alternating amplitude. The numerical methodology proposed for fretting fatigue life assessment includes the wear effect and crack propagation. The multiaxial fatigue parameter SWT, the theory of critical distance TCD, and Miners' linear rule were used to compute the damage in the crack nucleation phase. The node-displacement algorithm based on Archard's law was applied to account wear. In the crack propagation phase, the CDM (critical direction method) was used to estimate the crack initiation angle considering the worn contact surface, and then the crack is modeled and propagated. The still limited range of experimental data done in this work for fretting fatigue under varying loading blocks seems to indicate that the loading sequence has an effect on the accumulated fatigue damage, mainly to the H-L loading sequences. Based on this observation, a new non-linear damage model was proposed. Using this new damage model, the life estimation results were within a scatter band of 1.2.

Beknopte samenvatting

In het algemeen wordt het probleem van fretting-vermoeidheid behandeld met constante amplitudebelasting. Deze voorwaarde is echter niet de realiteit voor industriële toepassingen. Hoewel er weinig studies zijn over fretting-vermoeidheid onder variabele amplitudebelastingen, gebruiken ze een simplistische benadering van de schatting van de levensduur (niet in staat om de effecten van het complexe multiaxiale en niet-proportionele spanningsveld dat bestaat onder de contactinterface vast te leggen) en alleen de bulkmoeheidsbelasting heeft zijn amplitude alternerend. Het doel van dit werk is om een numerieke methodologie voor te stellen voor de beoordeling van de levensduur van componenten die onderhevig zijn aan wrijvingsmoeheid onder variabele amplitudebelasting en om de effecten van deze belastingen te bestuderen. Hiervoor werden experimentele tests uitgevoerd door H-L (High-Low) en L-H (Low-High) belastingsblokken toe te passen op de tangentiële belasting, dat wil zeggen de contactnormale belasting en de amplitude van de bulkmoeheidsbelasting werden constant gehouden terwijl de tangentiële belasting heeft zijn wisselende amplitude. De numerieke methodologie die wordt voorgesteld voor de beoordeling van de levensduur van de wrijvingsmoeheid omvat het slijtage-effect en de scheurvoortplanting. De multiaxiale vermoeidheidsparameter SWT, de theorie van de kritische afstand TCD en de lineaire regel van Miners werden gebruikt om de schade in de scheurnucleatiefase te berekenen. Het knooppuntverplaatsingsalgoritme op basis van de wet van Archard werd toegepast op accountwear. In de scheurvoortplantingsfase werd de CDM (critical direction method) gebruikt om de scheurinitiatiehoek te schatten, rekening houdend met het versleten contactoppervlak, en vervolgens wordt de scheur gemodelleerd en gepropageerd. De nog steeds beperkte reeks experimentele gegevens die in dit werk zijn gedaan voor fretting-vermoeidheid onder variërende blokbelasting lijkt erop te wijzen dat de laadvolgorde een effect heeft op de geaccumuleerde vermoeidheidsschade, voornamelijk op de H-L-laadsequenties. Op basis van deze observatie werd een nieuw niet-lineair schademodel voorgesteld. Met behulp van dit nieuwe

schademodel lagen de resultaten van de schatting van de levensduur binnen een spreidingsband van 1,2.

Abbreviations

ASTM	American Society for Testing and Materials
CDM	Critical Direction Method
CMOD	Crack-mouth-opening displacement
COF	Coefficient of friction
FEM	Finit Element Method
FS	Fatemi-Socie parameter
GNP	Gross National Product
HCF	High Cycle Fatigue
LEFM	Linear Elastic Fracture Mechanics
LM	Line Method of TCD
LVDT	Linear variable differential transformer
MERR	Maximum Energy Release Rate criterion
MTS	Maximum Tangential Stress criterion
PM	Point Method of TCD
PSBs	Persistent Slip Bands
SIF	Stress intensity factor
SWT	Smith, Watson and Topper parameter
TCD	Theory of Critical Distance
XFEM	eXtended Finite Element Method

Nomenclature

a	Contact semi-width/Crack size
a_i	Initial crack size
a_f	Final crack size
A	Material constants of L_M equation
α	Energy wear coefficient
b	Fatigue strength exponent
$b^{'}$	Fatigue strength exponent in torsion
B	Bulk fatigue load/Material constants of L_M equation
β	Exponent of the numerical damage rule
c	Semi-width of the stick zone/Fatigue ductility exponent
$c^{'}$	Fatigue ductility exponent in torsion
C	Paris' linear coefficient of the straight section
C_{ij}	Direction-dependent coefficients
dh	Material removal depth
ds	Incremental relative slip/Length increment along the contour Γ
da/dN	Crack growth rate
da	Crack incremental size
d_1	Damage generated in the first block
$D_{f,n}(\mathbf{x})$	Total cumulative damage
δ	Local slip amplitude
δ_{1i}	Kronecker delta
e	Offset of the stick zone
E	Young's modulus of elasticity
E^*	Effective modulus of elasticity
E_1,E_2	Young modulus of the bodies coming into contact
E_d	Friction energy dissipated
$E_{d,max}$	Maximum friction energy dissipated
ε	Strain of the material
$\varepsilon_f^{'}$	Fatigue ductility coefficient
ε_x,ε_y,ε_z	Strain in the x, y, and z-axis directions

ε_{ij}	Strain tensors
$\varepsilon_n(\theta, t)$	Average normal strain for a given θ line at the time t
$\bar{\varepsilon}_{n,a}(\theta)$	Maximum normal strain range for a given θ direction
$\Delta\varepsilon_1$	Maximum range of principal strain
f	Coefficient of friction
f_m	Mean coefficient of friction
f_s	Coefficient of friction for the slip zones
f_{ij}	Shape function
$F_\alpha(x)$	Elastic asymptotic cracktip functions
F	Shape factor
F_1,F_2,F_3	Generic loads applied in a material
G	Shear modulus
G_e, G^k	Energy release rate
γ_{xy},γ_{xz},γ_{yz}	Shear strain in the xy, xz, and yz-plane
$\gamma_f^{'}$	Shear fatigue ductility coefficient
Γ	Arbitrary counterclockwise path
$\Delta\gamma_{max}$	Maximum shear strain range
H	Material hardness
$H(x)$	Discontinuous jump function
J	J-integral
J_{Ic}	J-Integral Fracture Toughness
K	Stress intensity factor
$K1$	Ruiz fretting wear parameter
$K2$	Ruiz fretting fatigue parameter
K_I,K_{II},K_{III}	Stress intensity factor in mode I, II, and III
K_{Ic}	Plane strain fracture toughness
K_{max}	Maximum stress intensity factor
K_c	Critical stress intensity factor
K_{eq}	Stress intensity factor equivalent
K_I^k,K_{II}^k	K with infinitesimally small crack direction
K	Dimensionless wear coefficient
k_2	Material constant used in FS paramete
k_w	Local wear coefficient
ΔK	Stress intensity factor range
ΔK_{eq}	Stress intensity factor range equivalent
ΔK_{th}	Threshold stress intensity factor range
L	Critical distance for HCF
L_s	Critical distance static strength
L_M	Critical distance at medium-high cycle fatigue
m	Slope coefficient of the Paris' equation
m_i	Outward normal vector on path Γ^*
n_1,n_2	Number of cycles applied in each loading block

$\mathbf{n}$	Normal vector
n_i	Number of cycles applied with an σ_a
n_j	Components of the unit vector normal to Γ
N_1	Experimentally observed live for the high loading block
N_2	Experimentally observed live for the low loading block
N_i	Crack nucleation life
N_p	Crack propagation life
N_0	Initial guess life to estimate L_M
N_h	Estimated life of the High block
N_l	Estimated life of the Low block
N_f	Number of cycles to failure
$N_{f,i}$	Fatigue life expected for a given stress state
$N_{f,e}$	Numerical estimated life
$N_I(x)$	Nodal shape functions for conventional FE formulation
$N_J(x)$	Nodal shape functions for q_j^0
$N_K(x)$	Nodal shape functions for q_k^α
ΔN	Jumping factor
ν	Poisson's modulus
ν_1,ν_2	Poisson's ratio of the bodies coming into contact
O	Origin of coordinates in the plane
$p(x)$	Pressure distribution between two cylindrical contact
p_0	Peak pressure
P	Normal load
ϕ	Angle between the z and x' axis
$\phi(z)$	Muskhelishvili's potential
q	Weight function in the area A^*
q_j^0	Nodal enriched degree of freedom vector
q_k^α	Nodal enriched degree of freedom vector
$q(x)$	Tangential traction
Q	Tangential load
Q_1	Tangential load applied in the first block
Q_2	Tangential load applied in the second block
Q_a	Tangential load applied
Q_{max}	Maximum tangential load
Q_{min}	Minimum tangential load
r	Distance close to the crack tip
R	Loading ratio
R_p	Pad radius
R^*	Effective contact radius
R_1,R_2	Radius of the bodies coming into contact
S	Total relative slip
S_y	Yield strength

S_c	Set of nodes surrounding the crack tip
S_{ut}	Ultimate tensile strength
S_A	Set of all nodes in the FE mesh
S_H	Nodes whose supports are cut by the crack (excluding S_c)
σ	Stress
σ_x,σ_y,σ_z	Stress in the x, y, and z-axis directions
σ_n	Normal stress
σ_r	Reference material constant
σ_b	Bulk fatigue stress
σ_a	Stress amplitude
σ_m	Mean stress
σ_r	Radial stress component
σ_θ	Tangential stress component
$\sigma_{b,1}$,$\sigma_{b,2}$,$\sigma_{b,3}$	Bulk fatigue load applyed in each loading block
$\sigma^{'}_{f}$	Fatigue strength coefficient
σ_{ij}	Stress tensor
$\sigma_{n,max}$	Maximum normal stress
$\sigma_{ij}(r,\theta)$	Stress distribution in the area near the crack tip
σ^0_{ij}	Finite stresses at the crack tip
$\sigma_{\theta\theta}$	Stress field for polar coordinates
σ_{eff}	Effective stress
σ_{max}	Maximumm stress
$\sigma_n(\theta,t)$	Average normal stress for a given θ line at the time t
$\bar{\sigma}_{n,max}(\theta)$	Maximum normal stress range
$\Delta\sigma_{-1}$	Uniaxial plain fatigue limit range (R=-1)
t	Time
$\mathbf{t}$	Cauchy stress vector
$\mathbf{t}_n$	Normal stress vector
T	Period
$\mathbf{T}$	Stress tensor
T_i	Traction vector
τ	Shear stress
τ	Shear stress vector
τ_{max}	Maximum shear stress
τ_{xy},τ_{xz},τ_{yz}	Shear stress in the xy, xz, and yz-plane
$\tau^{'}_{f}$	Fatigue strength coefficient in shear
$\tau_{r\theta}$	Shear stress field for polar coordinates
θ	Angle between the x and z' axis/Crack direction
θ_p	Crack propagation angle
u_i	Displacement vector
u_I	Nodal displacement vector
$u^h(x)$	Nodal displacement for XFEM formulation

V	Volume of material removed
x',y',z'	New generic coordinate system
w	Strain energy density
ζ	Stabilization parameter

Contents

Abstract iii

Beknopte samenvatting v

Abbreviations vii

Nomenclature ix

Contents xv

List of Figures xix

List of Tables xxv

1 Introduction and literature review 1
- 1.1 Fretting fatigue . . . 2
  - 1.1.1 Review of the state of the art on fretting fatigue under variable amplitude loading . . . 4
- 1.2 Objectives . . . 7
- 1.3 Thesis scope and methodology . . . 8

2 Background knowledge 11
- 2.1 Fatigue . . . 12
  - 2.1.1 The physical nature of fatigue damage . . . 12
  - 2.1.2 Fatigue aproaches . . . 14
- 2.2 Multiaxial fatigue life assessment . . . 16
  - 2.2.1 Stress components relative to a generic material plane . 17
  - 2.2.2 Smith, Watson and Topper parameter (SWT) . . . 19
  - 2.2.3 Fatemi-Socie parameter (FS) . . . 20
- 2.3 Fracture mechanics . . . 21
  - 2.3.1 Modes of fracture . . . 22

2.3.2 Crack tip stress and displacement fields 23
2.3.3 J-integral 25
2.3.4 Fatigue crack propagation 26
2.3.5 Crack propagation direction 29
2.4 Computational Fracture Mechanics 31
2.4.1 The energy domain integral 32
2.4.2 XFEM principles 34
2.5 Theory of Critical Distance (TCD) 36
2.6 Contact mechanics 37
2.6.1 Surface tractions distributions 38
2.6.2 Bulk load effect on the shear traction distribution . . . 41
2.6.3 Sub-surface stress distributions 43
2.7 Wear modelling and damage accumulation 45
2.7.1 Wear model 45
2.7.2 Damage accumulation method 46

3 Experimental work 51
3.1 Material characterization 52
3.1.1 Aluminum alloy 7075-T651 52
3.1.2 Metallographic analysis 52
3.1.3 Hardness Test 54
3.1.4 Tensile tests 55
3.1.5 Fatigue Test 57
3.1.6 Curve da/dN vs ΔK and ΔK_{th} 60
3.2 Fretting fatigue tests 64
3.2.1 Experimental set-up 64
3.2.2 Test procedure 65
3.2.3 Measuring the coefficient of friction - COF 69
3.2.4 Experiments observations and results 71
3.3 Fretting fatigue data available in the literature 77
3.3.1 Al 7075-T651 78
3.3.2 Al 2024-T3 79
3.3.3 Al 7050-T7451 80

4 Effects of fretting wear process on fatigue crack propagation and life assessment 85
4.1 Overview 86
4.2 Methodologies to fretting fatigue life assessment 87
4.3 Numerical aspects 88
4.3.1 Critical distance application 88
4.3.2 Multiaxial fatigue parameter calibration 88
4.3.3 Wear modeling and damage accumulation 92
4.3.4 Crack propagation direction 93

4.3.5 Numerical model and boundary conditions 96
4.4 Results and discussions 96
4.4.1 Validation of the XFEM method for crack propagation . 96
4.4.2 Comparison between different crack path prediction methods 99
4.4.3 Application of XFEM and SWT_L method for crack propagation life and path estimation 101
4.4.4 Effects of fretting wear process on fatigue crack propagation 105
4.4.5 Results using the critical distance as a function of life . 110

5 Early crack orientation prediction methods under fretting fatigue loading including wear effects 117
5.1 Overview 118
5.1.1 Multiaxial fatigue parameter calibration 119
5.2 Methodology 120
5.2.1 Method 1: Critical Direction Method 122
5.2.2 Method 2: Method based on LEFM 123
5.2.3 Numerical model and boundary conditions 126
5.3 Results and discussions 126

6 Fretting fatigue under variable amplitude loading considering partial slip regime: numerical analysis 131
6.1 Overview 132
6.2 Numerical methodology 132
6.2.1 Summary 133
6.2.2 Numerical model and boundary conditions 135
6.3 Materials and fatigue parameter calibration 136
6.4 Results and discussions 138
6.4.1 L in function of life: -a vs D_{max} 138
6.4.2 Life estimation: High and Low blocks 140
6.4.3 Life estimation: H-L and L-H loading sequences 143

7 Conclusions 147
7.1 Overview 148
7.2 Effects of fretting wear process on fatigue crack propagation and life assessment 149
7.3 Early crack orientation prediction methods under fretting fatigue loading including wear effects 151
7.4 Fretting fatigue under variable amplitude loading considering partial slip regime: Experimental and numerical analysis 152
7.5 Future work 154
7.5.1 Numerical modelling 154
7.5.2 Experimental 154

A Technical drawing of specimens **157**

Bibliography **163**

Curriculum Vitae **179**

Publications **181**

A.1 A1 - Peer reviewed journal publications 181
A.2 P1 - Peer reviewed Publications in conference proceedings . . . 181
A.3 C1 - Publications in conference proceedings 182

List of Figures

1.1 Short caption for Table of Figures 3

2.1 Schematic representation of slip band formation [149]. 13
2.2 Stage I/Stage II growth process [149]. 14
2.3 S-N curve for unnotched specimens of a steel [49]. 15
2.4 Elastic, plastic, and total strain versus life curves [49]. 16
2.5 Body subjected to an external system of forces. [153]. 17
2.6 Equilibrium condition applied to the Cauchy tetrahedron. F_1; F_2; F_3 are generic loads applied to the outer faces [3]. 19
2.7 Stresses acting on a plane in a three dimensional coordinate system [149]. 20
2.8 Physical basis of the SWT (a) and FS (b) model [149]. 21
2.9 Fracture modes, from right to left mode I, mode II and mode III, respectively. 22
2.10 Crack tip stress field. 24
2.11 Schematic comparison of the stress-strain behavior of elastic-plastic and nonlinear elastic materials [4]. 26
2.12 Arbitrary contour around the tip of a crack [4]. 27
2.13 Scheme of the da/dN vs ΔK curve. 27
2.14 Degeneration of a quadrilateral element into a triangle at the crack tip [4]. 32
2.15 Inner and outer contours, which form a closed contour around the crack tip when connected by Γ_+ and Γ_- [4]. 33
2.16 Normal and tangential coordinates for a smooth crack using XFEM. 35
2.17 Schematic representation of the Point Method. 37
2.18 Schematic representation of the cylinder on plane contact configuration. 39
2.19 Variation of the tangential load Q over time. 41
2.20 Shear traction distributions during a tangential cycle, $Q_{max}/fP = 0.6$. 42

2.21 Shear traction distributions during a fretting cycle, $Q_{max}/fP = 0.6$ and $\sigma_{b,max}/fp_0 = 0.8$. 43
2.22 Illustration of the strategy used in order to compute the damage considering wear process: (a) accumulated damage at the centroid of the elements at the $(i-1)^{th}$ simulated fretting cycle, (b) incremental damage at the centroid of the elements at the i^{th} simulated fretting cycle, (c) accumulated damage at the $(i-1)^{th}$ simulated fretting cycle extrapolated to the position of the element centroids at the i^{th} simulated fretting cycle and (d) accumulation of the total damage at the i^{th} simulated fretting cycle. 48
2.23 Damage accumulation procedure considering wear. 49

3.1 Al 7075-T651 alloy samples embedded in resin. 52
3.2 Three-dimensional image formed with metallography in each lamination direction (T, S, and L). 53
3.3 Micrograph of Aluminum Alloy 7075-T651, in L (a), S (b), and T (c) direction at 200x increase. 54
3.4 Durometer Zwick Roell ZHU 250. 54
3.5 Servo hydraulic machine MTS 810. 55
3.6 Fatigue and tension test specimen. 56
3.7 Extensometer attached to the specimen during the tensile test. 56
3.8 $\sigma - \varepsilon$ diagram of Al 7075-T651 alloy. 57
3.9 Photo of the axial-torsional MTS 809 servo-hydraulic test rig. . 58
3.10 Al 7075-T651 alloy S-N curve. 58
3.11 Al 7075-T651 alloy τ-N curve. 59
3.12 Apparatus for testing compact specimens. 61
3.13 Picture of the compact tension specimen. 61
3.14 Measurement of the crack-mouth-opening displacement with a clip gage [4]. 62
3.15 Curve da/dN vs ΔK 62
3.16 Curve da/dN vs ΔK to obtain the ΔK_{th}. 63
3.17 Schematic of the four actuators fretting fatigue rig [1]. 65
3.18 Photos of the four actuators fretting fatigue rig (a), and fretting apparatus(b). 66
3.19 The dog-bone specimen (a), and fretting pad (b) used for fretting fatigue tests. 66
3.20 Fretting fatigue contact alignment analysis using pressure film: the well aligned (a) and misaligned contact (b) between fretting pad and fatigue specimen. 67

3.21 Schematic representation of the application of loads in the fretting fatigue test: (a) representation of where each load is applied to the specimen, (b) order of application of test loads, and the representation of the H-L (c) and L-H (d) loading blocks. . . . 68
3.22 Test methodology to determine the mean coefficient of friction. 70
3.23 Experimental fretting fatigue lives of the H-L (a) and L-H (b) loading blocks. 73
3.24 Estimated and observed fretting fatigue lives under variable loading conditions. 74
3.25 Fretting scar of the fretting fatigue specimens FF2 [H] (a) and FF19 [L-H] (b). 75
3.26 The fracture surface of the fretting fatigue specimens FF2 (a) and FF19 (b). 76
3.27 The three-dimensional fracture surface of the fretting fatigue specimen FF19 (dimensions in mm). 77
3.28 Methodology of fretting crack path and initiation angle measurement. 78
3.29 Crack propagation path of fretting fatigue specimens FF2, FF5, FF8, and FF19. 78
3.30 Uniaxial fatigue data for the Al 2024-T351 [120]. 81
3.31 Schematic of tests loading history. 82
3.32 Uniaxial fatigue data of Al 7050-T7451 [90]. 83

4.1 Flowchart of the third method for fretting fatigue life assessment. 89
4.2 Procedure to estimate the critical distance L_M: (a) definition of the critical distance L_M and (b) flowchart of the algorithm for fatigue life calculation. 90
4.3 Process of calibration of uniaxial fatigue data (Al 2024-T351 [120]) for crack nucleation life estimation. 91
4.4 Uniaxial fatigue data for the Al 2024-T3 expressed in terms of the SWT parameter: total failure (a) and nucleation life (b). . 92
4.5 Uniaxial fatigue data for the Al 2024-T3 expressed in terms of the FS parameter: total failure (a) and nucleation life (b). . . . 92
4.6 FE-based model for wear analysis using the moving node technique. 93
4.7 Illustration of the strategy used to $(SWT_{mean})_{max}$. 94
4.8 Illustration of the strategy used to SWT_L. 95
4.9 FE model for the fretting fatigue problem. 97
4.10 Loading scheme. 97
4.11 Cracked plate under tension (a) and crack modeling with XFEM(b). 98
4.12 Time variation of K_I (a) and K_{II} (b). 98
4.13 Analytical vs numerical stress intensity factor (a) and numerical results of the stress field at the crack tip (b). 99

4.14 Comparing the estimated crack propagation path using different criteria and the experimental observation. 100
4.15 Convergence analysis using different mesh size: crack path (a) and Stress Intensity Factor variation (b). 101
4.16 Life estimation using different mesh size. 102
4.17 Crack propagation trajectory (a) and Variation of the crack length versus crack propagation life time (b) for FF1–FF9. . . . 103
4.18 Variation of normalized equivalent SIFs versus the crack length for FF1–FF9 (a) and Estimated percentage of fretting fatigue crack initiation and propagation lifetime (b). 103
4.19 The energy dissipated along the surface contact for FF1-FF9. . 105
4.20 Estimated and observed fretting fatigue lives without and with crack propagation. 106
4.21 Comparison between surfaces (a) and normal pressure distribution (b) after wear process to FF4 test. 106
4.22 Comparison between crack path (a) and crack propagation life (b) after wear process to FF4 test. 107
4.23 Estimated and observed fretting fatigue lives without and with crack propagation including wear effect. 108
4.24 Correlation between maximum energy dissipated with life prediction error. 110
4.25 Correlation between maximum energy dissipated normalized with life prediction error. 111
4.26 Comparison between surfaces worn from FF1 to FF5 (a) and from FF6 to FF9 tests (c), normal pressure distribution from FF1 to FF5 (b), and from FF6 to FF9 tests (d). 112
4.27 Crack path without wear (a) and with wear effects (b). 113
4.28 Crack propagation life without wear (a) and with wear effects (b). 113
4.29 Fretting fatigue life assessment for tests FF1-FF9 with fixed (a), and variable (b) critical distance. 114

5.1 Calibration procedure to represent uniaxial fatigue data (Al 7050-T7451 [90]) in terms of crack initiation lifetime. 121
5.2 SWT parameter calibrated for crack initiation life. 121
5.3 Schematic representation of CDM at the contact trailing edge: (a) without wear and (b) with wear. Positive θ angles in the counterclockwise direction. 123
5.4 Schematic representation of Method 2 at the contact trailing edge: (a) without wear and (b) with wear. Positive θ angles in the counterclockwise direction. 124
5.5 Schematic representation of stresses near the crack tip. 125
5.6 Wear results for each test configuration: (a) worn surface and (b) normal pressure distribution. 127

5.7 Crack angle prediction for tests C2 (a), C3 (b) and C4 (c). . . 130

6.1 Flowchart of the numerical method proposed for estimating the life of components subjected to fretting fatigue. 134
6.2 Schematic representation of the load application sequence. . . . 135
6.3 Process of calibration of uniaxial fatigue data for crack nucleation life: Al 7075-T651. 137
6.4 Uniaxial fatigue data for the Al 7075-T651 expressed in terms of the SWT parameter: total failure (a) and nucleation life (b). . 137
6.5 Variation of the critical distance along the cycles. 139
6.6 Stress gradient at the trailing edge of the contact, -a: distribution of σ_x inside of the material. 139
6.7 Pad and specimen profile before and after wear: High block (a) and Low block (b). 140
6.8 Stress distribution of High block: without wear (a) and with wear (b). 141
6.9 Crack propagation path (a) and life (b) prediction for High and Low blocks. 142
6.10 Evolution of ΔK_{eq} as the crack grows. 142
6.11 Expected results using the Numerical rule for sequences H-L (a) and L-H (b). 144
6.12 Estimated and observed fretting fatigue lives under variable amplitude loading condition: comparison between Miner's rule and Numerical damage model. 144

A.1 Technical drawing of fatigue specimen. 158
A.2 Technical drawing of compact tension specimen. 159
A.3 Technical drawing of fretting fatigue specimen. 160
A.4 Technical drawing of pad used in fretting fatigue test. 161

List of Tables

3.1 Chemical composition of Aluminum Alloy 7075-T651 (%weight) (ASM International). 52
3.2 Mechanical properties of AL 7075-T651. 57
3.3 Results from uniaxial fatigue tests. 59
3.4 Results from pure torsion fatigue tests. 60
3.5 Results from crack propagation tests. 63
3.6 Coefficients of friction for the Al 7075-T651 alloy under fretting conditions with a constant normal load. 71
3.7 Loading configuration of the blocks High and Low. 71
3.8 Fretting fatigue lives of the loading block individually (High and Low blocks). 71
3.9 Loading configuration of the tests H-L and L-H. 72
3.10 Fretting fatigue tests under H-L loading sequence. 72
3.11 Fretting fatigue tests under L-H loading sequence. 73
3.12 Initial crack angle observed for the crack size of $2L$. 77
3.13 Mechanical properties of Al7075-T651 [167]. 79
3.14 Mechanical properties of Al2024-T3 [84]. 80
3.15 Test conditions of fretting fatigue experiments [84]. 80
3.16 Monotonic and cyclic properties of 7050-T7451 aluminum alloy. . 81
3.17 Loading and geometry configurations of fretting experiments. . 82
3.18 Crack orientation measured for all tests. 83

4.1 Result of life assessment: with and without take wear into account, checking the influence of wear in N_i and N_p. 109
4.2 Fretting fatigue life assessment for tests FF1-FF9. 115
4.3 Percentage of the total fatigue life related to the crack initiation phase. 115
4.4 Life estimation error, the mean and standard deviation of the error. 116

5.1 Crack nucleation life prediction for tests C1-C8. 127
5.2 Crack angle prediction for all tests using Methods 1 and 2. . . 129

6.1 Al 7075-T651 properties. 136
6.2 Crack nucleation life and crack initiation angle estimated for blocks High and Low. 141
6.3 Numerical life estimation for High and Low blocks. 143
6.4 Numerical life estimation using Miner and Numerical damage rule compared with experimental results. 145

Chapter 1

Introduction and literature review

“The first chapter presents a brief introduction of fretting fatigue under variable amplitude loading and address the objectives of this thesis”

Some parts of the text in this chapter was previously published as:
PINTO, André Luis, et al. Fretting fatigue under variable amplitude loading considering partial and gross slip regimes: Numerical analysis. Tribology International, 2020, 146: 106199.

1.1 Fretting fatigue

In recent decades the phenomenon/mechanism of failure known as fretting has been extensively investigated. Fretting occurs when two contacting parts are subjected to fluctuating loads, provoking a relatively small amplitude slip between them. Strong stress gradients and wear due to the contact loads may lead to the early initiation of cracks. In this case, in the presence of bulk fatigue loads, one has the so-called fretting fatigue phenomenon. Under such conditions, initiated cracks may propagate at high rates resulting in strong fatigue resistance reductions [99]. Fretting fatigue takes place in many practical situations such as gears, aircraft fuselages, the connection between rotor and blades in jet engines, flanges, bolted joints in pipelines and overhead conductors [141, 173, 8, 15]. Fretting fatigue studies and tests have been carried under constant amplitude loads [128, 135, 116, 59]. However, in practice, under actual working conditions, components such as the blade and disk attachment and overhead conductors are subjected to variable amplitudes over time [102, 29]. In such cases, some questions are not trivial, for instance: how to determine the fatigue life of a component subjected to variable fretting loading conditions from the knowledge of simple stress (S) × life (N) curves of the material? How to account for the strong stress gradient inherent to fretting problems? Is it necessary to consider wear in such an analysis? Questions like these are what motivated the development of this doctoral thesis.

One of the first scientific studies on this failure process, carried out in 1911, showed that on the contact surface of steel grips there was the presence of oxide debris [55]. Although Tomlinson [163] associated the fretting process with very small relative tangential displacements on the contact surface between materials and Warlow-Davies [169] and McDowell [105] demonstrated the combination of effects of fretting and fatigue could reduce material fatigue strength significantly, only in the 1960s that parameters such as contact pressure, relative tangential displacement, contact size, fretting wear, environment conditions and stress concentration on fretting fatigue were analyzed independently [122, 123, 124, 125, 126]. These studies have shown that the frequency of cyclic loading has no significant influence on life and that due to some fretting fatigue tests present non-propagating cracks it can lead to conclude that despite the fretting process collaborate for the crack nucleation, some parameters may retard or hinder the evolution of these cracks. Tests investigating the influence of relative slip showed that for values between 5μm and 50μm a fatigue strength was reduced while above 50μm of slip displacement fatigue cracks were not observed. This behavior was later investigated by Vingsbo and Söderberg [168], Figure 1.1 shows that the effect of wear is proportional to slip displacement. Nishioka and Hirakawa [124] showed that the mean stress applied to the specimens did not

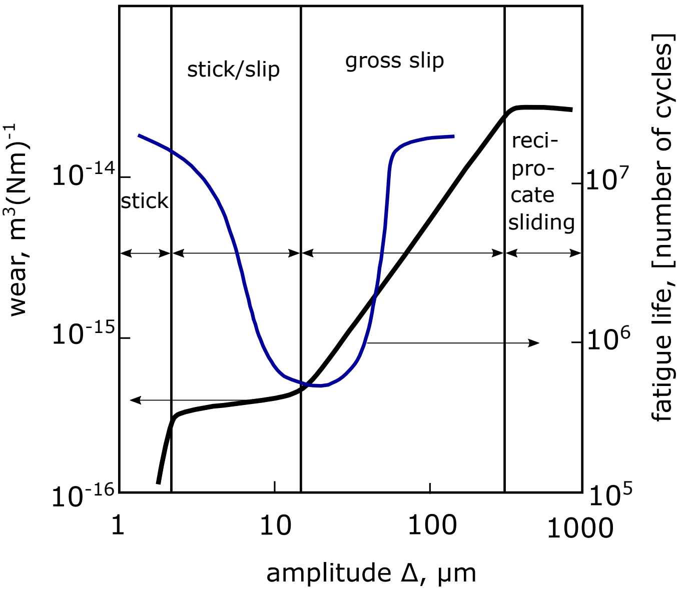

Figure 1.1: Fretting map: wear (black line) and fatigue life as function of slip amplitude [168].

have major effects on the life of components subjected to fretting fatigue, and that cracks tend to initiate in the high stress zones close to the contact edges and propagate entering the region behind the zone contact.

In 1973, Bramhall [24] carried out a study using constant peak pressure and varying the size of the contact, this work showed that for a certain critical size of the contact the life of fatigue is drastically reduced. He attributed this behavior to the stress gradient effect, because, small contacts have steeper stress decays, whereas larger contacts have smoother ones for the same levels of surface stress. This behavior was later confirmed by other authors as [127, 6]. Later, studies by Endo and Goto [56] showed that the crack propagation process in fretting problems has two distinct stages. In their tests, they performed crack growth measurements on mild still using cylindrical pads under gross slip conditions. First, in the crack nucleation process (stage I), it was noted that cracks initiated on shear planes and then quickly started propagating nearly perpendicular to the contact surface (stage II). A literature review of palliatives for fretting fatigue as surface treatments, coatings, shims, and friction reduction was carried out by Gordelier and Chivers [70] and another study focused on stress concentration effects by Wright and O'Connor [174].

Ruiz et al. [140] proposed a parameter based on the definition of an energy damage parameter defined as the product of the local slip amplitude with the maximum shear traction, $K1 = \delta\tau$. This parameter is widely used to predict fretting fatigue performance and predict the location of fretting fatigue crack initiation. Later this parameter was modified including the maximum stress component parallel to the contact surface, $K2 = \delta\tau\sigma_{xx}$. Although the modified Ruiz parameter, $K2$, presents better estimates of the crack initiation site, the physical interpretation of this parameter is not very clear [37].

In view of the expressive advance of the contact mechanics theory over the last century due to works carried out by [77, 31, 113, 87], great advances were made in studies on fretting fatigue due to the possibility of obtaining precise information about the mechanical fields through analytical solutions of contact mechanics. Given these advances, other authors were able to start working with differences theories to predict fretting fatigue performance, such as notch analogy [68, 10, 46], crack analogy [67, 36] and short crack arrest [6, 46, 65]. At this point, it is almost impossible to cover all relevant contributions to the field of fretting fatigue in recent years. Therefore, as this doctoral thesis aims to investigate the effects of loads with variable amplitudes on the fretting fatigue problem, the next section will bring a brief review of works related to this subject.

1.1.1 Review of the state of the art on fretting fatigue under variable amplitude loading

In the early 1980s Kantimathil and Alic [89] reported fretting fatigue tests conducted on the 7075-T7351 experiencing variable loading. Specimens were subjected to constant amplitude loading conditions followed by tensile overloads applied at each 1,000 cycles. Compressive overloads were also assessed. For the constant amplitude loading cycles, different load ratios were considered. From their results, they have observed that the influence of the overloads were negligible for constant amplitude cycles with high maximum bulk stresses. However, for lower maximum values of the bulk stress in the constant amplitude cycles, overloads seemed to have a beneficial effect in terms of fatigue resistance, which may be explained by crack growth retardation due to plastic deformation at the crack tip.

Mutoh et al. [114] published a paper in 1987 where they examined the fretting fatigue resistance of a low strength medium carbon steel for two-step variable amplitude loading blocks. Each block consisted of n_1 cycles at a given bulk stress amplitude $\sigma_{b,1}$ followed by n_2 cycles at $\sigma_{b,2}$. In other words, each block consisted of $(n_1 + n_2)$ fretting cycles. Different combinations of n_1 and n_2 per block were considered in their analysis. They concluded that when the block contained a large enough number of cycles and the number of blocks to failure were smaller than 5 or 6, the variable amplitude loading condition lead to life reductions up to 10 times. It was also shown that Miner's linear rule did not always provide good estimates, as it was the case for plain fatigue conditions. Besides, they have highlighted that fretting fatigue life is highly influenced by the number of cycles at high stress levels, where crack growth rates become significant.

Two years later, Mutoh et al. [115] investigated the fretting fatigue resistance of a high strength steel under random loading conditions. Two load spectrum were examined (A and B). In spectrum A, the maximum value of the bulk stress was 45 % greater than its RMS over time, while in spectrum B it was 85 % greater. Overall speaking, random loading conditions reduced fretting fatigue lives by a factor of 1.5. In addition, Miner's rule led to satisfactory life estimates but being generally nonconservative.

In the late 1990s Troshchenko et al. [164] investigated the fatigue damage accumulation in Al and Ti alloys under variable loading conditions in the presence of stress concentration and fretting conditions. In their analysis, failure is not necessarily assumed to occur when Miner's cumulative damage reaches the unity. Then, they reported that damage computations by assuming Miner's linear rule for the fretting fatigue case under variable amplitude loading were equal or exceeded those from smooth specimens. The work was based on the construction of S-N curves considering constant amplitude conditions for a further comparison with tests carried out under variable amplitude programs.

Cortez et al. [39], in the same period, investigated the fretting fatigue behavior of the Ti-6Al-4V under constant and variable amplitude loading. Besides, they also evaluated the influence of the loading frequency on the experiments. For the variable amplitude loading tests, the loading history consisted of 500 high-frequency small amplitude cycles at 200 Hz followed by a single large amplitude cycle at 1 Hz. The maximum load for small and large amplitude cycles were the same. Different positive load ratios were considered in the small amplitude cycles while a load ratio of about 0.1 was observed in the large amplitude cycles. Two main conclusions were drawn concerning the variable amplitude loading tests. Firstly, it was observed that the variable amplitude loading conditions did not present a significant impact on the fretting fatigue resistance of the Ti-6Al-4V assessed. In addition, from the constant amplitude fretting fatigue loading tests, they have used Miner's rule to estimate life at variable loading conditions. In this case, Miner's rule provided reasonably accurate results although slightly optimistic.

Kinyon and Hoeppner [91] in 2000 also presented interesting results concerning fretting fatigue tests under variable amplitude loading. Tests were carried out on a Ti alloy. Three different amplitudes of bulk stress were considered in their analysis ($\sigma_{b,1} > \sigma_{b,2} > \sigma_{b,3}$), where both two and three-step loading blocks were investigated. For the two-step loading tests, the loading sequence consisted of one cycle subjected to $\sigma_{b,1}$ followed by another cycle subjected to $\sigma_{b,2}$. These two cycles with different amplitudes were repeated up to the specimen's failure (Case 1). Similarly, another two-step loading block was considered but at this time replacing $\sigma_{b,2}$ by $\sigma_{b,3}$ (Case 2). For the three-step loading set (Case 3), the specimen was subject to one cycle at each stress amplitude $\sigma_{b,1}$, $\sigma_{b,2}$ and $\sigma_{b,3}$, where these three blocks were repeated until failure. Throughout fretting fatigue tests performed with constant amplitude loads ($\sigma_{b,1}$,$\sigma_{b,2}$ and $\sigma_{b,3}$), the authors found that the application of Miner's rule provided unsafe life estimates for the Case 1 and conservative predictions for the Cases 2 and 3. At the end, the authors claimed that Miner's rule did not seem appropriate to model fretting fatigue lives.

In the 2000s Kondo et al. [92] investigated the fretting fatigue behavior under variable amplitude loading conditions for a low alloy steel. In their work, the authors first obtained a fretting fatigue limit diagram (like the modified Goodman line) when considering constant amplitude loadings. Different tests were carried out considering the same contact normal load but with different fatigue load ratios. At this stage, for fatigue limit conditions under small mean bulk loads, non-propagating cracks were observed. As the mean bulk load was increased in the tests, cracks were not formed at all. In the next, the authors carried fretting fatigue tests considering repeated two-step loadings. In this setting, one of the loading blocks considered fatigue limit conditions by the application of a fully reversed fatigue stress ($\sigma_{b,1}$), while the other block, with amplitude $\sigma_{b,2}$, was set considering positive mean stresses. It is worth noting that, in this case, $\sigma_{b,2}$ was chosen well below the fatigue limit obtained from the fretting fatigue limit diagram with constant amplitude. Summarizing, it was observed that, even though $\sigma_{b,1}$ and $\sigma_{b,2}$ were below the fatigue limit for constant amplitude loading conditions, the repeated two-step loading of $\sigma_{b,1}$ and $\sigma_{b,2}$ could lead to failure. At the end of the paper, these authors highlight that care should be taken when using fatigue limit data from constant amplitude fretting fatigue tests once under variable amplitude loading, failure may occur even for stresses below fatigue limit conditions.

Massingham and Irvin [103] in 2006 started their work by highlighting the lack of investigations on fretting fatigue under variable amplitude loading. They have developed a finite element model to assess the influence of overloads followed by the maintenance of constant amplitude loads during the simulations. As the main conclusion, it is verified that in spite of the application of two or more overload cycles, the position of the stick-slip zone boundary as well as shear stress distributions depends only on the largest previous cycle. In other words, the order that the overloads are applied is important in determining whether shear stress distributions are modified, besides, it is the largest previous overload that will dictate the shear stress distribution in subsequent smaller amplitude cycles. The authors also suggest that these changes in stress distribution tends to make linear damage rules act conservatively.

More recently, Gandiolle and Fouvry [66] have conducted experiments and a numerical study in order to evaluate the crack propagation rate for fretting fatigue under variable loading conditions. Crack length was obtained during the tests by using a potential drop technique. Further, a numerical decoupled approach was used to obtain the crack stress intensity factor, which allowed relating the crack extension with the number of cycles by considering Paris law. Even though they have not focused on the specific effects of considering variable amplitude loads, the strategy permitted the estimate of important parameters such as crack arrest, the crack extension and the number of cycles to failure.

This comprehensive review of the state of the art on variable amplitude fretting fatigue revealed that most of the research carried out up to now was based on the use of (i) S-N curves generated by fretting fatigue tests performed on one actuator fretting fatigue devices (thus bulk and fretting loads are coupled), (ii) the use of Miner's damage rule and (iii) uniaxial fatigue analysis to estimate life. This is obviously a rather simple research approach as it misses the systematic investigation of a number of well know important characteristics of the fretting problem such as the wear, the stress gradient, the multiaxial state of stress, the varying stress ratio, contact nonlinearities, among others parameters. As there is a lack of control of such parameters in these previous works, it has not been possible to draw more firm conclusions even about the applicability of Miner's linear damage rule to fretting fatigue [114, 115, 164, 39, 91]. Although more detailed studies have been proposed more recently [103, 66], they are clearly just a few, which considered a limited range of materials and loading conditions.

1.2 Objectives

In order to predict the fatigue life of a component subjected to variable amplitude loads, or to random loads, a cumulative damage law must be used. Palmgren-Miner's law, or simply Miner's rule [129, 109], is one of the most well known in the technical literature. This is a linear damage accumulation rule, i.e., it estimates that the order of application of the variable amplitude loading blocks does not change the component fatigue resistance, as long as the total damage produced by such blocks is the same at the end. According to this law, the order of application of the load blocks with variable amplitude does not change the fatigue resistance or the fatigue life of the material as long as the fatigue damage per each block is the same. In this setting, it is important to verify Miner's law applicability evaluating its performance in classical fretting fatigue tests subject to loadings with variable amplitude. Although there are a few works evaluating fretting fatigue response under variable amplitude loading conditions, most of them rely on the construction of fatigue resistance curves for further comparison with variable amplitude loading conditions. In this case, even when Miner's rule is considered, simple uniaxial fatigue approximations are adopted.

With this in mind, the main objective of this thesis is to investigate the effect of sequences of variable amplitude shear loadings on contact tractions/stresses and on the development of life estimation methodologies for these more challenging loading histories. Therefore, a numerical methodology will be developed capable of computing the wear in the crack nucleation phase, estimating the crack initiation angle, and propagating this crack until the failure. For validation of the methodology, experimental data available in the literature and a wide set of fretting fatigue under variable amplitude loading tests will be used.

Other more specific aims of this work are:

- To develop a FE model to estimate crack initiation (life and orientation) which considers the update of the worn surface profile.
- To develop a numerical model to compute crack propagation path and life under mixed cyclic loading mode.
- To perform a set of new fretting fatigue tests under variable amplitude shear loading blocks to investigate the effects of the loading sequence in the life assessment of cylinder on plane contact configurations, where both specimens and pads were made of the aeronautical Al 7075-T651 alloy.

1.3 Thesis scope and methodology

The thesis is organized by first presenting an introduction to address the scope, next a literature review is conducted and a detailed description of the experimental work is provided. Then, the following chapters describe the different analyses and results obtained by applying the different predictive methodologies proposed in this work. More specifically, this thesis is structured as follows:

- **Chapter 1:** A general scope is given followed by a review of the main research progress in the field of fretting fatigue under variable amplitude loading.

- **Chapter 2:** This chapter is a literature review and addresses the following aspects: fatigue, multiaxial fatigue, fracture mechanics, basic contact mechanics, critical distance approach, wear, and numerical methods.

- **Chapter 3:** All experimental work carried out in this doctoral thesis is summarized in this chapter. Initially, basic experimental tests are presented for characterization of the material, and then the fretting fatigue tests under variable amplitude loading are presented. A section is also dedicated to present some experimental data available in the literature.

- **Chapter 4:** Three different numerical methods for life assessment of fretting fatigue have been introduced in this chapter, which may or not include the effects of surface wear. The XFEM method was used for crack simulation and a new method to estimate crack propagation path, that takes into account the effect of the load's non-proportionality in fretting conditions, is presented. In this case, fretting tests available in the literature using an Al 2024-T3 cylindrical contact under partial slip conditions are considered. The same set of experimental tests is employed to investigate damage accumulation using a fixed and variable critical distance.

- **Chapter 5:** This chapter investigates two different methods to predict crack initiation direction in fretting problems subjected to partial slip conditions. In addition, this chapter also investigates the influence of considering wear to estimate the crack initiation direction. For validation of the methods, experimental data from fretting tests conducted on an AA7050-T7451 alloy were used.

- **Chapter 6:** A robust numerical model that includes all fatigue process phases is presented in this chapter. That is a model that includes the wear in the crack nucleation phase and estimates its initiation angle. In addition, the crack propagation until material failure is included. This methodology is applied and validated using the experimental data of fretting fatigue under variable amplitude loading.

- **Chapter 7:** The main conclusions drawn from this thesis are highlighted. Suggestions for future work are also addressed in this chapter.

Chapter 2

Background knowledge

"The main idea of this chapter is about background of different approaches that are used in case of fretting fatigue problem"

2.1 Fatigue

The origin of the word fatigue comes from the Latin expression fatigare. Although this term is associated with physical or mental exhaustion, in engineering, fatigue refers to damage and failures generated by cyclic loading (even at stresses well below a given material's ultimate strength) [152].

In 1837 Albert [142] developed an experimental apparatus to study observed failures in crane chains. Despite being one of the first works carried out on fatigue, it was only after Poncelet's work in 1839 that the term began to be used [134]. It is also noteworthy remembering one of the main names in fatigue, August Wöhler, his work was motivated by railway axle failures. In the 1850s he tested irons, steels, and other metals under bending, torsion, and axial loads. His work has inspired great names like Gerber and Goodman on predicting mean stress effects [49]. Schutzs in 1996 summarized several of the important contributions in this area covering the period 1837 to 1996 [143].

It is quite common to associate the phenomenon of fatigue only with metallic materials. However, many materials with applications in engineering have become objects of great interest. In this context, research with non-metallic materials such as ceramics [151, 139], polymers [79, 78] and composites [178] are increasing.

Etimated 80% of the economic costs of fracture and its prevention involve situations where fatigue is at least a contributing factor. About 3% of the gross national product (GNP) of U.S. economy is expended with fatigue of materials. Because of this, fatigue failures are a major concern in engineering design [49]. However, the understanding of this phenomenon and successive advances to understand or minimize it permeate economic issues insofar as disasters are avoided, saving lives.

2.1.1 The physical nature of fatigue damage

On a small size scale, the materials are anisotropic and inhomogeneous. Because the materials are formed by an aggregate of small crystal grains and the orientation of the crystalline planes is different from one grain to another. Furthermore, tiny voids and inclusions (particles of distinct chemical compositions) contribute to this inhomogeneity. As a result, stresses are distributed in a non-uniform manner inside of the material, and regions, where the stresses are severe, are usually the points where fatigue damage starts [49].

In 1903 Ewing and Humphrey carried out fatigue tests with specimens made from high quality Swedish iron [58]. Examining the same region of the specimen

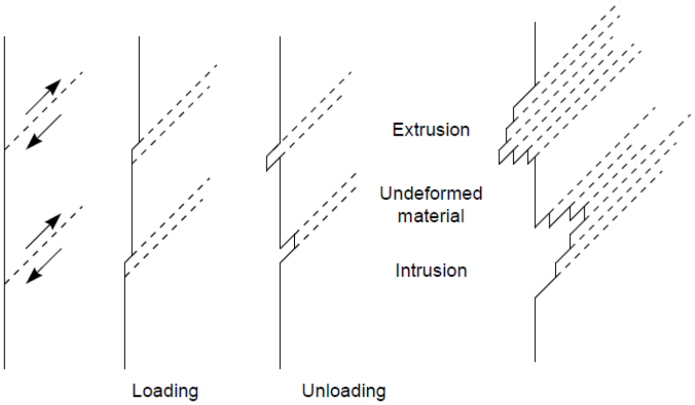

Figure 2.1: Schematic representation of slip band formation [149].

at various stages of the fatigue life, they noticed slip lines on some of the crystals (grains) after a few cycles. These slip lines increased in scale over the cycles joining other crystals and finally developing a crack on the surface of the specimen. Over the years, through testing with electron microscopes, X-ray and other powerful tools, there has been a consensus that fatigue crack nucleation is the result of alternating shear stresses and strains [149].

In general, as shown in Figure 2.1, we can say that the alternating shear stresses/strains move the discordances of the crystalline planes that cause the formation of the persistent slip bands (PSBs). Some slip bands called extrusions to come out of the surface of the material, and intrusions go into the surface. Some slip bands develop into cracks within grains, which then spread into other grains, joining with other similar cracks, and producing a large crack that propagates to failure. Crack nucleation occurs especially at the material surface, when it occurs subsurface, it is usually caused by stress concentration in tiny voids or inclusions [149, 49].

The crack nucleation, as well as the propagation within the material, are extremely important to have a more robust description of the fatigue process. The first cracks appear on the faces of individual grains. Although the crack orientation is slightly different from one grain to another, the overall growth path is maintained along planes of maximum shear stress (Stage I). Upon reaching a large enough size, the crack turns to grow perpendicular to the tensile stress axis (Stage II). Figure 2.2 illustrates this process. This transition is governed by the material microstructure, loading (compression and torsion), and the environment [149].

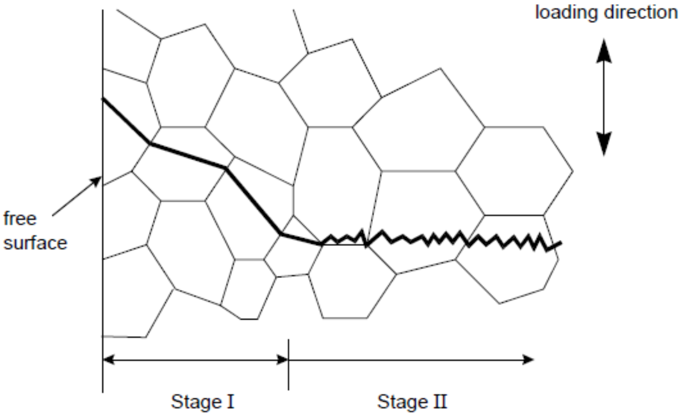

Figure 2.2: Stage I/Stage II growth process [149].

2.1.2 Fatigue aproaches

There are two classic approaches to fatigue. They can be characterized in terms of stress (S-N approach) and strain (ε-N approach). Both methods aim to estimate the life in the number of cycles, N_f, until material failure or crack nucleation. For this, tests are performed in laboratories with smooth specimens (without initial cracks) controlling the stress (S-N) or strain amplitude (ε-N). The S-N approach is indicated for high cycle fatigue or simply for $N_f > 10^3$. In cases where the stress level is close to the yield point, involving significant plastic deformation, the strain approach is recommended [142].

The S-N curves are plotted in terms of stress amplitude versus cycles to failure, Figure 2.3. S-N curves vary with the material and are also affected by mean stress, geometry, surface finish, chemical and thermal environment, frequency of cycling, and residual stress [49]. The equation for representing S-N curves is:

$$\sigma_a = \sigma_f^{'}(2N_f)^b \tag{2.1}$$

where $\sigma_f^{'}$ and b are respectively the fatigue strength coefficient and exponent.

In the strain-based approach, a strain versus life curve is plotted with strain amplitude versus cycles to failure. A schematic diagram of a ε-N curve on log–log coordinates is shown in Figure 2.4. It is important to note that the

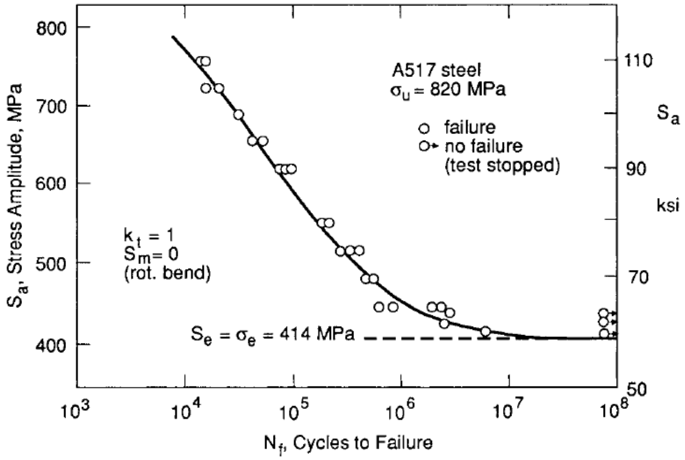

Figure 2.3: S-N curve for unnotched specimens of a steel [49].

strain amplitude can be split into elastic and plastic parts. The elastic strain amplitude is related to the stress amplitude and, the plastic strain amplitude is a measure of the half-width of the stress-strain hysteresis loop. With a separated log-log plot of these curves, it is possible to identify the relationship between the total strain amplitude and the life as:

$$\varepsilon_a = \frac{\sigma_f^{'}}{E}(2N_f)^b + \varepsilon_f^{'}(2N_f)^c \tag{2.2}$$

The quantities $\varepsilon_f^{'}$ and c are respectively the fatigue ductility coefficient and exponent. Note that they are considered to be material properties. When more than one amplitude or mean level occurs, the Palmgren-Miner damage accumulation rule, or just Miner's rule, may be used to life estimates by summing cycle ratios as Eq. 2.3 [129, 108]. Where n_i represents the number of cycles in which a stress amplitude was applied, and N_{fi} is the number of cycles to failure for that same stress amplitude. Note that the sum of damage generated by each load block must equal 1 for the failure to occur.

$$\sum_{i=1} \frac{n_i}{N_{fi}} = 1 \tag{2.3}$$

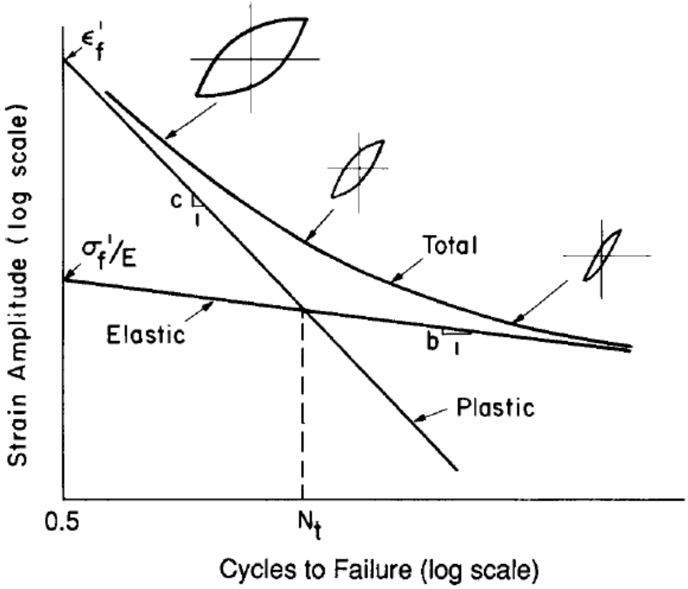

Figure 2.4: Elastic, plastic, and total strain versus life curves [49].

2.2 Multiaxial fatigue life assessment

It is very common that real fatigue conditions can exhibit a multiaxial stress state. Mechanical components in a fretting condition are one of those cases. Several approaches and damage parameters have been used for problems subjected to multiaxial stress conditions. The first experimental works in this area date back to the 1930s and 1940s, they served in the future to give rise to the first multiaxial criteria [71, 121]. These multiaxial models can currently be classified as a critical plane [62, 146, 154], stress invariant approaches [41, 145], fretting specific parameters [74, 44], and continuum damage mechanics approach [97, 33]. In this work, two different multiaxial fatigue models based on critical plane approaches are considered and reviewed in this section. However, a brief introduction to the use of Cauchy's Theorem to obtain the stress components relative to a generic plane will be presented first.

2.2.1 Stress components relative to a generic material plane

In a multiaxial fatigue context it is very important to understand how external loads combine to produce stresses and strains in the critical location of a structure or component [149]. Considering a body loaded by an external system of forces, as in Figure 2.5, the stress state at point O is triaxial [153]. In other words, at any instant t of the applied cyclic load history (having period T) the stress tensor at O can be expressed as:

$$\mathbf{T}(t) = \begin{bmatrix} \sigma_x(t) & \tau_{xy}(t) & \tau_{xz}(t) \\ \tau_{xy}(t) & \sigma_y(t) & \tau_{yz}(t) \\ \tau_{xz}(t) & \tau_{yz}(t) & \sigma_z(t) \end{bmatrix} \tag{2.4}$$

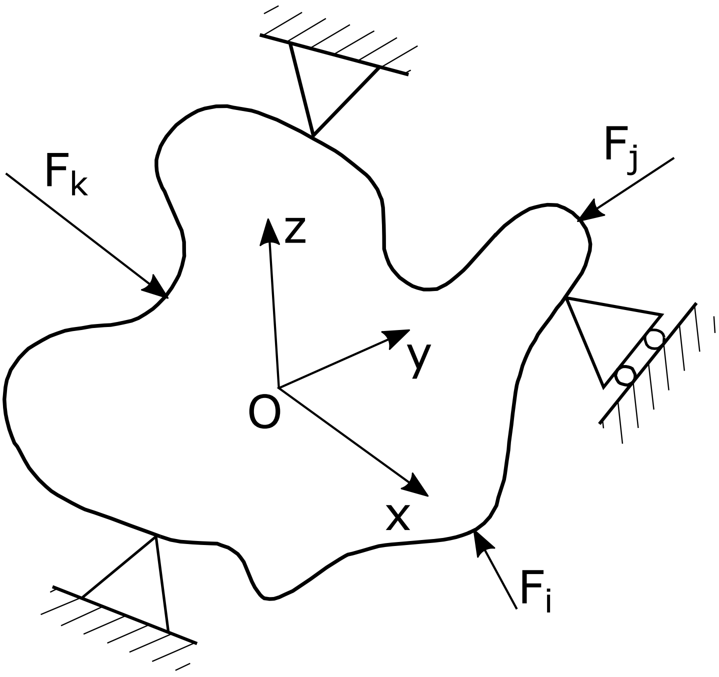

Figure 2.5: Body subjected to an external system of forces. [153].

The Cauchy's theorem can be used to investigate the stress state at any material plane. As depicted in Figure 2.6, the Cauchy stress vector can be decomposed into:

$$\mathbf{t} = \mathbf{T}\mathbf{n} = \mathbf{t}_n + \boldsymbol{\tau} \tag{2.5}$$

Since the normal stress vector is given by $\mathbf{t}_n = \sigma_n \mathbf{n}$, the normal stress, σ_n, can be calculated as follows:

$$\sigma_n = \mathbf{t} \cdot \mathbf{n} = (\mathbf{T}\mathbf{n}) \cdot \mathbf{n} \tag{2.6}$$

Isolating the shear stress vector from Eq. 2.5 and substituting the values found in the previous equations, this vector can be determined as:

$$\boldsymbol{\tau} = \mathbf{T}\mathbf{n} - [(\mathbf{T}\mathbf{n}) \cdot \mathbf{n}]\, \mathbf{n} \tag{2.7}$$

Considering a generic plane, as in Figure 2.7. The $\mathbf{n}$ is its normal unit vector and x', y', and z' are the new coordinate system. Where x' is normal to the inclined plane, y' is parallel to the intersection between the inclined and the $x - y$ plane, and z' is perpendicular to the $x' - y'$ plane. Thus, in relation to the new coordinate system, the stress vector can be written as:

$$\mathbf{t} = \sigma_{x'} \mathbf{n} + \tau_{x'y'} \mathbf{n}_{y'} + \tau_{x'z'} \mathbf{n}_{z'} \tag{2.8}$$

With the bases of the new system given in spherical coordinates, the normal and shear stress components can be calculated respectively as follows:

$$\sigma_{x'} = (\mathbf{T}\mathbf{n}) \cdot \mathbf{n} = (\mathbf{T}\mathbf{n}) \cdot \begin{bmatrix} cos\theta sin\phi \\ sin\theta sin\phi \\ cos\theta \end{bmatrix} \tag{2.9}$$

$$\tau_{x'y'} = (\mathbf{T}\mathbf{n}) \cdot \mathbf{n}_{y'} = (\mathbf{T}\mathbf{n}) \cdot \begin{bmatrix} -sin\theta \\ cos\theta \\ 0 \end{bmatrix} \tag{2.10}$$

$$\tau_{x'z'} = (\mathbf{T}\mathbf{n}) \cdot \mathbf{n}_{z'} = (\mathbf{T}\mathbf{n}) \cdot \begin{bmatrix} -cos\theta cos\phi \\ -sin\theta cos\phi \\ sin\phi \end{bmatrix} \tag{2.11}$$

Furthermore, the strains can be computed for any plane too. Because the strains ε_x, ε_y, and ε_z are analogous to the stresses σ_x, σ_y, and σ_z. However, it is worth remembering that only one-half of the shear strains γ_{xy}, γ_{xz}, and γ_{yz} are analogous to the shear stresses τ_{xy}, τ_{xz}, and τ_{yz} [149].

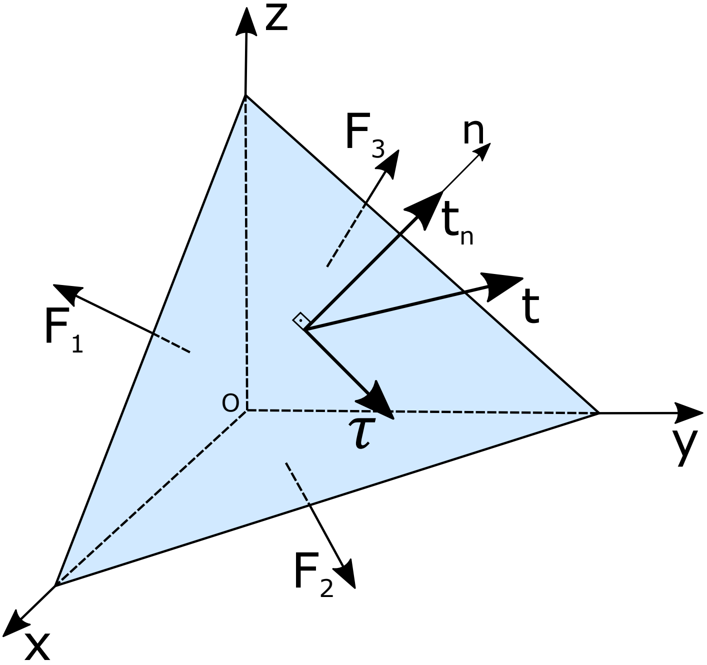

Figure 2.6: Equilibrium condition applied to the Cauchy tetrahedron. F_1; F_2; F_3 are generic loads applied to the outer faces [3].

2.2.2 Smith, Watson and Topper parameter (SWT)

One of the most popular criterion used to determine crack nucleation point and life, SWT parameter is a multiaxial strain energy-based critical plane approach [146]. In addition to its simplicity, which makes this parameter one of the most popular, is the possibility to deal with non-proportional loading conditions and can be applied to high and low cycle fatigue [147]. However, it is important to note that this parameter is better suited for materials and loading conditions where cracks propagate perpendicular to the direction of maximum principal stress and strain (Mode I cracks), as illustrated in Figure 2.8(a) [22]. The SWT parameter can be defined as:

$$SWT = \sigma_{n,max} \frac{\Delta\varepsilon_1}{2} \tag{2.12}$$

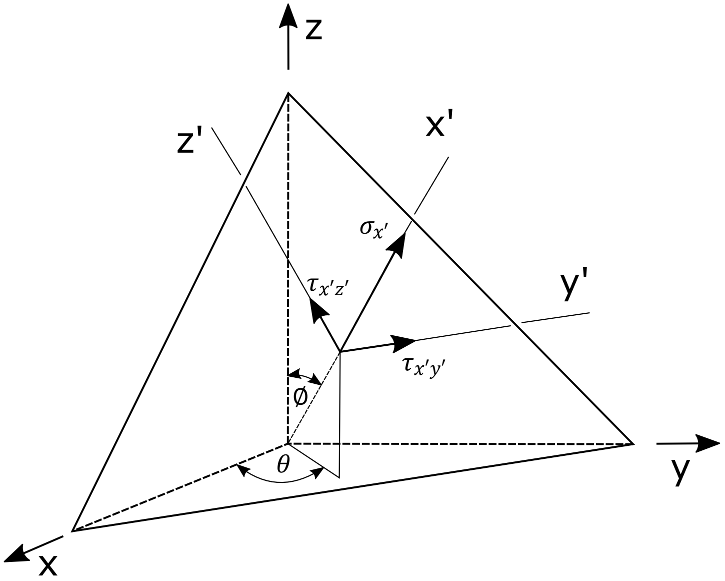

Figure 2.7: Stresses acting on a plane in a three dimensional coordinate system [149].

where $\Delta\varepsilon_1$ is the maximum range of principal strain and $\sigma_{n,max}$ is the maximum normal stress in the plane where the maximum range of principal strain is produced. It also allows estimating the component life by reference to a fully reversed uniaxial test where stress (Basquin) and strain (Coffin Manson) life relations can be combined yielding:

$$\sigma_{n,max}\frac{\Delta\varepsilon_1}{2} = \frac{\sigma_f^{'}}{E}\left(2N_f\right)^{2b} + \sigma_f^{'}\varepsilon_f^{'}\left(2N_f\right)^{b+c} \tag{2.13}$$

where $\sigma_f^{'}$ and $\varepsilon_f^{'}$ are the fatigue strength and ductility coefficients, respectively, while b and c are the fatigue strength and ductility exponents, respectively.

2.2.3 Fatemi-Socie parameter (FS)

Fatemi and Socie [61] proposed this parameter based on Brown and Miller's parameter. Different from Brown and Miller, the parameter proposed by Fatemi and Socie incorporated the effect of non-proportional loading and mean stress.

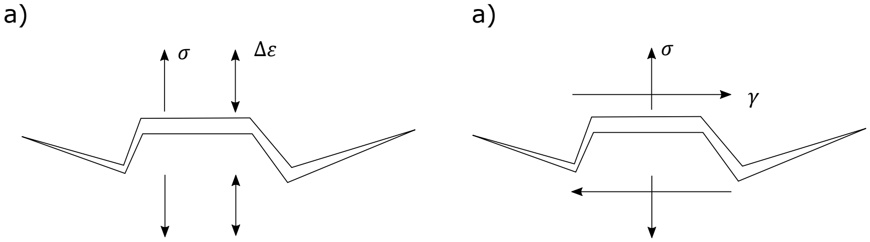

Figure 2.8: Physical basis of the SWT (a) and FS (b) model [149].

It is known that the FS parameter is suitable for situations where material failure occurs in shear mode as illustrated in Figure 2.8(b), and additionally, this parameter can predict the fatigue failure accurate for both in-phase and out of phase loading cases. Fatemi-Socie parameter can be expressed as:

$$FS = \frac{\Delta\gamma_{max}}{2}\left(1 + k_2\frac{\sigma_{n,max}}{S_y}\right) \tag{2.14}$$

where, $\Delta\gamma_{max}$ is the maximum shear strain range, S_y is the yield strength and k_2 is a material constant and characterizes the effect of normal strain on initial crack growth.

Most of the researchers [7, 100, 98] employed an alternative form proposed by Socie et al. [148], this form to compute cycles to initiation under fretting fatigue conditions can be written as:

$$FS = \frac{\tau_f^{'}}{G}(2N_f)^{b^{'}} + \gamma_f^{'}(2N_f)^{c^{'}} \tag{2.15}$$

where, $b^{'}$ and $c^{'}$ are respectively the fatigue strength exponent and the fatigue ductility exponent in torsion, $\gamma_f^{'}$ is shear fatigue ductility coefficient, G is the shear modulus and $\tau_f^{'}$ is the fatigue strength coefficient in shear.

2.3 Fracture mechanics

Fracture mechanics is a field of solid mechanics that deals with the mechanical behavior of cracked bodies. This discipline was no longer just a scientific curiosity during World War II. A large number of ships supplied by the United States to the United Kingdom during the war were built with an all-welded hull, as opposed to the riveted construction of traditional ship designs. A large number of these ships, known as Liberty Ships, had catastrophic failures. Which in a way boosted the study on the behavior of cracked bodies [4].

After World War II, the fracture mechanics research group at the Naval Research Laboratory was led by Irwin [86]. The first studies in an attempt to quantify the effects of cracking were carried out by Inglis in the early 1900s [85]. He published a stress analysis for an elliptical hole in an infinite linear elastic plate loaded at its outer boundaries. Subsequently, based on his tests on cracked glass spheres, Griffith transformed the Inglis analysis by calculating the effect of the crack on the strain energy stored in an infinite cracked plate and proposed that this energy should be taken as a measure of the tendency of the crack to propagate [72]. Irwin, using the concepts developed by Inglis and Griffith, to extend the Griffith approach to metals by including the energy dissipated by local plastic flow.

2.3.1 Modes of fracture

There are three different ways of crack propagation, Irwin [86] proposed a classification corresponding to the situations represented in Figure 2.9, the crack can propagate in one of these loading modes or with a combination of them. Traction loading gives rise to Mode I, the crack opening propagation mode, the most common. Most crack propagation problems mainly involve mode I. Mode II is the sliding mode, a result of shear in the crack propagation plane. Mode III is the tearing mode, the result of shearing outside the propagation plane.

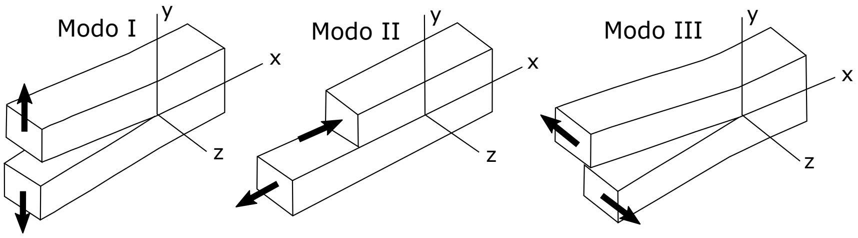

Figure 2.9: Fracture modes, from right to left mode I, mode II and mode III, respectively.

For each mode, crack propagation can only occur in the x-axis direction (original crack direction). In a more general case, a mixed-mode situation can generally be observed, where modes overlap. In the mixed linear elastic problem, the principle of stress superposition indicates that each contribution to a given stress component is additive and can be written as:

$$\sigma_{ij} = \sigma_{ij}^{I} + \sigma_{ij}^{II} + \sigma_{ij}^{III} \rightarrow i,j = x,y \tag{2.16}$$

According to linear elastic theory, cracks introduce discontinuities in the elastomer; therefore, when approaching the crack tip, the tension tends to infinity. Irwin [86] discussed the singular behavior of the stress component at a distance r from the crack tip. The relation he obtained can be written in a simplified form as:

$$\sigma = \frac{K}{\sqrt{2\pi r}} \tag{2.17}$$

The stress intensity factor, K, plays a fundamental role in fracture mechanics, as it characterizes the stress field at the crack tip. Equation 2.17 is valid only near the crack tip, where the singularity $1/\sqrt{r}$ dominates the stress field. Stresses distant from the crack tip are governed by remote boundary conditions.

2.3.2 Crack tip stress and displacement fields

Considering a static 2D crack in the plate under plane stress. Suppose there is no tension on the crack surface, and the crack is positioned along the negative x-axis, as shown in Figure 2.10. Then, the stress distribution in the area near the crack tip can be derived as:

$$\sigma_{ij}(r,\theta) = \frac{K_I}{\sqrt{2\pi r}} f_{ij}^{I}(\theta) + \frac{K_{II}}{\sqrt{2\pi r}} f_{ij}^{II}(\theta) + \sigma_{ij}^{0} \tag{2.18}$$

for $r \rightarrow 0$, $i,j = x,y$, and σ_{ij}^{0} indicates the finite stresses at the crack tip. The constants of the stress field K_I and K_{II} represent the stress intensity factors (SIFs) for the corresponding modes I and II, respectively, and are defined as:

$$K_I = \lim_{r \rightarrow 0} \sqrt{2\pi r}\sigma_y(r,0) \tag{2.19}$$

$$K_{II} = \lim_{r \rightarrow 0} \sqrt{2\pi r}\tau_{xy}(r,0) \tag{2.20}$$

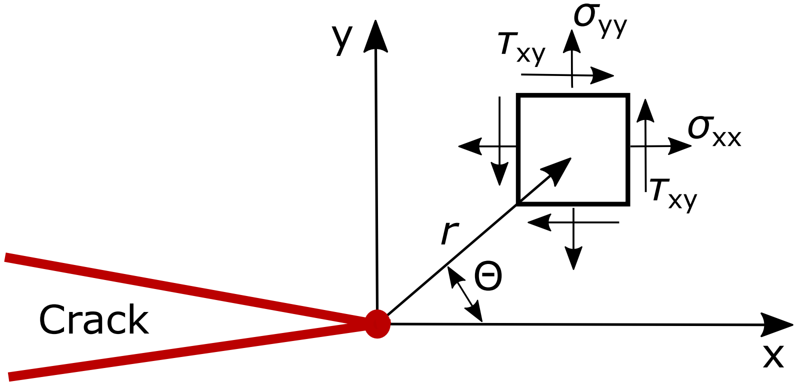

Figure 2.10: Crack tip stress field.

When considering the assumption of the two-dimensional mechanical problem of Linear Elastic Fracture Mechanics (LEFM) in mixed mode, the size of the plastic zone around the crack tip is very small compared to the size of the structure. As shown in Figure 2.10, for the element near the crack tip, according to Anderson [4], the two-dimensional formulation of calculating stresses and displacement in a mixed mode is:

$$\begin{aligned} \begin{Bmatrix}\sigma_x\\ \sigma_y\\ \tau_{xy}\end{Bmatrix} &= \frac{K_I}{\sqrt{2\pi r}} cos\left(\frac{\theta}{2}\right)\begin{Bmatrix}1 - sin\frac{\theta}{2}sin\frac{3\theta}{2}\\ 1 + sin\frac{\theta}{2}sin\frac{3\theta}{2}\\ sin\frac{\theta}{2}cos\frac{\theta}{2}cos\frac{3\theta}{2}\end{Bmatrix} \\ &+ \frac{K_{II}}{\sqrt{2\pi r}}\begin{Bmatrix} sin\frac{\theta}{2}\left[2+cos\frac{\theta}{2}cos\frac{3\theta}{2}\right]\\ sin\frac{\theta}{2}cos\frac{\theta}{2}cos\frac{3\theta}{2}\\ sin\frac{\theta}{2}\left[1 - sin\frac{\theta}{2}sin\frac{3\theta}{2}\right]\end{Bmatrix} \end{aligned} \tag{2.21}$$

and

$$\begin{aligned} \begin{Bmatrix}u_x\\ u_y\end{Bmatrix} &= \frac{K_I}{2G}\sqrt{\frac{r}{2\pi}}\begin{Bmatrix} cos\frac{\theta}{2}\left[k-1+2sin^2\frac{\theta}{2}\right]\\ sin\frac{\theta}{2}\left[k+1-2cos^2\frac{\theta}{2}\right]\end{Bmatrix} \\ &+ \frac{K_{II}}{2G}\sqrt{\frac{r}{2\pi}}\begin{Bmatrix} sin\frac{\theta}{2}\left[k+1+2cos^2\frac{\theta}{2}\right]\\ cos\frac{\theta}{2}\left[k-1-2sin^2\frac{\theta}{2}\right]\end{Bmatrix} \end{aligned} \tag{2.22}$$

In which G is the shear modulus, small differences in the plane stress and plane strain formulas are treated with k, where:

$$k = \begin{cases} 3 - 4\nu \rightarrow PlaneStrain \\ \frac{3-\nu}{1+\nu} \rightarrow PlaneStress \end{cases} \tag{2.23}$$

2.3.3 J-integral

Rice and Rosengren [136, 137] developed the J-integral method, used to evaluate the rate of energy release in crack growth considering a non-linear elastic material, as shown in Figure 2.11. The J-integral is a path-independent line integral and measures the singular stresses and strains near the crack tip. Because it is a path-independent integral, it allows for evaluating linear and non-linear elastic energy release rates and elasto-plastic work far from the crack tip [4]. Consider an arbitrary counterclockwise path (Γ) around the tip of a crack, as in Figure 2.12. J-integral can be written for a crack in the x-y plane as:

$$J = \oint_{\Gamma} \left(wdy - T_i \frac{du_i}{dx} ds \right) \tag{2.24}$$

where w is the strain energy density, which can be written as:

$$w = \int_{0}^{\varepsilon_{ij}} \sigma_{ij} d\varepsilon_{ij} \tag{2.25}$$

T_i and u_i are respectively the traction and displacement vector components in the coordinate system ahead of the crack. σ_{ij} and ε_{ij} are the stress and strain tensors respectively, n_j are the components of the unit vector normal to Γ, and ds length increment along the contour Γ. The traction vector at a given point on the contour T_i is given by:

$$T_i = \sigma_{ij} n_j \tag{2.26}$$

J-integral can also be used as a basis for fracture resistance tests in accordance with ASTM E1820. The advantage of using this method is that there is no need to make large specimens, as the limitations of the Linear Elastic Fracture Mechanical can be exceeded. The fracture toughness given by J_{Ic} can be used to estimate K_{Ic} [49]. For a linear elastic material, we can obtain a relationship between the J-integral and the energy release rate G_e, where $J = G_e$. In this way, the J-integral can be written as:

$$J = \frac{K_I^2}{E} \rightarrow (Stress\ plane\ state) \tag{2.27}$$

$$J = \frac{(1-\nu^2)K_I^2}{E} \rightarrow (Strain\ plane\ state) \tag{2.28}$$

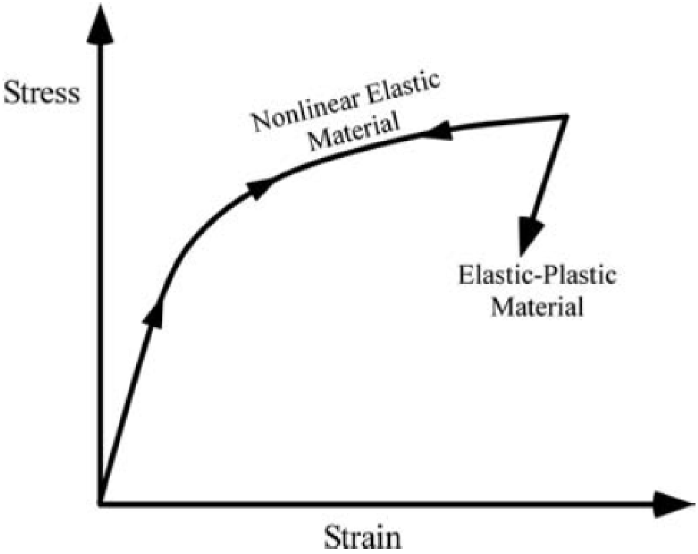

Figure 2.11: Schematic comparison of the stress-strain behavior of elastic-plastic and nonlinear elastic materials [4].

2.3.4 Fatigue crack propagation

In the early 1960s, Paris showed that stress was not the parameter that controls fatigue crack propagation, but the variation in the stress intensity factor, ΔK [130]. In his experiment, Paris used two identical plates, made of the same material and with a central crack of the same length. Due to the relationship between the crack length and the stress intensity factor K, it is possible to associate crack growth with a ΔK.

When plotting the curve da/dN vs ΔK in logarithmic form, a curve with three very distinct phases is obtained, as shown in Figure 2.13. The information

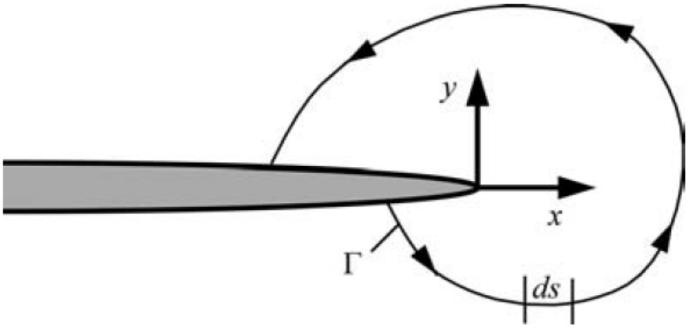

Figure 2.12: Arbitrary contour around the tip of a crack [4].

obtained through this type of graph can be used to predict the residual life in cracked structures.

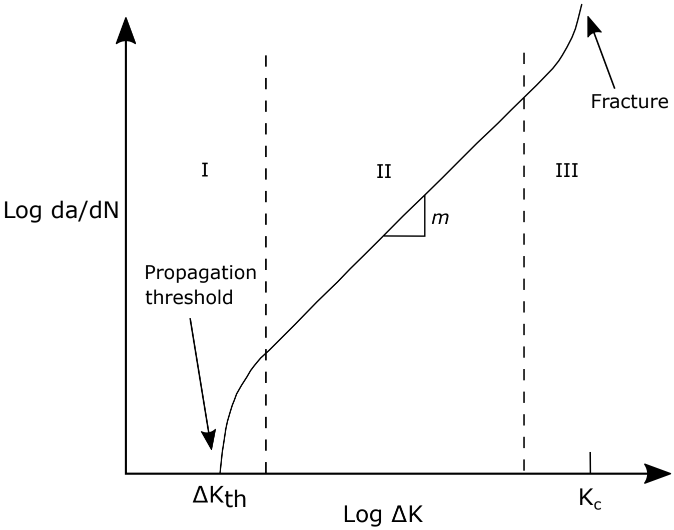

Figure 2.13: Scheme of the da/dN vs ΔK curve.

In phase I, there is a propagation threshold known as the fatigue crack propagation threshold (ΔK_{th}-threshold). For values below the threshold the crack does not propagate, that is, the loads do not cause damage to the material. Phase I ranges from ΔK_{th} to propagation rates of 10^{-7} to 10^{-10} mm/cycle, and crack growth is discontinuous, being generated by micro-mechanisms sensitive to the medium load, to the microstructure of the material, the environment and the crack opening load [42].

Phase II comprises the largest region and can be between the rates of $10^{-10} \sim 10^{-9}$ to $10^{-6} \sim 10^{-4}$ mm/cycle. Crack growth is approximately continuous along its front, and this can be indicated by the streaks on the crack faces seen in scanning electron microscopes. At this stage, propagation is not very sensitive to microstructure, medium load, the environment, and the thickness of the part [42].

The main characteristic of phase III is the unstable crack propagation or the fracture of the part, which occurs when $K_{max} = \Delta K/(1 - R)$ reaches the toughness of the material. The fracture mechanisms are superimposed on those of propagation, and can occur in a ductile (coalescence of voids) or fragile (cleavage) form. This phase is sensitive to the average load and to the factors that influence the toughness of the material, such as the microstructure, the environment, and the thickness of the part [42].

Several well-known empirical models are used to describe the crack propagation rate using parameters obtained from experimental data. These models partly describe the shape of the da/dN vs ΔK curve, and some consider the effects of ΔK_{th}, K_c, and the ratio between the maximum and minimum stress intensity factors. Paris and Erdogan [130] developed the most classic model and became known as the Paris model:

$$\frac{da}{dN} = C(\Delta K)^m \tag{2.29}$$

This model describes the behavior only in phase II and does not consider the effects of the loading rate. Parameter C represents the linear coefficient of the straight section and m the slope. These two parameters are obtained experimentally for each type of material, this is done by applying a linear regression on a log-log scale. In general, the value of m can vary between 2 and 4 for metallic materials [49].

For a mixed-mode loading, ΔK can be replaced by an equivalent SIF given by

$$K_{eq} = \sqrt{K_{I,max}^2 + K_{II,max}^2} \tag{2.30}$$

Therefore, the number of cycles to crack propagation until failure can be calculated using

$$dN = N_f - N_i = N_{if} = \int_{a_i}^{a_f} \frac{da}{C(\Delta K_{eq})^m} \tag{2.31}$$

2.3.5 Crack propagation direction

The stresses and strains at the crack tip can be used to determine the crack propagation angle. Therefore, it is very important to use a numerical method that can estimate the stress field accurately. There are several methods available in the literature widely used to predict the crack trajectory. Some of the most widely used mixed mode criteria are the Maximum Tangential Stress criterion (MTS) [57], the Maximum Energy Release Rate criterion (MERR) [75], and the zero K_{II} criterion ($K_{II} = 0$) [40]. These methods are already implemented in the commercial FE software ABAQUS 6.14. Therefore, the three methods were tested in this thesis.

Despite the popularity and easy implementation of the methods mentioned above, their performance in applications such as fretting fatigue was unsatisfactory [84]. The fretting problem not only presents a non-linear behavior, i.e., it is load history-dependent, but also has a non-proportional load. This explains why traditional methods are unable to predict the crack path very well in fretting applications.

Maximum Tangential Stress (MTS)

The MTS method assumes that the crack propagation angle will be perpendicular to the maximum tangential stress at the crack tip [57]. The near crack tip stress field for a homogeneous, isotropic linear elastic material is given by:

$$\sigma_{\theta\theta} = \frac{1}{\sqrt{2\pi r}} cos\frac{\theta}{2} \left[K_I cos^2\frac{\theta}{2} - \frac{3}{2} K_{II} sin\theta \right] \tag{2.32}$$

$$\tau_{r\theta} = \frac{1}{\sqrt{2\pi r}} cos\frac{\theta}{2} \left[K_{II} sin\theta - K_{II}(3cos\theta - 1) \right] \tag{2.33}$$

where r and θ are polar coordinates centred at the crack tip in a plane orthogonal to the crack face. The direction of crack propagation then can be obtained using either the condition $\partial\sigma_{\theta\theta}/\partial\theta$ or $\tau_{r\theta} = 0$. This can be expressed as:

$$K_I sin\theta_p + K_{II}(3cos\theta p - 1) = 0 \tag{2.34}$$

$$\theta_p = arccos\left[\frac{3K_{II}^2 + \sqrt{K_I^4 + 8K_I^2K_{II}^2}}{K_I^2 + 9K_{II}^2}\right] \tag{2.35}$$

where the crack propagation angle θ_p is measured with respect to the crack plane, i.e., $\theta_p = 0$ represents the crack propagation in "straight ahead" direction and $\theta_p \leqslant 0$ if $K_{II} \geqslant 0$, while $\theta_p \geqslant 0$ if $K_{II} \leqslant 0$.

Maximum Energy Release Rate (MERR)

Hayashi and Nemat-Nasser [75] proposed a linear combination between the SIFs K_I and K_{II} for a global crack with the SIFs of a crack with infinitesimal length positioned at crack global tip. By considering a crack segment of length l kinking out the plane of the crack at an angle θ_p the existing SIFs prior to kinking for the original crack are:

$$K_I^k = \left(\frac{4}{3 + cos^2\theta}\right)\left(\frac{1 - \theta/\pi}{1 - \theta/\pi}\right)^{\frac{\theta}{2\pi}}\left(K_I cos\theta + \frac{3}{2}K_{II} sin\theta\right) \tag{2.36}$$

$$K_{II}^k = \left(\frac{4}{3 + cos^2\theta}\right)\left(\frac{1 - \theta/\pi}{1 - \theta/\pi}\right)^{\frac{\theta}{2\pi}}\left(K_{II} cos\theta - \frac{1}{2}K_{II} sin\theta\right) \tag{2.37}$$

For the crack segment the relation between energy release rate (G^k) and SIFs at small crack tip can be written as:

$$G^k = \frac{1}{E}\left[\left(K_I^k\right)^2 + \left(K_{II}^k\right)^2\right] \tag{2.38}$$

The $MERR$ criterion assumes that the original crack initially propagates in the direction that maximizes G^k. In this way, the MERR method establishes for a general case of mixed-mode loading that the crack initiation occurs from a global energy balance or a point of view of the local stress intensity.

Criterion of local symmetry (Zero K_{II})

This criterion was proposed by Cotterell and Rice [40] and simply postulates that a crack initially propagates in the direction that makes $K_{II} = 0$. The implementation of this criterion within the context of an FE model requires the extension of an infinitesimally small crack from the crack tip, whose direction is varied to attain a minimum for K_{II}. There are a series of direction-dependent coefficients C_{ij} to estimate at the crack tip, the stress intensity factors for different direction was proposed by Hayashi and Nemat-Nasser [75] and can be expressed as:

$$K_I^k = C_{11} K_I + C_{12} K_{II} \tag{2.39}$$

$$K_{II}^k = C_{21} K_I + C_{22} K_{II} \tag{2.40}$$

It was mentioned that the criterion $K_{II} = 0$ assumes that the crack will propagate in the direction where $K_{II}^k = 0$. However, it was observed that the variation on K_{II}, with infinitesimally small crack direction, is approximately linear over a wide range of angles. This linearity has been utilized in an improved algorithm in ABAQUS for finding the optimum direction angle. Therefore, some equation such as Eq. (2.37) can be used to find the next crack propagation angle, which leads to minimum value of K_{II}. In some loading conditions, which are not possible to reach $K_{II} = 0$, therefore ABAQUS searches for the minimum value of K_{II}.

2.4 Computational Fracture Mechanics

Through the LEFM (Linear-elastic fracture mechanical) it is possible to quantify the stress field at the crack tip. For known geometries, this can be done analytically. However, there are cases of complex geometries and loads that require the use of numerical methods. There are several numerical methods such as finite difference [95], finite element [177], and boundary integral equation methods [138]. The latter two numerical methods have been applied almost exclusively. In this thesis, the finite element method (FE method) was used.

At the beginning of the FE method development, it was noticed that the mathematical singularity present at the crack tip was not represented faithfully

[34]. To try to overcome this problem of the mathematical singularity at the crack tip, $1/\sqrt{r}$, special finite elements, known as “quarter-points”, were developed. These elements were proposed by Henshell and Shaw (1975) and Barsoum (1976), and their development brought a significant advance in the use of FE method in problems of linear elastic fracture mechanics [76, 18].

These elements are quadrilateral isoparametric elements with mid-side nodes moved to the quarter points. At the crack tip, quadrilateral elements (in two-dimensional problems) are usually collapsed down to triangles, three nodes occupy the same point in space, as depicted in Figure 2.14. For an elastic linear analysis the collapsed elements are tied, however, for elastic-plastic analyzes, the crack-tip nodes are untied and the location of the mid-side nodes is unchanged [4].

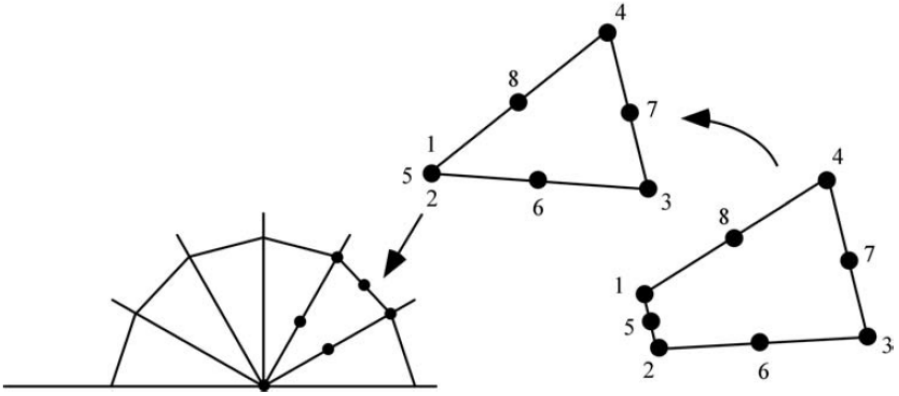

Figure 2.14: Degeneration of a quadrilateral element into a triangle at the crack tip [4].

2.4.1 The energy domain integral

The energy domain integral is a numerical solution of J-integral presented in section 2.3.3. Shih et al. formulated the methodology [144, 112]. This approach is extremely versatile, as it can be applied to quasi-static and dynamic problems with response from elastic, plastic, or viscoplastic materials, as well as thermal loading [4].

As shown in Figure 2.15, a closed contour containing an inner contour Γ_0 and an outer contour Γ_1 is used, where the inner is vanishingly small and the exterior is finite. For quasistatic conditions, the J-integral can be written in terms of the following integral around the closed contour $\Gamma^* = \Gamma_1 + \Gamma_+ + \Gamma_- - \Gamma_0$:

$$J = \int_{\Gamma^*} \left[\sigma_{ij} \frac{\partial u_j}{\partial x_1} - w\delta_{1i} \right] q m_i d\Gamma - \int_{\Gamma_+ + \Gamma_-} \sigma_{2j} \frac{\partial u_j}{\partial x_1} q d\Gamma \tag{2.41}$$

where w is the strain energy density, q is a weight function in the area A^* that allows the domain integral to be handled in the finite element formulation. Usually, a linear function is chosen for q, which assumes a unit value at the crack tip and a null value along the contour, $\Gamma_0 \rightarrow q = 1$, and $\Gamma_1 \rightarrow q = 0$. δ_{1i} is the Kronecker delta, σ_{ij} is the stress tensor, m_i is the outward normal on Γ^*, and Γ_+ and Γ_- are the upper and lower crack faces, respectively. In the absence of crack-face tractions, the second integral in Eq. 2.41 vanishes.

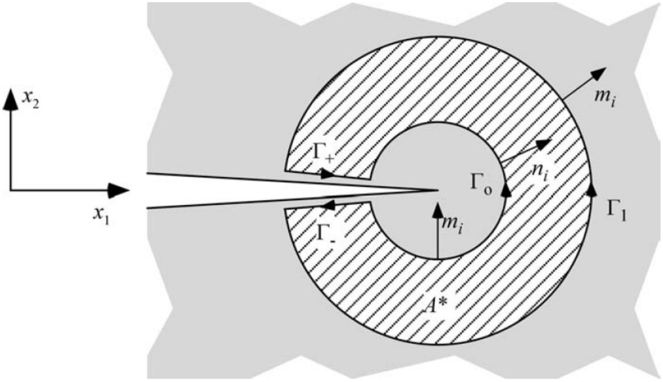

Figure 2.15: Inner and outer contours, which form a closed contour around the crack tip when connected by Γ_+ and Γ_- [4].

Applying the divergence theorem for a linear or nonlinear elastic material under quasistatic conditions, in the absence of body forces, thermal strains, and crack-face tractions, Eq. 2.41 reduces to:

$$J = \int_{A^*} \left[\sigma_{ij} \frac{\partial u_j}{\partial x_1} - w\delta_{1i} \right] \frac{\partial q}{\partial x_1} dA \tag{2.42}$$

Eq. 2.42 is equivalent to Rice's path-independent J-integral (section 2.3.3). When the sum of the additional terms as body forces, thermal strains, and crack-face tractions is nonzero, J is path dependent.

2.4.2 XFEM principles

It is possible to model a stationary crack using the conventional FEM (Finite Element Method); however, there are a number of restrictions regarding the mesh generation. The geometry of a cracked body needs to be matched with the mesh making it necessary to use a very refined mesh. Therefore, the simulation becomes cumbersome. Thus, in this study, the approach namely XFEM (eXtended Finite Element Method) was used to model two dimensional crack propagation problems. Belytschko and Black [19] first introduced the XFEM. It is an extension of the conventional FE method based on the concept of partition of unity by Melenk and Babuska [106], which allows local enrichment functions to be easily incorporated into a FE approximation.

For the purpose of fracture mechanics analysis, as the XFEM technique is the extended version of FEM approach, the FE method basically adds some enrichment functions to the nodes of the elements where there is one crack. These nodes receive other degrees of freedom through a change in the displacement formulation of the finite element method. The enrichment functions typically consist of the near-tip asymptotic functions that capture the singularity around the crack tip and a discontinuous function that represents the jump in displacement across the crack line (in case of 2-D) [110].

The total formulation of XFEM can be derived defining all the nodes in the mesh by the set S_A, the nodes surrounding the crack tip by the set S_c and the nodes whose supports are cut by the crack (excluding the nodes in S_c) defined by S_H. The XFEM formulation can be written as:

$$u^h(x) = \sum_{I \in S_A} N_I(x) u_I + \sum_{J \in S_H} N_J(x) H(x) q_j^0 + \sum_{K \in S_c} \sum_{\alpha=1}^{4} N_K(x) F_\alpha(x) q_k^\alpha \quad (2.43)$$

where, $N_I(x)$ is the usual nodal shape functions for conventional FE formulation. u_I, is the usual nodal displacement vector associated with the continuous part of the FE solution. The second term is the product of the nodal enriched degree of freedom vector, q_j^0, and the associated discontinuous jump function $H(x)$ across the crack line. The third term is the product of the nodal enriched degree of freedom vector, q_k^α, and the related elastic asymptotic cracktip functions, $F_\alpha(x)$. The usual nodal displacement vector, u_I, is implemented to all the nodes in the FE model. The second term, $N_J(x)H(x)q_j^0$, is valid for nodes whose shape function support is cut by the crack. The third term i.e. $N_K(x)F_\alpha(x)q_K^\alpha$, is used only for nodes whose support is cut by the crack tip. Figure 2.16 shows the discontinuous jump function across the crack surfaces, which is defined by:

$$H(x) = \begin{cases} 1 & for, (x - x^*)n \geqslant 0 \\ -1 & else, \end{cases} \tag{2.44}$$

where x is a sample integration (Gauss) point, x^* is the point on the crack closest to x, and n is the unit outward normal to the crack at x^*.

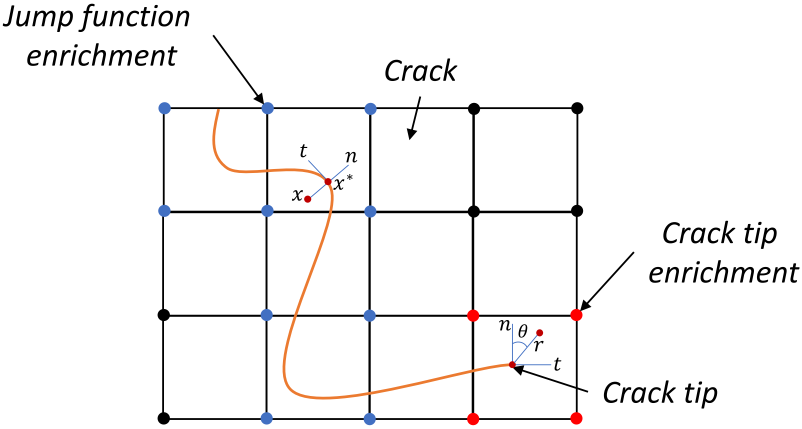

Figure 2.16: Normal and tangential coordinates for a smooth crack using XFEM.

As Figure 2.16 shows, some elements are not entirely separate. In these cases, the discontinuous jump function cannot be used to enrich the domain. Flemming et al. [63] have shown that asymptotic crack tip functions in an isotropic elastic material contained within the span of the following four functions:

$$\left\{F_\alpha(r,\theta)\right\}_{\alpha=1}^{4} = \left\{\sqrt{r}cos(\tfrac{\theta}{2}), \sqrt{r}sin(\tfrac{\theta}{2}), \sqrt{r}sin(\tfrac{\theta}{2})sin\theta, \sqrt{r}cos(\tfrac{\theta}{2})sin\theta\right\} \tag{2.45}$$

where (r,θ), is a polar coordinate system with its origin at the crack tip and $\theta = 0$ is tangent to the crack faces. These functions forms the basis of the asymptotic field around the crack tip. These four functions are used for enriching the field near the crack tip, thus giving rise to four additional degrees of freedom in each direction at a node, in addition to standard degrees of freedom. It should be noted here that among the four the second function $\sqrt{r}sin(\theta/2)$ is discontinuous along the crack surfaces, thus giving the effect of required discontinuity in the approximation along the crack. The rest of the three functions are used for improving the solution near the crack tip. The inclusion of $\sqrt{r}$ term in the enrichment function gives the required singularity in the stress field. It is important to note that, with the use of the above mentioned near tip enrichment functions an element partially cut by the crack could be modelled [83].

2.5 Theory of Critical Distance (TCD)

The mechanical contact in the fretting problem is a stress raiser and, in this case, it is necessary to consider the effects of the stress gradient caused by the contact between the surfaces. In the 1930s, the development of the Theory of Critical Distance (TCD) was started with the works of [119, 131] in an attempt of predicting fatigue failures in metallic components in the presence of geometric features. Neuber proposed the Line Method (LM) and Peterson the Point Method (PM). Whitney and Nuismer [172] evaluating monotonic loading conditions were capable of defining the critical distance for the PM and LM through a relationship between the Mode I fracture toughness, K_{Ic}, and the tensile strength of smooth specimens. A decade later Tanaka presented a relation with an identical theoretical derivation and equally valid when applied to High Cycle Fatigue (HCF) [159]. Subsequently, several studies were carried out with the objective of proving the feasibility of predicting the fatigue limit resistance by using the TCD for HCF [96, 160, 162].

In general, the TCD define an effective stress, σ_{eff}, which is obtained through an averaging procedure over a volume surrounding the stress raiser. The method assumes that fatigue failures occurs when σ_{eff} exceeds a reference material strength. For 2D analysis, the volume method can be simplified by considering stress averages over an area, line (Area and Line Methods, respectively) or even at a point located at a critical distance, $L/2$, from the stress raiser (Point Method) [9]. The PM is used in this work, Figure 2.17. In this approach, for HCF, the critical distance assumes the following form [160]:

$$L = \frac{1}{\pi}\left(\frac{\Delta K_{th}}{\Delta\sigma_{-1}}\right)^2 \tag{2.46}$$

where, ΔK_{th} is the threshold stress intensity factor range and $\Delta\sigma_{-1}$ is the uniaxial plain fatigue limit range both obtained at fully reversed loading configurations.

On the other hand, the relation to estimate the critical distance to static strength of notched members is given by [161, 156]:

$$L_s = \frac{1}{\pi}\left(\frac{K_{Ic}}{\sigma_r}\right)^2 \tag{2.47}$$

where the K_{Ic} is the plane strain fracture toughness and σ_r is a reference material constant which may be equal to or greater than the ultimate tensile strength, S_{ut}.

As can be seen in Equations (2.46) and (2.47), the values of the critical distances under fatigue and static loading are usually different, which leads us to assume that, the critical distance, L_M, at medium-high cycle fatigue regime depends on the number of cycles to failure, N_f. The relationship between L_M and N_f can established by using a power law:

$$L_M(N_f) = AN_f^B \tag{2.48}$$

where the material constants A and B can be determined from a smooth specimen fatigue curve together with a fatigue curve for specimens containing geometrical features [156, 155]. Alternatively, in the absence of such data, constants A and B can be obtained by using Eqs. 2.46 and 2.47. Note that this approximation is very simple and inexpensive since the material constants are readily obtained from empirical relations [9].

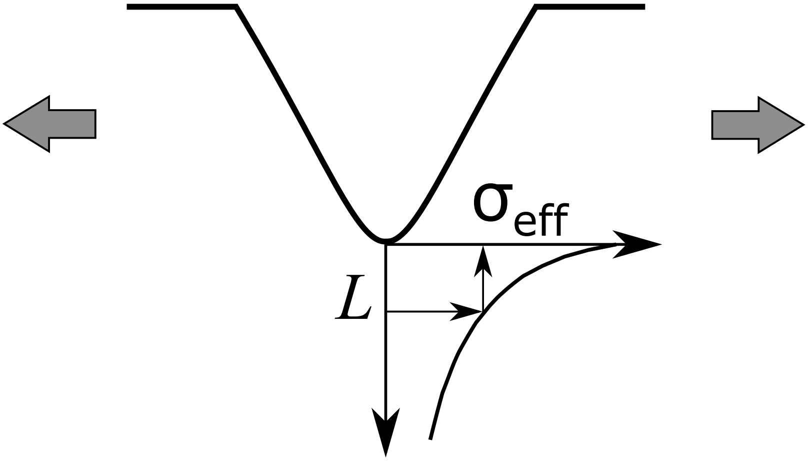

Figure 2.17: Schematic representation of the Point Method.

2.6 Contact mechanics

In practical engineering terms, it is well known that most of the mechanical components are in contact with each other. The concentration of tension caused by contact, especially in the critical regions of the body, makes the contact problem one of the great challenges of Solid Mechanics. When considering the law of friction, the complexity of the contact problem arises, which leads to the non-linear behavior of the connected bodies [83].

Fretting problems often involve the contact of highly complex components. In this configuration, the numerical method becomes mandatory and the finite element method is mainly the option of choice. However, this section focuses on the analysis of contact problems and, more specifically, on the contact between cylinders pressed on elastic half-plane. With a well-defined stress/displacement solution, this contact configuration is usually evaluated experimentally. In addition, these tests are easy to control, repeatable and insensitive to small manufacturing defects [81].

2.6.1 Surface tractions distributions

Considering the cylinder on plane contact configuration as shown in Figure 2.18, this section presents the analytical solutions for determining contact tractions. Hertz [77] showed that the pressure distribution developed between two cylindrical contact surfaces subjected to a static normal load P is given by

$$p(x) = -p_0\sqrt{1-\left(\frac{x}{a}\right)^2} \tag{2.49}$$

where p_0 is the peak pressure

$$p_0 = \frac{2P}{\pi a} \tag{2.50}$$

a is the contact semi-width

$$a = \sqrt{\frac{2PR^*}{\pi E^*}} \tag{2.51}$$

where

$$R^* = \left(\frac{1}{R_1} + \frac{1}{R_2}\right)^{-1} \tag{2.52}$$

For the cylinder on plane configuration, R^* is simply equal to the pad radius, because R_1 and R_2 are the radius of the bodies coming into contact. The equivalent Young modulus in Eq. 2.51 is given by

$$E^* = \left(\frac{1-\nu_1^2}{E_1} + \frac{1-\nu_2^2}{E_2}\right)^{-1} \tag{2.53}$$

where E and ν are, respectively, the Young modulus and the Poisson's ratio. The subscripts 1 and 2 refer to each body in contact.

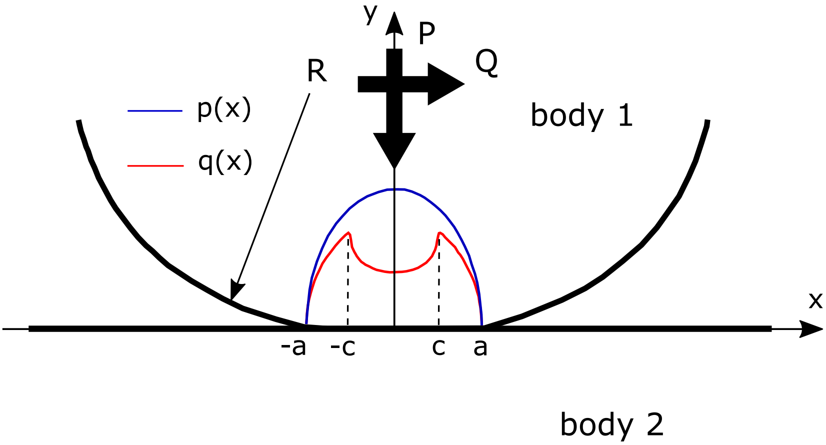

Figure 2.18: Schematic representation of the cylinder on plane contact configuration.

The solution to the contact problem including the tangential load Q was performed by Cattaneo [32] and independently by Mindlin [107]. When load Q is included, shear tractions are developed along the contact surface. Due to the elliptical distribution, the contact pressure tends to zero at the contact ends, this means that when the Q/P ratio is less than the coefficient of friction f, two symmetrical slip zones surrounding a central stick zone are formed along the contact surface. The mathematical solution for the shear traction distribution q can be seen as a perturbation of the solution for gross sliding:

$$q(x) = f p_0 \sqrt{1 - \left(\frac{x}{a}\right)^2} + q'(x) \tag{2.54}$$

where

$$q'(x) = \begin{cases} 0, & if \quad c \leqslant |x| \leqslant a \\ -f p_0 \frac{c}{a}\sqrt{1 + \left(\frac{x}{c}\right)^2}, & if \quad |x| \leq c \end{cases} \tag{2.55}$$

where a is the semi-width of the contact zone and the semi-width of the stick zone c is obtained imposing tangential equilibrium:

$$\frac{c}{a} = \sqrt{1 - \left|\frac{Q}{fP}\right|} \tag{2.56}$$

So far, the tangential traction $q(x)$ is effective only when the tangential load is applied monotonically from 0 to the maximum value Q_{max} (point A) (Figure 2.19). However, it is known that the tangential load Q changes over time under fretting conditions, as shown in Figure 2.19. After the tangential load from point A to point B is infinitesimally reduced, the entire contact surface experiences an adhesion state. Note that the action of the tangential traction force is opposite to the relative movement between the contact parts at this time; therefore, this condition is violated. A further reduction of the load Q to point C will result in the occurrence of reverse slip because, locally, the relative movement between the contact parts has been reversed. In the knew slip zones, shear traction will change from $fp(x)$ to $-fp(x)$. o capture these effects, a second correction term q'' has been added to the shear traction construction:

$$q''(x) = 2fp_0\frac{c'}{a}\sqrt{1 - \left(\frac{x}{c'}\right)^2} \tag{2.57}$$

For more details see Hills and Nowell [80]. Thus, the shear traction can be obtained as:

$$\frac{q(x)}{fp_0} = \begin{cases} -\sqrt{1-\left(\frac{x}{a}\right)^2}, & if\ c' < |x| \leqslant a \\ -\sqrt{1-\left(\frac{x}{a}\right)^2} + 2\frac{c'}{a}\sqrt{1-\left(\frac{x}{c'}\right)^2}, & if\ c < |x| \leqslant c' \\ -\sqrt{1-\left(\frac{x}{a}\right)^2} + 2\frac{c'}{a}\sqrt{1-\left(\frac{x}{c'}\right)^2} - \frac{c}{a}\sqrt{1-\left(\frac{x}{c}\right)^2}, & if\ |x| \leqslant c \end{cases} \tag{2.58}$$

where again, from the equilibrium of forces in the tangential direction:

$$\frac{c'}{a} = \sqrt{1 - \left(\frac{Q_{max} - sQ(t)}{2fP}\right)} \tag{2.59}$$

where one assumes $s = 1$ when one moves from Q_{max} towards Q_{min} and $s = -1$ during the reloading phase, i.e. from Q_{min} to Q_{max} in the tangential loading cycle, 2.19.

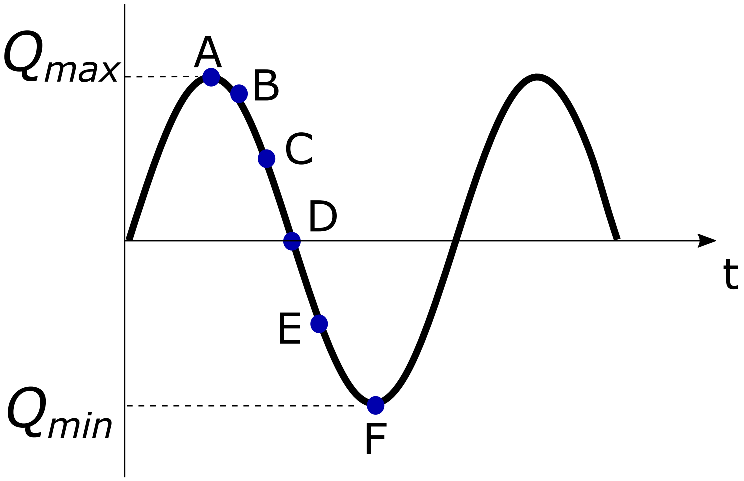

Figure 2.19: Variation of the tangential load Q over time.

Figure 2.20 shows the shear traction distribution when the tangential load Q moves from point A to point F in Figure 2.19. Even when the load Q is zero, there is still shear traction distribution along with the contact. This clearly shows the load history dependency in contact problems. It is also worth mentioning that the contact solutions presented in this section are valid for elastically similar bodies, that is, tangential loads do not modify the contact pressure distribution and normal loads do not generate shear tractions.

2.6.2 Bulk load effect on the shear traction distribution

The fretting fatigue problem includes the presence of a fatigue load in one of the bodies, called the bulk load. Let one considers here that only the specimen, body 2 in Figure 2.18 is subjected to a bulk load acting in phase with the tangential load Q. This bulk load generates a bulk stress $\sigma_b(t)$ on the specimen which will cause a mismatch in strain between the contacting parts. This mismatch will modify the Mindlin-type analyzes presented in the previous section. Now the perturbation solutions q' and q'' in Eq. 2.58 need to be rewritten as follows:

$$q' = -fp_0 \frac{c}{a}\sqrt{1-\left(\frac{x-e}{c}\right)^2} \qquad (2.60)$$

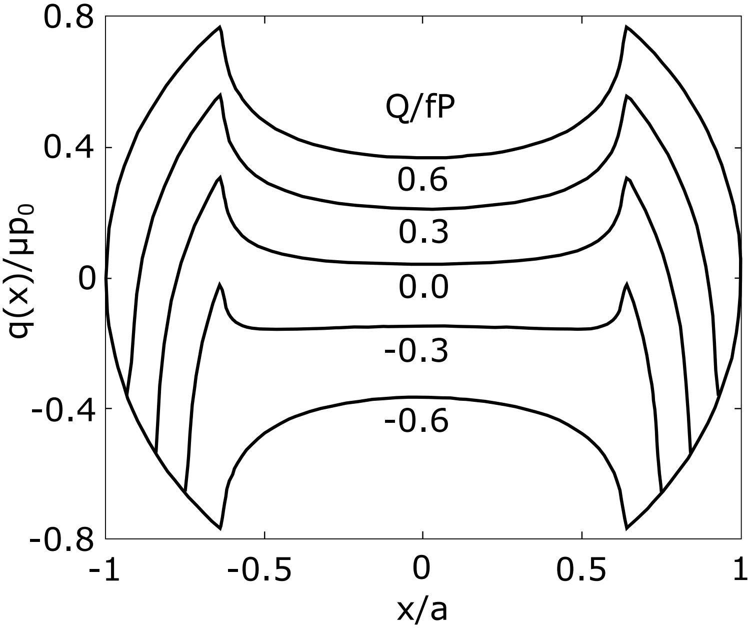

Figure 2.20: Shear traction distributions during a tangential cycle, $Q_{max}/fP = 0.6$.

and

$$q'' = 2fp_0 \frac{c'}{a} \sqrt{1 - \left(\frac{x - e'}{c'} \right)^2} \tag{2.61}$$

where the normalized offset terms e/a and e'/a are given respectively by:

$$\frac{e}{a} = \frac{\sigma_{b,max}}{4fp_0} \tag{2.62}$$

being $\sigma_{b,max}$ the maximum value reached by the bulk stress over a cycle and

$$\frac{e'}{a} = \frac{\sigma_{b,max} - s\sigma_b(t)}{8fp_0} \tag{2.63}$$

Figure 2.21 shows the shear traction distributions at different times when the sample is subjected to a sinusoidal bulk stress σ_b in phase with the tangential load Q (Figure 2.19). It is worth mentioning that these equations are only valid for small values of bulk fatigue load, and the following relationships must be observed: $e + c < a$ and $e' + c' < a$.

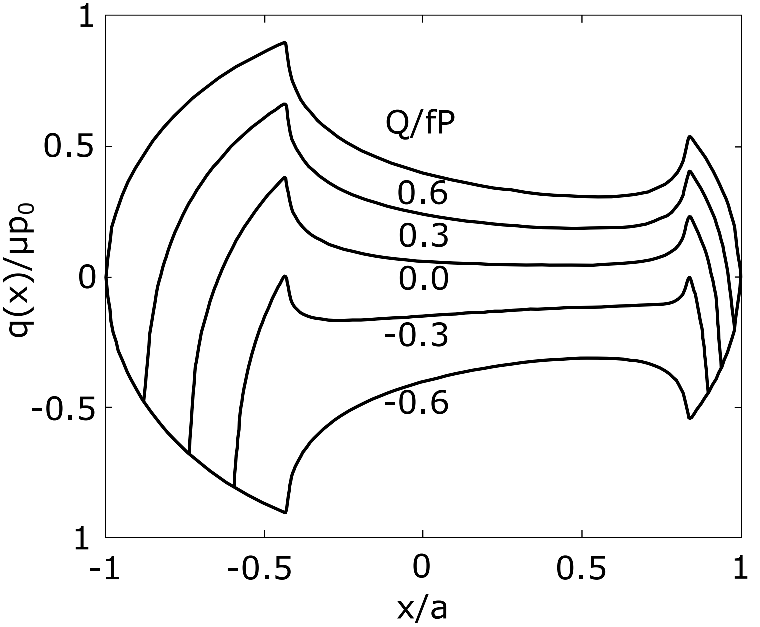

Figure 2.21: Shear traction distributions during a fretting cycle, $Q_{max}/fP = 0.6$ and $\sigma_{b,max}/fp_0 = 0.8$.

2.6.3 Sub-surface stress distributions

Muskhelishvili's potential is the most popular method used to calculate internal stress distribution in plane problems [113]. This potential, ϕ, is a function of position, z, which is a complex coordinate, i.e. $z = x + yi$. The potential itself can be obtained performing a full contour along the contact line:

$$\phi(z) = \frac{1}{2\pi i} \int_{contact} \frac{p(\zeta) - iq(\zeta)}{\zeta - z} ds \tag{2.64}$$

Once the potential ϕ is found, stress components can be defined by

$$\sigma_{xx} + \sigma_{yy} = 2\left[\phi(z) + \bar{\phi}(\bar{z})\right] \tag{2.65}$$

$$\sigma_{yy} - \sigma_{xx} + 2i\sigma_{xy} = 2\left[(\bar{z} - z)\phi'(z) - \bar{\phi}(z) - \phi(z)\right] \tag{2.66}$$

where $\phi'(z)$ implies differentiation with respect to z and $\bar{\phi}(z)$ implies taking the conjugate. For the cylinder contact configuration in the plane evaluated here, the pressure distribution has an elliptical profile. In addition, the shear traction distribution is a superposition of the elliptical traction distribution. In this configuration, two different potential expressions can be defined:

$$\phi^n(z) = \frac{1}{2\pi i}\int_{contact} \frac{p(\zeta)}{\zeta - z} ds \tag{2.67}$$

$$\phi^t(z) = \frac{1 - if}{2\pi i}\int_{contact} \frac{p(\zeta)}{\zeta - z} ds \tag{2.68}$$

where ϕ^n is obtained considering only the normal load, P, while ϕ^t is obtained considering gross sliding conditions. Therefore, solving the linear system described by Eqs 2.65 and 2.66, the following expressions for the σ_{xx} stress component can be obtained for instance:

- At maximum and minimum loads:

$$\begin{aligned}\frac{\sigma_{xx}(x,y)}{p_0} = \left(\frac{\sigma^n_{xx}\left(\frac{x}{a},\frac{y}{a}\right)}{p_0}\right) \pm \left(\frac{\sigma^t_{xx}\left(\frac{x}{a},\frac{y}{a}\right)}{fp_0}\right) \\ \mp \left(\frac{\sigma^t_{xx}\left(\frac{x-e}{c},\frac{y}{c}\right)}{fp_0}\right) + \frac{\sigma_b}{p_0}\end{aligned} \tag{2.69}$$

  where the signal combination + and - holds for the maximum load.

- During unloading and reloading phases:

$$\begin{aligned}\frac{\sigma_{xx}(x,y)}{p_0} = \left(\frac{\sigma^n_{xx}\left(\frac{x}{a},\frac{y}{a}\right)}{p_0}\right) \mp \left(\frac{\sigma^t_{xx}\left(\frac{x}{a},\frac{y}{a}\right)}{fp_0}\right) \\ \pm 2f\frac{c'}{a}\left(\frac{\sigma^t_{xx}\left(\frac{x-e'}{c'},\frac{y}{c'}\right)}{fp_0}\right) \mp f\frac{c}{a}\left(\frac{\sigma^t_{xx}\left(\frac{x-e}{c},\frac{y}{c}\right)}{fp_0}\right) + \frac{\sigma_b}{p_0}\end{aligned} \tag{2.70}$$

  where the signal combination -, + and - holds for the unloading phase.

Similarly, other stress components can be obtained.

2.7 Wear modelling and damage accumulation

2.7.1 Wear model

Among the most well-known wear models, especially in fretting fatigue applications, we can highlight for their wide use and easy applicability the local formulations of Archad's equation [45, 104] or the dissipated friction energy [64, 47].

Archad's equation for sliding wear can be expressed as [12]:

$$\frac{V}{S} = K\frac{P}{H} \tag{2.71}$$

where P, S and V are the normal contact load, total relative slip, and volume of material removed, respectively. K is the dimensionless wear coefficient and H is the material hardness. In terms of one locally expression, the wear can be written applied for an infinitesimal area as:

$$dh = k_w p(x) ds \tag{2.72}$$

where $p(x)$ is contact pressure and k_w the local wear coefficient and dh is the material removal depth for a given incremental relative slip ds.

While Archad's equation correlates surface wear with normal contact load, total relative slip, and material hardness the friction energy wear law consists in relating the total wear volume to the accumulated friction energy dissipated on the contact interface.

$$V = \alpha \sum E_d \tag{2.73}$$

where E_d is the friction energy dissipated during a fretting cycle and α is the energy wear coefficient. Locally, for an infinitesimal area, the wear depth can be expressed as:

$$dh = \alpha q(x) ds \tag{2.74}$$

where $q(x)$ is the contact shear traction.

The equations 2.72 and 2.74 can be used to compute wear locally. However, in the context of an FE code it is necessary to make some changes. From a practical point of view, the simulation of all the desired wear cycles is not feasible. In this case, a strategy commonly adopted is to compute the wear during a fretting cycle and then multiply it by the jumping factor ΔN assuming that the wear is nearly constant for ΔN wear cycles. This way, each contact surface node will be updated after the application of the i_{th} wear block ΔN as follows:

- Archard's law:

$$\Delta h_{i,j} = \sum_{k=1}^{n_{inc}} k_w p(x_j, t_k) \Delta s(x_j, t_k) \Delta N \tag{2.75}$$

- Frictional dissipated energy:

$$\Delta h_{i,j} = \sum_{k=1}^{n_{inc}} \alpha q(x_j, t_k) \Delta s(x_j, t_k) \Delta N \tag{2.76}$$

where $\Delta h_{i,j}$ is the wear depth increment of the node j located at the contact surface with position x_j, α is the energy wear coefficient, k_w is the local wear coefficient and n_{inc} is the total number of load increments over a fretting cycle. The contact variables $p(x_j, t_k)$, $q(x_j, t_k)$ and $\Delta s(x_j, t_k)$ are respectively, the pressure distribution, the shear traction and the contact relative slip increment for the node j at the time increment t_k. The total required number of wear cycles, N_t, can be split in n_w wear blocks, where each block corresponds to ΔN wear cycles, i.e. $n_w = N_t/\Delta N$. Thus, the total wear depth at N_t cycles for the node j is given by:

$$h_j = \sum_{i=1}^{n_w} \Delta h_{i,j} \tag{2.77}$$

2.7.2 Damage accumulation method

With the evolution of wear, the stresses and strains change in each simulated fretting cycle. Thus, it is necessary to calculate the damage in each wear step. Miner's linear cumulative damage rule [129, 108] was used in this work to predict material failure. For a material sub-surface point $\mathbf{x}$, the total cumulative damage associated with the n^{th} wear step is given by:

$$D_{f,n}(\mathbf{x}) = \sum_{i=1}^{n} \frac{\Delta N}{N_{f,i}(\mathbf{x})} \tag{2.78}$$

where $N_{f,i}$ is the fatigue life expected for a given stress state, i.e. a multiaxial fatigue model is used after determining the stress state $\sigma(\mathbf{x}, t)$ for given material point $\mathbf{x}$ and time instant t over the i^{th} fretting cycle to predict the fatigue life $N_{f,i}(\mathbf{x})$. It is important to note that $N_{f,i}$ can be the life for crack nucleation or failure, it depends on how the fatigue parameter used was calibrated. The centroid of the elements was defined as the position to compute the damage defined by Eq.(2.78). Due to the evolution of wear, the contact surface is constantly changing, thus the position of the nodes and consequently the centroid of the elements are changed. Therefore, the following numerical scheme was adopted: as can be seen on Figure 2.22, after each i^{th} fretting cycle simulation, the damage value on the $(i-1)^{th}$ fretting cycle was interpolated from the $(i-1)^{th}$ element centroids position to the new i^{th} element centroids location. In view of this, the actual damage field distribution at the i^{th} damage increment can be expressed as:

$$D_{f,i} = D^{*}_{f,i-1} + \Delta D_{f,i} \tag{2.79}$$

where $D^{*}_{f,i-1}$ is the damage field from the previous fretting cycle simulation $(i-1)^{th}$ interpolated to the position of the element centroid points at the i^{th} fretting cycle.

Note that although surface wear is considered in both specimen and pad, the damage generated in the material is computed only in the specimen, as shown in Figure 2.23. Damage is computed at the center of all elements near the contact region. The TCD is used to account for geometric features, this means that the damage taken at the center of the elements is interpolated to obtain an approximate value considering a distance $L/2$ from the contact surface, red dots on Figure 2.23 . The same is true when using L_M (critical distance as a function of life). The wear process is stopped when the damage accumulated at some point in $L/2$ or L_M equals 1.

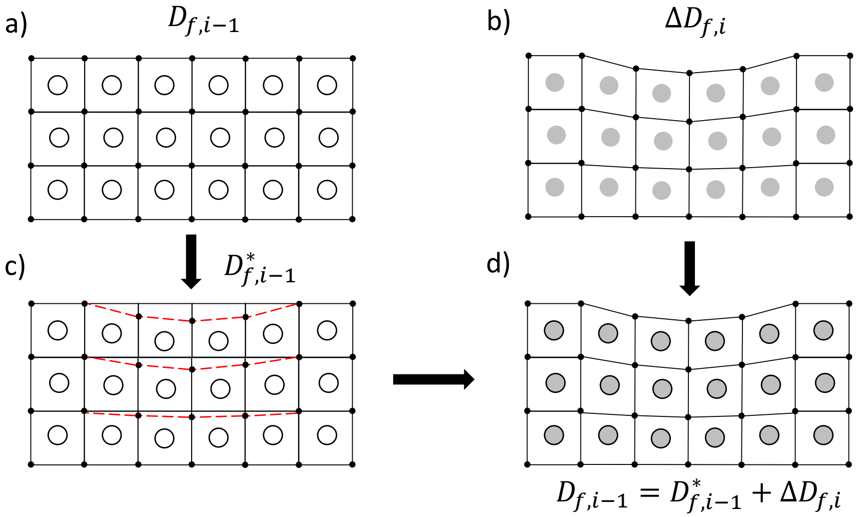

Figure 2.22: Illustration of the strategy used in order to compute the damage considering wear process: (a) accumulated damage at the centroid of the elements at the $(i-1)^{th}$ simulated fretting cycle, (b) incremental damage at the centroid of the elements at the i^{th} simulated fretting cycle, (c) accumulated damage at the $(i-1)^{th}$ simulated fretting cycle extrapolated to the position of the element centroids at the i^{th} simulated fretting cycle and (d) accumulation of the total damage at the i^{th} simulated fretting cycle.

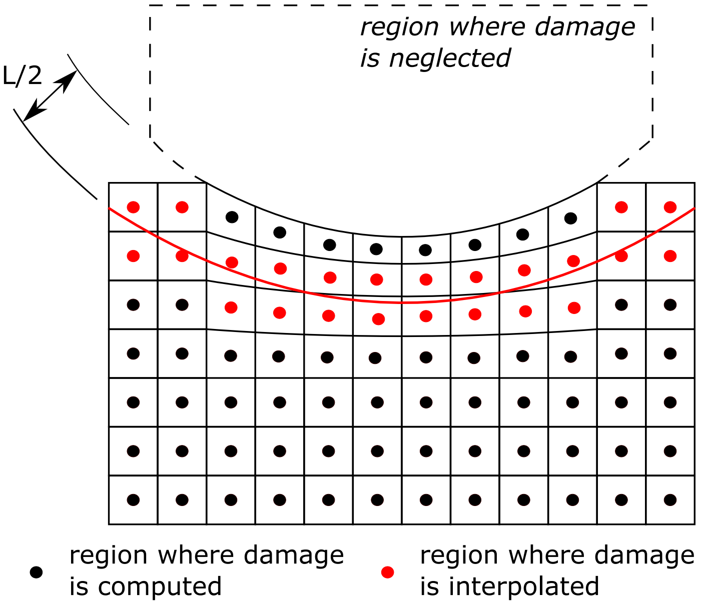
region where damage
is neglected
L/2
region where damage
is computed
region where damage
is interpolated

Figure 2.23: Damage accumulation procedure considering wear.

Chapter 3

Experimental work

“This chapter presents the experimental results for the characterization of aluminum alloy Al 7075-T651 and discusses the experimental methods used to study fretting fatigue behavior under variable amplitude loading”

3.1 Material characterization

3.1.1 Aluminum alloy 7075-T651

The material used in this research was aluminum alloy 7075 with T651 heat treatment. Developed in the 1930s by the Japanese company Sunimoto Metal to be used in the fuselage of the Mitsybishi A6M2 Reisen “zero” fighter [150], it had its first application in the industry only in 1943 by ALCOA [17]. Due to its high strength and low specific mass, it continues to be widely used in the aeronautical industry. Table 3.1 presents the chemical composition of the alloy Al 7075-T651.

Table 3.1: Chemical composition of Aluminum Alloy 7075-T651 (%weight) (ASM International).

Si	Fe	Cu	Mn	Mg	Cr	Zn	Ti	Al	Outros
0.4	0.5	1.2-2.0	0.3	2.1-2.9	0.18-0.28	5.1–6.1	0.2	87.17-99.00	0.05-0.15

The aluminum alloy with the designation T651 undergoes solubilization treatments, artificial aging and subsequent stress relief by stretching. The process for obtaining the alloy consists of heating to a temperature of 480°C, cooling and then reheating to a temperature of 120°C in order to artificially age it. Finally, there is stress relief by stretching [38].

3.1.2 Metallographic analysis

To carry out the metallographic analysis of the 7075-T651 aluminum alloy, small sample cubes of the material were removed. Then, the samples (cubes) were cold embedded in transparent resin, leaving the faces to be analyzed exposed, these perpendicular to the L, S and T directions, as shown in Figure 3.1.

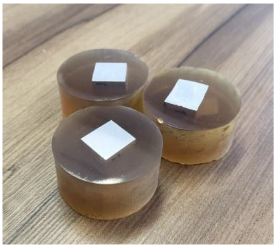

Figure 3.1: Al 7075-T651 alloy samples embedded in resin.

The surface of the samples was polished using a manual polisher model Polipan-U, from Pantec. The surface preparation process consists of two steps: sanding and polishing. The samples were sanded using silicon carbide water sandpaper with granulometry 220, 320, 400, 600, 800, 1200, and 2000. Then, they were polished with diamond paste (3 μm). The chemical attack on the surface was carried out after sanding and polishing with Keller (2 mL HF + 3 mL HCl + 5 mL HNO_3 + 190 mL H_2O), as indicated in the standard ASTM E407-07 [14]. The duration of exposure to Keller on surfaces was between 10 and 20 seconds for each sample. Finally, the images of the microstructure of each sample were acquired using an Olympus laser confocal microscope, model OLS4100, with the aid of the Olympus Stream application.

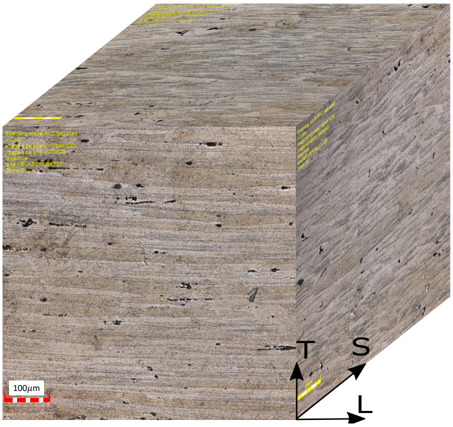

Figure 3.2: Three-dimensional image formed with metallography in each lamination direction (T, S, and L).

In order to clearly visualize how the morphology of the grains varies with the analyzed direction, the images obtained with a microscope for each of the directions were placed on three faces of a cube, Figure 3.2. Thus, it can be observed how the grains are arranged in the aluminum alloy analyzed. In figure 3.3(a), there is a micrograph in the lamination direction (L), where longitudinally elongated grains can be observed with an average size of 528μm, and a width of 17μm. Figure 3.3(b) show the grains in the short transverse direction (S), where the average size of the grains in the rolling direction is 263μm with 40μm of width. Finally, Figure 3.3(c) present the results of the long transverse direction (T). As can be seen, the average grain size is 201μm$\times$28μm. As the stretching was done in the alloy, there is a more homogeneous distribution of precipitates. According to Zhao and Jiang [176], these precipitates (black dots) are particles of $Cr_2Mg_3Al_{18}$ and $(Fe, Mn)Al_6$.

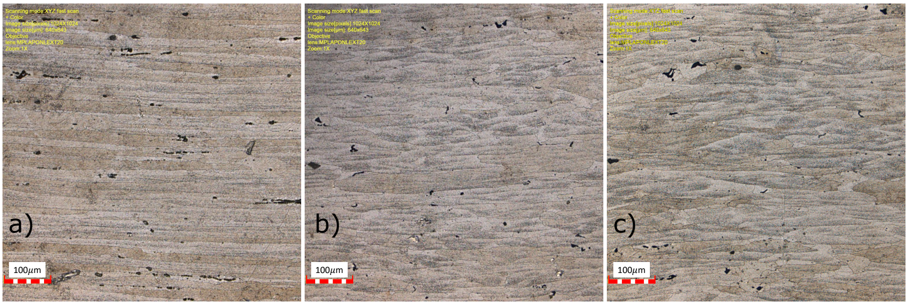
Scanning mode:XYZ fast scan
+ Color
Image size[pixels]:1024X1024
Image size[µm]: 640x643
Objective
lens:MPLAPONLEXT20
Zoom:1X
a)
100µm
Scanning mode:XYZ fast scan
+ Color
Image size[pixels]:1024X1024
Image size[µm]: 640x643
Objective
lens:MPLAPONLEXT20
Zoom:1X
b)
100µm
c)
100µm

Figure 3.3: Micrograph of Aluminum Alloy 7075-T651, in L (a), S (b), and T (c) direction at 200x increase.

3.1.3 Hardness Test

Small samples such as those in Figure 3.1 were used for penetration hardness tests. For this, the Zwick Roell ZHU 250 durometer presented in Figure 3.4 was used.

Figure 3.4: Durometer Zwick Roell ZHU 250.

The penetration hardness test (Rockwell, Vickers, Brinell) consists of applying a load to the surface of the material, with the penetration tip (indenter), leaving an impression/mark on the sample, whose shape will depend on the indenter used. The measured hardness was Rockwell Hardness, and the test was performed in accordance with ASTM E18-19 [50]. Therefore, as the material studied is an aluminum alloy, a spherical indenter with a diamond tip of 1/16 in (1.588 mm) was used for the test on the Rockwell Hardness B scale to leave the impression on the piece and, in addition, a load of 100 kgf was applied to the sample. Each sample had its hardness measured five times.

The hardness test was performed on two samples of aluminum alloy. Each sample had its hardness measured five times, at random points on the surface of the L-T plane. The test showed little variation in the values found for hardness at these points. By calculating the average of these values, the hardness of the aluminum alloy studied is 88.7 HRB. Compared to the value found in ASM 1990 for Rockwell Hardness of Aluminum alloy 7075 T-651, the difference is only 1%.

3.1.4 Tensile tests

In order to obtain the monotonic mechanical properties of the Aluminum alloy 7075-T651, three tensile tests were performed. For this, the servo hydraulic machine MTS 810 was used, Figure 3.5. The specimens tested were manufactured in accordance with ASTM E8/E8M-16 [54], and machined in the alloy rolling direction. The dimensions of the specimens, in millimeters, are shown in Figure 3.6. The specimens used in fatigue tests have the same dimensions. The technical drawing is available in Appendix A.

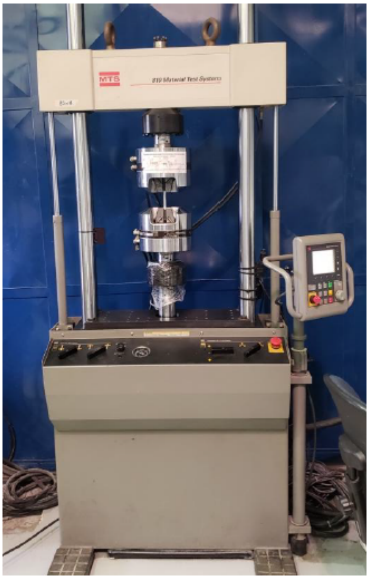

Figure 3.5: Servo hydraulic machine MTS 810.

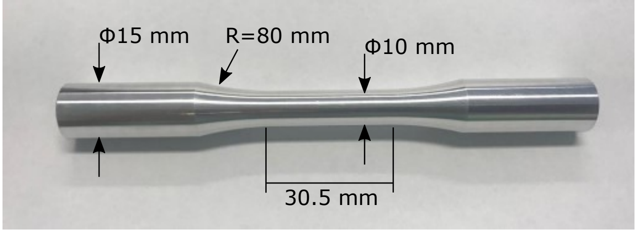

Figure 3.6: Fatigue and tension test specimen.

The tensile test was carried out under displacement control (a rate of 2mm/min) up to the final fracture. To obtain a more accurate deformation of the specimen, a model 634.11F-24 strain gauge was used, illustrated in Figure 3.7. Due to the operating limitations of this accessory, at a given moment of the test, the strain gauge was uncoupled from the specimen and the test resumed normally.

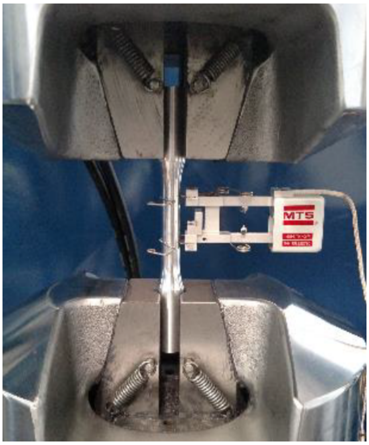

Figure 3.7: Extensometer attached to the specimen during the tensile test.

Three tensile tests were conducted and their respective stress-strain curves are depicted in Figure 3.8. The mechanical properties are summarized in Table 3.2. It is noticed that the values found in the test are consistent with the literature.

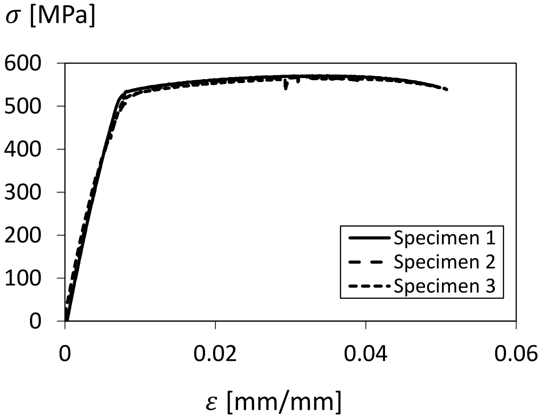

Figure 3.8: $\sigma - \varepsilon$ diagram of Al 7075-T651 alloy.

Table 3.2: Mechanical properties of AL 7075-T651.

Monotonic properties	
Young's modulus, E	68 GPa
Yield strength, σ_y	506 MPa
Tensile strength, σ_u	570 MPa

3.1.5 Fatigue Test

Fatigue tests followed the protocols required by ASTM E739 and E466 [53, 51]. The specimens shown in Figure 3.6 were subjected to cyclic loading with loading ratio $R = -1$ until failure. The MTS 809 axial/torsional servo-hydraulic machine, Figure 3.9, with a capacity of ± 100 kN in the axial direction and ± 1100 Nm of torque was used for the uniaxial and torsional fatigue tests.

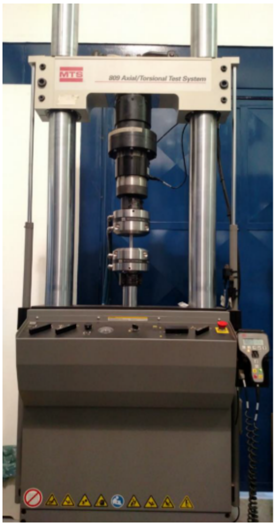

Figure 3.9: Photo of the axial-torsional MTS 809 servo-hydraulic test rig.

A total of 13 specimens were used to obtain the S-N curve. Results are reported in Table 3.3. Figure 3.10 shows the final S-N curve. Note that the uniaxial plain fatigue range, $\Delta\sigma_{-1}$, to loading ratio R= -1, is equal to 427MPa.

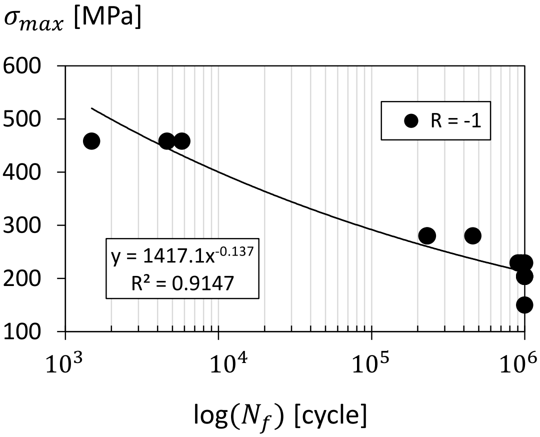

Figure 3.10: Al 7075-T651 alloy S-N curve.

Table 3.3: Results from uniaxial fatigue tests.

Specimen	f **[Hz]**	σ_a **[MPa]**	$N_f \times 10^3$ **[cyles]**
1	0.5	458	1.49
2	0.5	458	5.77
3	0.5	458	4.62
4	7.5	280	232.14
5	7.5	280	458.31
6	7.5	280	229.50
7	7	280	317.43
8	7	229	947.22
9	7	229	904.68
10	7	229	$10^3 >$
11	8	204	$10^3 >$
12	8	204	$10^3 >$
13	8	204	$10^3 >$

Tests under pure torsion were also performed. The load ratio was $R = -1$. Twelve specimens were used to obtain the τ-N curve. The data of each test are presented in Table 3.4. Figure 3.11 shows the τ-N curve. Note that the pure torsion fatigue range, $\Delta\tau_{-1}$, to loading ratio R= -1, is equal to 337.35MPa.

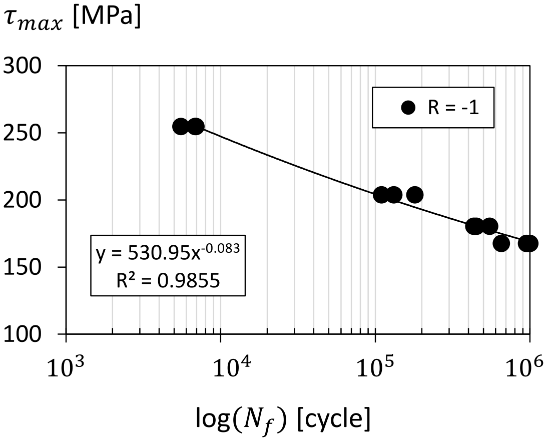

Figure 3.11: Al 7075-T651 alloy τ-N curve.

Table 3.4: Results from pure torsion fatigue tests.

Specimen	f **[Hz]**	τ_a **[MPa]**	$N_f \times 10^3$ **[cycles]**
1	5	255	6.85
2	5	255	6.93
3	5	255	5.54
4	5	204	131.93
5	5	204	180.37
6	5	204	109.88
7	5	180	434.16
8	5	180	450.32
9	5	180	549.95
10	7	168	$10^3 >$
11	7	168	654.66
12	7	168	951.64

3.1.6 Curve da/dN vs ΔK and ΔK_{th}

Crack propagation tests were performed on an MTS 810 servo-hydraulic machine. The specimen is pin-loaded by special clevises, described by ASTM E399 as Tension Testing Clevis. Figure 3.12 shows the alignment of the grips and the specimen. The software used to collect experimental data was MTS Fatigue Crack Growth. The tests followed the ASTM E647 standard [52], as well as the designing and fabrication of the specimens. Figure 3.13 presents the dimensions in millimeters of the specimen known as Compact tension, CT. The technical drawing is available in Appendix A.

An essential aspect of the test is associated with the accuracy of the measurement of crack-mouth-opening displacement (CMOD) as a function of the applied load and the stiffness of the system. This displacement is measured with the clip gage that is attached to sharp knife edges, illustrated in Figure 3.14. The knife edges can either be machined into the specimen, which was done in this work or attached to the specimen at the crack mouth. The measurement of the CMOD is an important parameter to be controlled during the test, as it is related to the crack length, a. Therefore, to correctly measure the crack length value it is necessary to ensure that the CMOD and loading values are accurately measured.

To carry out the tests, it is necessary to create a pre-fatigue crack. According to the E647 standard in the final stage of pre-crack generation (2.5% missing for the maximum crack size), the stress intensity factor K_I cannot be greater than

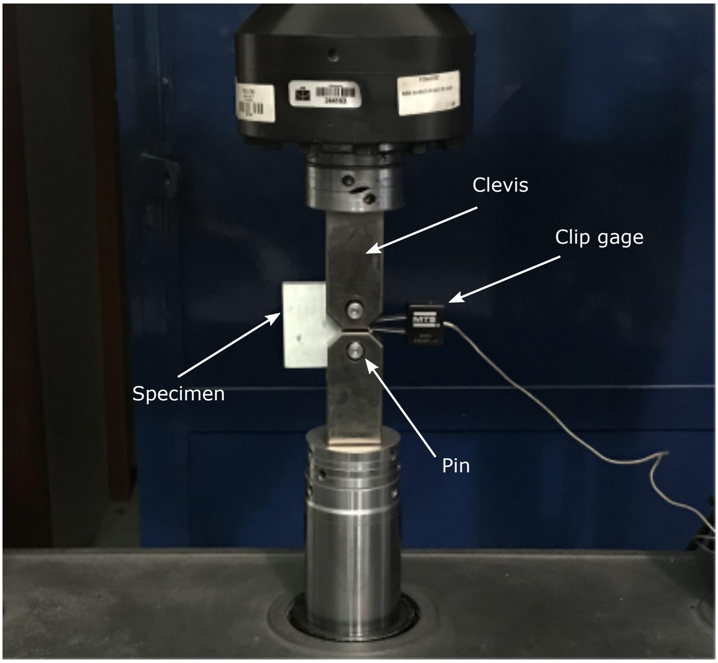
Clevis
Clip gage
Specimen
Pin

Figure 3.12: Apparatus for testing compact specimens.

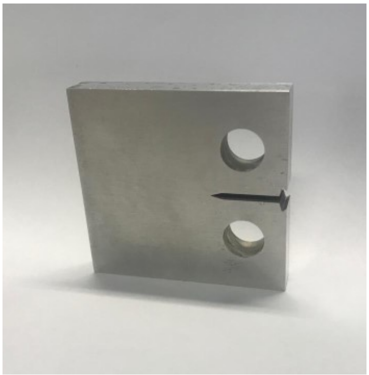

Figure 3.13: Picture of the compact tension specimen.

60% of the fracture toughness of the material, K_{Ic}. For all tests, the pre-crack size was 2 mm.

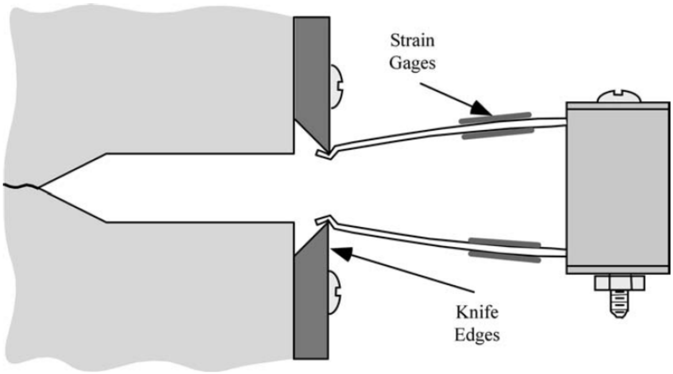

Figure 3.14: Measurement of the crack-mouth-opening displacement with a clip gage [4].

The curves da/dN vs ΔK were obtained with tests of constant amplitude load where the ΔK is increasing. During all tests, a constant load of 1.5 kN was used with load ratio R= 0.1. Figure 3.15 shows the results of the da/dN vs ΔK curves. A total of 6 tests were conducted, 3 performed in the S-L lamination direction, 2 in the L-T direction, and 1 in the T-L direction.

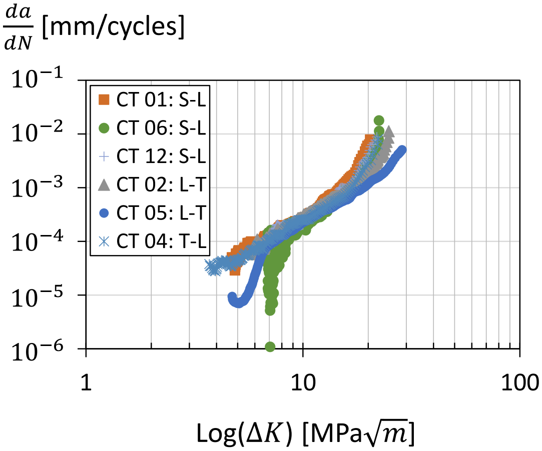

Figure 3.15: Curve da/dN vs ΔK

To obtain the ΔK_{th}, tests were performed with decreasing ΔK. Where, K_{max} at the beginning of the test was 5 MPa$\sqrt{m}$ with a loading ratio R=0.1. The value of K_{max} decreases until the crack propagation rate is close to 10^{-7} mm/cycle. As shown in Figure 3.16, 3 tests were performed, 2 in the S-L direction and 1 in the L-T direction.

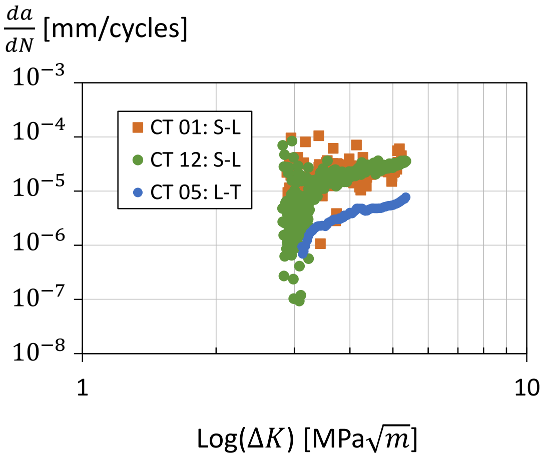

Figure 3.16: Curve da/dN vs ΔK to obtain the ΔK_{th}.

Table 3.5 shows the values of the constants C and m (Paris' constants), as well as the propagation threshold ΔK_{th}.

Table 3.5: Results from crack propagation tests.

CT	**Direction**	ΔK_{th} $(MPa\sqrt{m})$	**C** $(\frac{mm}{cycle}/(MPa\sqrt{m})^m)$	**m**
1	S-L	2.88	5×10^{-7}	2.81
2	S-L	-	3×10^{-7}	2.89
3	S-L	2.45	5×10^{-7}	2.72
1	L-T	-	5×10^{-7}	2.74
2	L-T	2.9	5×10^{-7}	2.59
1	T-L	-	8×10^{-7}	2.57
Mean		**2.74**	5.17×10^{-7}	**2.72**

3.2 Fretting fatigue tests

3.2.1 Experimental set-up

The testing machine used in this work was the MTS 322 Test Frame. This fretting fatigue rig was modified by Almeida et al. [1] to work with four uncoupled actuators, i.e., it is possible to independently control all the loads involved in the fretting tests (bulk, normal and tangential loads). It means that the loads can vary with time in-phase or out-of-phase, and they can also be applied in their waveforms synchronously or asynchronously. The Basic Test-Ware program was used to control the tests. The University of Brasília laboratory also uses the Multipurpose Elite program. Both offer numerous control features and allow a wide range of tests to be conducted on this machine. The programs also have a practical and effective system of data acquisition and monitoring of variables throughout the test. It is worth mentioning that, despite not being part of the scope of this research, the apparatus was also designed to perform tests at high temperatures (up to 750 °C).

The schematic drawing in Figure 3.17 depicts the main parts of the fretting apparatus. As can be seen, there is in the machine rig a fixed and movable jaw (6 and 7) that held the flat dog-bone tensile specimen between them, and the pad holders (12) are mounted on a set of linear bearings (10) which allows the application of varying normal loads or displacements to the pads. The movable jaw (7) is linked to a load cell (4) and to a hydraulic actuator (3) capable of applying loads up to 250 kN. This one is responsible for applying the fatigue load on the specimen. The fretting apparatus is linked to the load cell and LVDT sensor (2) and to the hydraulic actuator (1), which can provide fretting loads up to 100 kN. And finally, the two MTS hydraulic actuators (9) are responsible for applying the normal load to the fretting pads (11). Each of these actuators can apply up to 15 kN force under cyclic or static conditions. More details of the fretting apparatus design can be seen in the work done by Almeida et al. [1]. Figure 3.18 shows a photo of the four actuators fretting fatigue rig.

As previously mentioned, the specimens used in the fretting fatigue tests are of the flat dog-bone type. Figure 3.19 shows a photo of the specimen (a) and pad (b) used in the tests, both were made using the same material (Al 7075-T651). All specimens have a cross-section of 13mm×13mm and the shoes have a radius of R= 70mm. The technical drawing is available in Appendix A.

Before the tests, the specimens and shoes had their measurements and roughness inspected. The roughness measurement was performed with the Olympus LEXT OLS4100 confocal laser microscope and following the NBR ISO 4287/2002

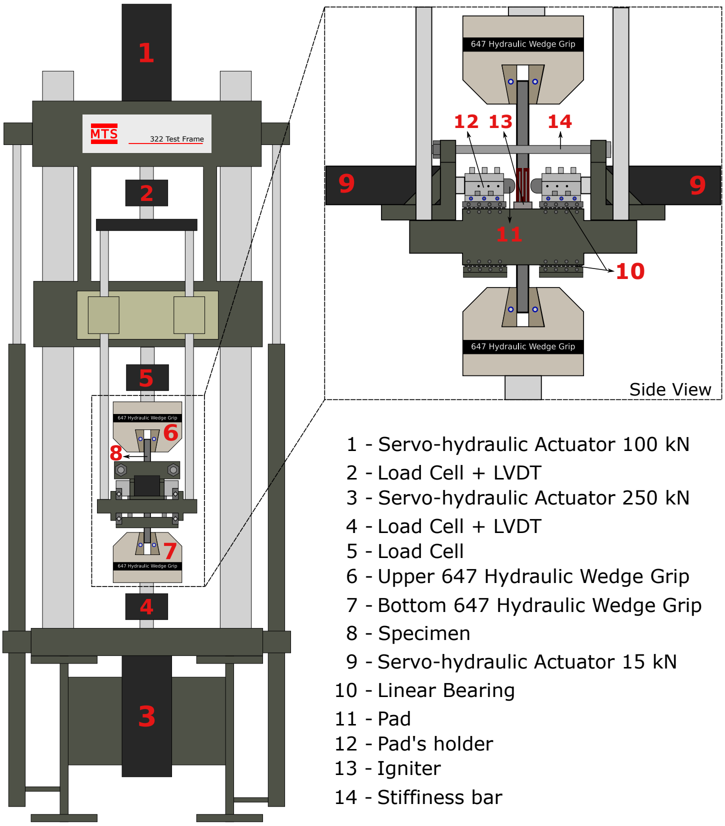
1
MTS
322 Test Frame
2
5
647 Hydraulic Wedge Grip
6
8
7
647 Hydraulic Wedge Grip
4
3
647 Hydraulic Wedge Grip
12 13
14
9
9
11
10
647 Hydraulic Wedge Grip
Side View
1 - Servo-hydraulic Actuator 100 kN
2 - Load Cell + LVDT
3 - Servo-hydraulic Actuator 250 kN
4 - Load Cell + LVDT
5 - Load Cell
6 - Upper 647 Hydraulic Wedge Grip
7 - Bottom 647 Hydraulic Wedge Grip
8 - Specimen
9 - Servo-hydraulic Actuator 15 kN
10 - Linear Bearing
11 - Pad
12 - Pad's holder
13 - Igniter
14 - Stiffiness bar

Figure 3.17: Schematic of the four actuators fretting fatigue rig [1].

standard. Three measurements were performed in the center of each side of the specimen and on the surface of the radius of the shoes. The roughness values obtained were lower than 0.4μm.

3.2.2 Test procedure

Before starting the fretting fatigue tests, the contact surfaces are cleaned with ethyl alcohol. Then, the specimen is set in the jaws of the testing machine. Before closing and pressurizing the jaws, it is necessary to ensure the alignment of the specimen with the jaw walls to avoid twisting the specimen. At this stage the mean fatigue load is applied in the absence of the pads.

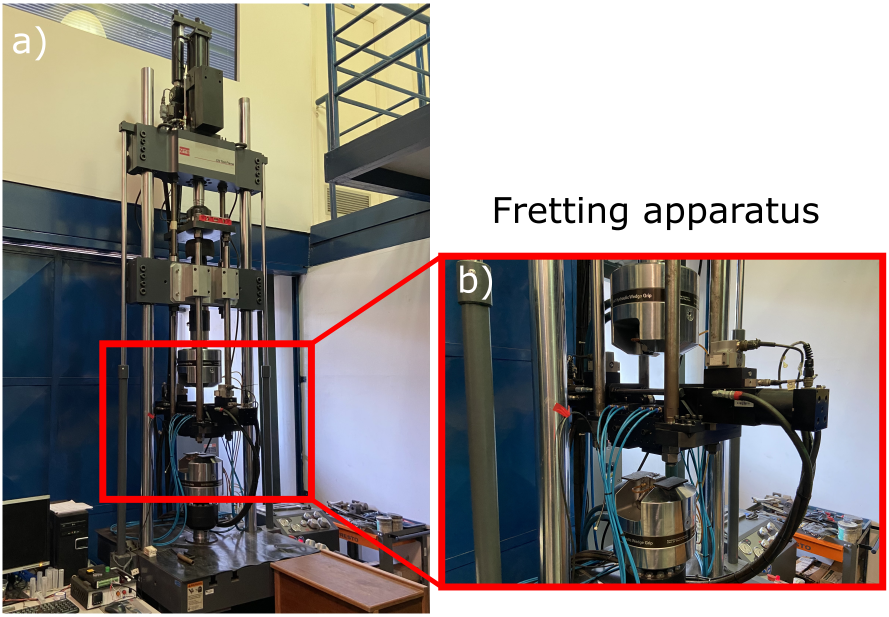

Figure 3.18: Photos of the four actuators fretting fatigue rig (a), and fretting apparatus(b).

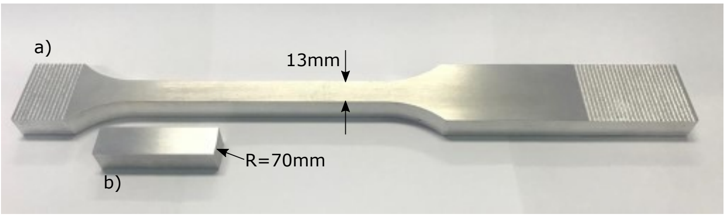

Figure 3.19: The dog-bone specimen (a), and fretting pad (b) used for fretting fatigue tests.

The pad must be positioned so that the sides of the specimen are aligned with those of the pad. It is also necessary that the pad is perpendicular to the specimen to ensure a uniform pressure field. A Fujifilm Prescale Medium pressure film was used to check alignment. Figure 3.20 shows the marks taken at two different positions of the fretting pad. A good pad alignment results in a linear and homogeneous pressure distribution, as shown in Figure 3.20(a). In this way, crack nucleation begins at the contact center and the crack propagates through the specimen up to the final rupture. On the other hand, a misalignment as in Figure 3.20(b) causes an anomalous and faster crack initiation due to the edge effect phenomenon, and eventually crack advances from the edge of contact (a behavior known as corner crack) towards the opposite and lateral side of the specimen performing a diagonal crack path advance. These tests are invalid.

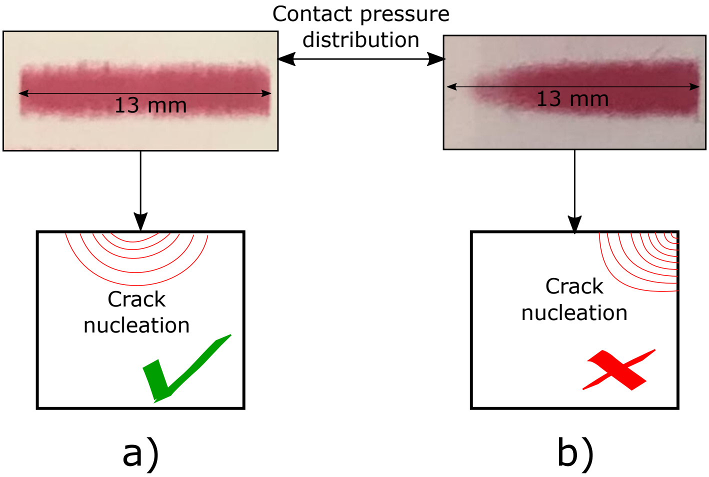

Figure 3.20: Fretting fatigue contact alignment analysis using pressure film: the well aligned (a) and misaligned contact (b) between fretting pad and fatigue specimen.

After tightening the screws on the pad's holder and aligning the assembly, the normal contact load can be applied. The following test steps are carried out with the help of the Basic Test-Ware program. Initially, a test is performed in displacement control on the 100kN actuator (fretting actuator) applying only the mean bulk fatigue load and constant normal contact load. In this test, the fretting actuator displacement amplitude is gradually increased until the load read from this actuator is equal to or slightly greater than the maximum tangential load desired during the fretting fatigue test. Upon reaching this desired load, the test is allowed to run for another 5,000 cycles. This step is important to adjust the friction coefficient of the contact surface, thus reducing the probability of the test failing due to gross slip when performed in force control. After stabilization of the coefficient of friction, the load control test begins. As stated before, the mean fatigue load is applied even before the pad alignment and maintained throughout the test. Then the normal load is applied. Finally, there is the simultaneous application of the fatigue and tangential-fretting loads. A sinusoidal wave shape was used.

Although the vast majority of laboratory tests are performed keeping the amplitude of the bulk and fretting loads constant during the test, it is expected that in most practical applications the loading history is random and quite complex. Therefore, this work aims to investigate the effects of a variable tangential load and of the sequence of application of these different tangential loading blocks on the life of the Al 7075-T651 specimens. In this setting, we have designed new tests consisting of two blocks of the fretting load, as illustrated in Figure 3.21.

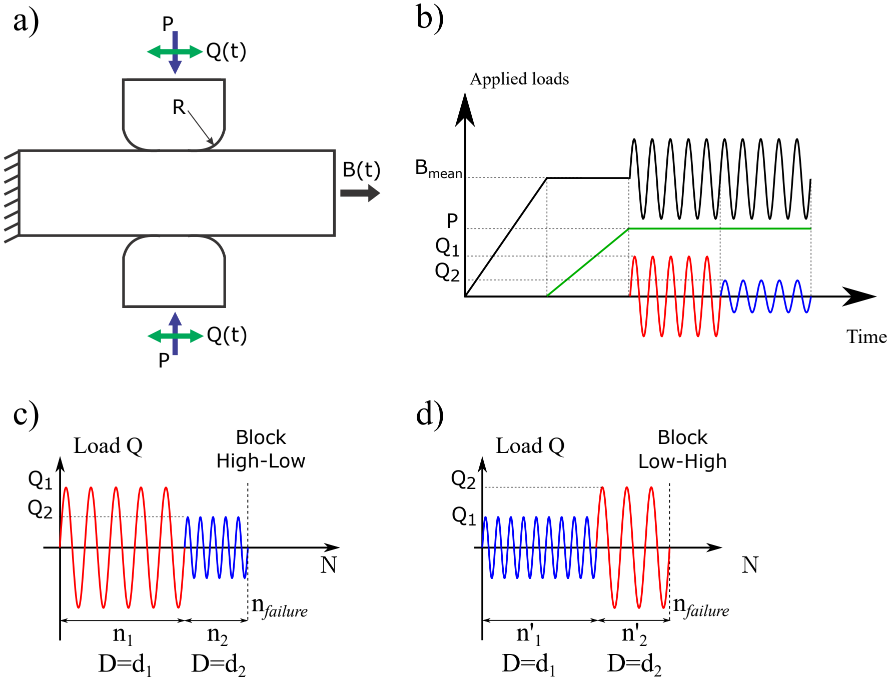
a)
P
Q(t)
R
B(t)
Q(t)
P
b)
Applied loads
B_mean
P
Q1
Q2
Time
c)
Load Q
Block
High-Low
Q1
Q2
N
n_failure
n1
n2
D=d1
D=d2
d)
Load Q
Block
Low-High
Q2
Q1
N
n_failure
n'1
n'2
D=d1
D=d2

Figure 3.21: Schematic representation of the application of loads in the fretting fatigue test: (a) representation of where each load is applied to the specimen, (b) order of application of test loads, and the representation of the H-L (c) and L-H (d) loading blocks.

Note that only the tangential load amplitude, Q will vary. The amplitude of the bulk fatigue load, F_b, is the same during all tests and the normal load P is always constant. In Figure 3.21(c) one has a High-Low (H-L) loading sequence, where, for a given number of cycles n_1 and n_2 the amplitudes of the tangential load considered in the analysis are Q_1 and Q_2, respectively, with $Q_1 > Q_2$. On the other hand, in Figure 3.21(d), the Low-High (L-H) loading sequence considers first the application of a tangential load of amplitude Q_2 followed by the one of amplitude Q_1. In this case, the first amplitude block Q_2 is prescribed over n_1' cycles and this number of cycles is chosen so that the damage generated by the low amplitude block is equal to the one generated in the high amplitude block of the H-L loading sequence. Damage assessments are carried out by means of Miner's rule. Similarly, the number of cycles n_2' is determined by equating the damage of the high amplitude block in the L-H loading sequence with the one present in the low amplitude block of the H-L loading sequence. It means that the damage in the first load block for both loading sequences (H-L and L-H) is determined as follows:

$$d_1 = \frac{n_1}{N_1} = \frac{n_1'}{N_2} \tag{3.1}$$

where N_1 and N_2 are the experimentally observed lives for the high and low loading blocks respectively. These lives are obtained by evaluating a test of a single loading block until the failure.

3.2.3 Measuring the coefficient of friction - COF

Two tests were carried out in order to obtain the coefficient of friction under fretting conditions for the aluminum alloy 7075-T651. Figure 3.22 illustrates the procedure to obtain the mean coefficient of friction, f_m, which consists of a composition of the friction coefficients in the slip and the stick zones. The methodology to obtain f_m consists initially of performing a pure fretting test in displacement control, that is, applying the normal load P (constant throughout the test) and then the tangential displacement amplitude δ_a is prescribed during the test and is increased gradually (steps of 2.5 μm at every 200 cycles) until the tangential force read on its load-cell is equal to the desired tangential load. After, the test is maintained for approximately 10,000 cycles so that the fretting scar is properly developed. The second part of the test requires a monotonic increase of the tangential load until full sliding is achieved and shear load at this moment is recorded. This maximum Q/P ratio is the mean coefficient of friction, f_m. Note that f_m is an average of the slip and stick zone friction coefficients found on the contact surface.

To evaluate the tractions and subsurface stress field in fretting fatigue it is necessary to use the coefficient of friction for the slip zones, f_s. Hills and Nowell

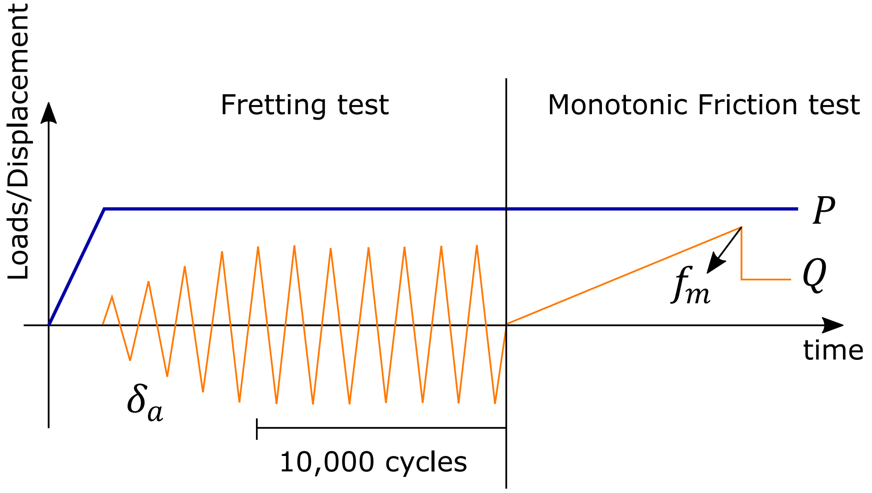
Loads/Displacement
Fretting test
Monotonic Friction test
P
Q
f_m
time
δ_a
10,000 cycles

Figure 3.22: Test methodology to determine the mean coefficient of friction.

and after Araújo and Nowell [82, 7] proposed an analytical solution to obtain the f_s once the f_m is known. It can be calculated as:

$$f_m = f_s + \left[\frac{4Q}{\pi P}\left(\frac{\pi}{2} - \cot\theta_s - \theta_s\right) - \frac{\pi}{2}\left(f_s\phi_s - \frac{Q}{P}\tan\phi_s\right)\right] \tag{3.2}$$

wehere

$$\theta_s = \sin^{-1}\sqrt{\frac{Q}{f_s P}} \tag{3.3}$$

and

$$\phi_s = \cos^{-1}\sqrt{\frac{Q}{f_s P}} \tag{3.4}$$

Following the experimental methodology described above, two tests were carried out to determine the coefficient of friction. Table 3.6 summarizes the results.

Table 3.6: Coefficients of friction for the Al 7075-T651 alloy under fretting conditions with a constant normal load.

Test	**Fretting test**			**Monotonic test**	
	P [N/mm]	Q_a **[N/mm]**	**Q/P**	f_m	f_s
COF1	483	192	0.4	0.56	0.91
COF2	483	192	0.4	0.54	0.79
Mean				**0.55**	**0.85**

3.2.4 Experiments observations and results

The first step in carrying out tests with variable-amplitude loading blocks is to define what the loading configurations of these blocks will be. Since the number of cycles applied to the first block is defined based on the damage generated in the material, it becomes necessary to identify the life to failure for each loading configuration. In this work, a sequence of loadings of the H-L and L-H type was chosen. However, before one conducts the tests with the H-L or L-H sequence of blocks, it is necessary to perform tests just with the high amplitude shear load configuration and later with low one. This will allow us to obtain the N_1 and N_2 lives required to compute the fagitue damage performed by each loading block individually.

Table 3.7: Loading configuration of the blocks High and Low.

Load config.	**Q [N/mm]**	**P [N/mm]**	**Q/P**	$\mathbf{R}_p$ **[mm]**	**a [mm]**	p_0 **[MPa]**	**B [MPa]**
High	210	300	0.7	70	0.837	228	70
Low	120	300	0.4	70	0.837	228	70

Table 3.8: Fretting fatigue lives of the loading block individually (High and Low blocks).

Test	**Load config.**	N_f **[cycles}**	**Mean**
FF1	High	122,037	
FF2	High	146,178	143,281
FF3	High	168,048	
FF4	Low	345,313	348,102
FF5	Low	350,891	

Table 3.7 shows the loading configuration of each block and in Table 3.8 can be seen the experimentally observed lives. In both loading blocks, High and Low,

a loading ratio R= -1 for the tangential and bulk loads was considered. The normal load P was held constant during all tests. As can be seen, the difference between the High and Low blocks is only in the amplitude of the tangential load used. The tangential load of the High block is 75% higher than that of the Low block, this difference is large enough so that the average life of the High block is 41% lower than the average life of the Low block.

Three tests were performed for the High block and two tests for the Low block, both until the material failed. With these tests, it was possible to define the lives N_1 and N_2 (averages of the observed lives of the High and Low blocks respectively). Now it is possible to design and to carry out our set of fretting fatigue tests under variable amplitude block loading. Table 3.9 shows the loading configuration of the tests H-L and L-H. The results of tests performed with loading sequences H-L and L-H are presented in Tables 3.10 and 3.11 respectively.

Table 3.9: Loading configuration of the tests H-L and L-H.

Load config.	Q_1 **[N/mm]**	Q_2 **[N/mm]**	**P [N/mm]**	**B [MPa]**
H-L	210	120	300	70
L-H	120	210	300	70

Table 3.10: Fretting fatigue tests under H-L loading sequence.

Test.	**Load seq.**	$\mathbf{d_1}$	$\mathbf{n_1}$	$\mathbf{n_2}$	$\mathbf{N_f}$
FF6	H-L	0.75	107,461	22,553	**130,014**
FF7	H-L	0.75	107,461	44,756	**152,217**
FF8	H-L	0.5	71,641	96,408	**168,048**
FF9	H-L	0.5	71,641	125,173	**196,813**
FF10	H-L	0.5	71,641	134,240	**205,880**
FF11	H-L	0.4	57,312	201,203	**258,515**
FF12	H-L	0.3	42,984	255,259	**298,243**
FF13	H-L	0.25	35,820	332,611	**368,431**
FF14	H-L	0.25	35,820	304,180	**340,000**
FF15	H-L	0.25	35,820	308,945	**344,765**

Figure 3.23 presents the experimental results as a function of the material damage generated by the first load block. Figure 3.23(a) shows the results for the H-L loading sequence. The solid black line in this figure represents the life estimated by Miner's damage accumulation rule, while the blue squares are the experimental results. Likewise, in Figure 3.23(b), the results for the L-H loading sequence are shown. In this case, the values estimated by Miner's

Table 3.11: Fretting fatigue tests under L-H loading sequence.

Test.	**Load seq.**	$\mathbf{d}_1$	**n'**$_1$	**n'**$_2$	$\mathbf{N}_f$
FF16	L-H	0.75	261,077	57,889	**318,965**
FF17	L-H	0.75	261,077	62,910	**323,986**
FF18	L-H	0.5	174,051	87,025	**261,076**
FF19	L-H	0.5	174,051	79,038	**253,089**
FF20	L-H	0.5	174,051	67,142	**241,193**
FF21	L-H	0.35	121,836	92,175	**214,011**
FF22	L-H	0.25	87,026	97,975	**185,000**
FF23	L-H	0.25	87,026	175,895	**262,920**
FF24	L-H	0.25	87,026	168,501	**255,526**
FF25	L-H	0.25	87,026	150,370	**237,395**
FF26	L-H	0.15	52,215	145,048	**197,263**

rule are represented by the solid red line and the experimental data by yellow triangles. Note that the behavior pattern differs when comparing the two loading sequences. The L-H sequence is closer to the estimates using Miner's rule.

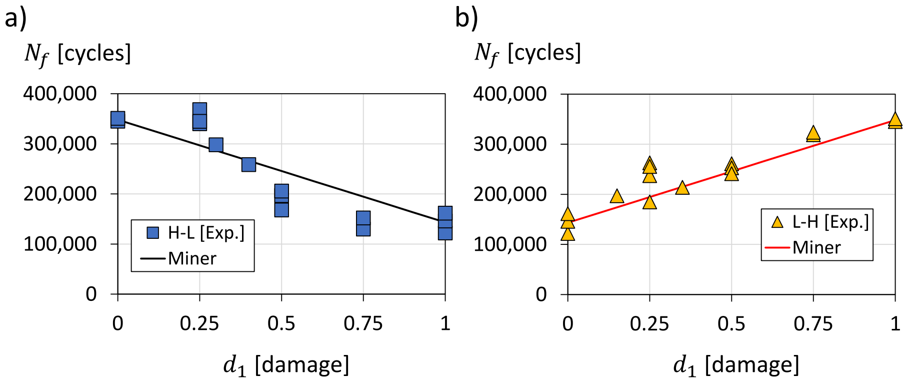

Figure 3.23: Experimental fretting fatigue lives of the H-L (a) and L-H (b) loading blocks.

Figure 3.23(a) shows that if the damage generated in the first loading block (High block) is d_1<0.3, Miner's rule is more conservative. Nonetheless, when applying a number of cycles in the High block large enough to generate initial damage greater than 0.3 a reduction in the actual total life is observed when compared to that estimated by Miner´s rule. On the other hand, the experimental results of the L-H loading sequence, Figure 3.23(b), show that for this configuration, the sensitivity to the loading sequence effect is much lower than in the H-L because the results are closer to those predicted by the linear damage model.

These still limited range of experimental data for fretting fatigue under varying block loading seem to indicate that the loading sequence has an effect on the accumulated fatigue damage. Although this effect exists (especially for H-L sequences), it does not mean that Miner's rule can not be applied for life assessment. Figure 3.24 presents all experimental results (H-L and L-H blocks) compared with the estimated life using Miner's rule. As can be seen, the data are all within a scatter band of factor 1.5. This means that the margin of error is between 50% and -33%.

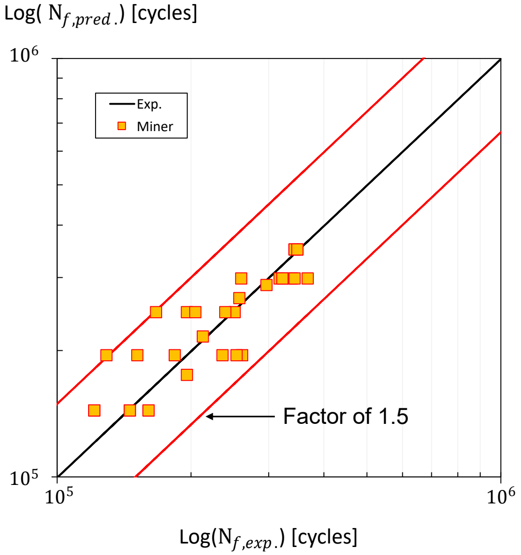

Figure 3.24: Estimated and observed fretting fatigue lives under variable loading conditions.

Fractography

Figure 3.25 (a) and (b) show the fretting scars after failure of specimens FF2 [H] (Table 3.8) and FF19 [L-H] (Table 3.11) respectively . Note that the fretting wear scar has a width of approximately 1.64-1.70mm, while the theoretical contact size 2a=1.674mm, and the crack that led to failure initiated at the edge of the contact. In the FF19 [L-H] test, there is a load change, and it may have caused a more significant slip initially, which stabilized soon afterward. This behavior explains the brighter aspect, as some of the debris at the edge of the contact may have been dragged along with this slip during the load change.

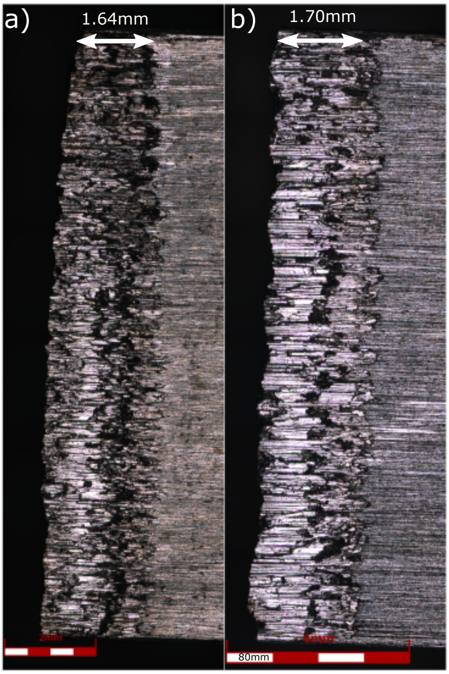

Figure 3.25: Fretting scar of the fretting fatigue specimens FF2 [H] (a) and FF19 [L-H] (b).

Figure 3.26 indicates the fracture surface of the same tests as Figure 3.25. Figure 3.26(a) is the specimen FF2 and Figure 3.26(b) the specimen FF19. Note that, in both tests, multiple cracks nucleated at the contact surface. These microcracks become a single dominant macrocrack that propagates along the specimen until failure. Figure 3.26 indicates that the fracture surface consists of two distinguished regions: one for cracks initiation site induced at contact interface followed by crack propagation zone, and the other one for a rupture region due to overloading.

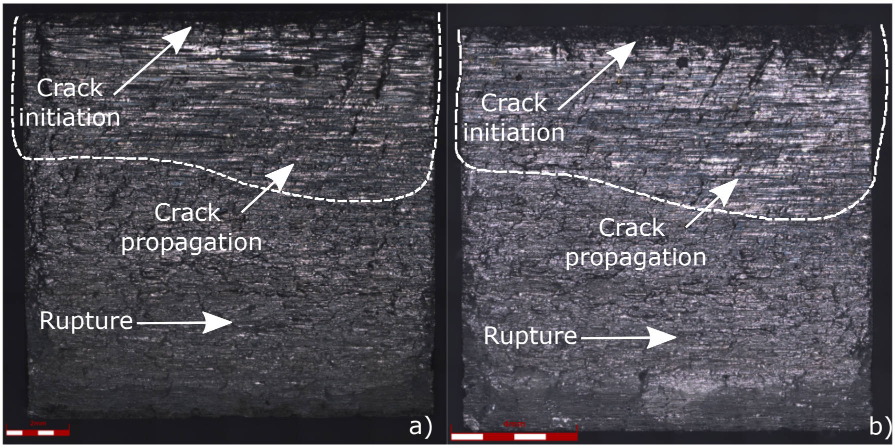

Figure 3.26: The fracture surface of the fretting fatigue specimens FF2 (a) and FF19 (b).

Crack propagation trajectory

Figure 3.27 shows a three-dimensional image of the fracture surface of specimen FF19. This three-dimensional image was used to obtain the crack trajectory and consequently the initiation angle (considering a length of $2L = 39\mu$m). As crack path and initiation angle can vary significantly along the fractured surface, five individual crack paths were measured along the fractured surface following the dashed red line depicted in Figure 3.28. The crack path and initiation angle for each test is defined as the average of them.

Figure 3.29 shows the crack path of tests FF2, FF5, FF8, and FF19. These trajectories were obtained using the average of different trajectories on the fracture face, as previously described. As can be seen, in all tests the initial crack propagates under mixed-mode, and after that, the crack propagation is governed by axial stress perpendicular to the contact interface. The initial crack angle was measured for the four tests and is shown in Table 3.12.

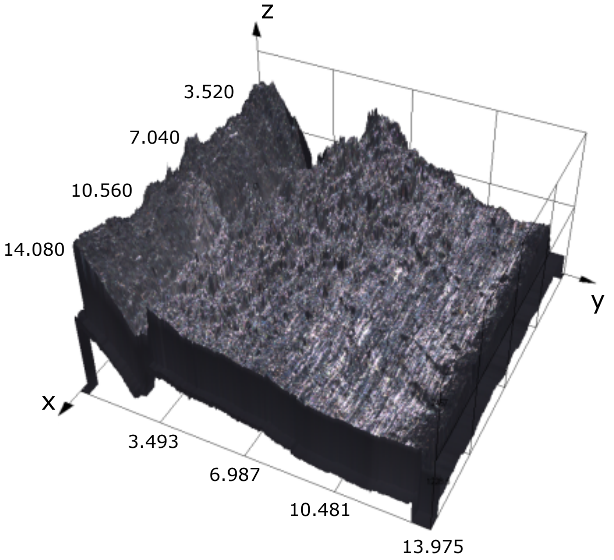

Figure 3.27: The three-dimensional fracture surface of the fretting fatigue specimen FF19 (dimensions in mm).

Table 3.12: Initial crack angle observed for the crack size of $2L$.

Test	**Load seq.**	**Crack angle [°]**
FF2	High	11
FF5	Low	2
FF8	H-L	17
FF19	L-H	14
Mean		11

3.3 Fretting fatigue data available in the literature

This section presents experimental data available in the literature for three different aluminum alloys. Both basic properties of these materials and fretting fatigue test results are provided. Some of these data were used in other chapters to implement numerical models and even to validate the proposed methods.

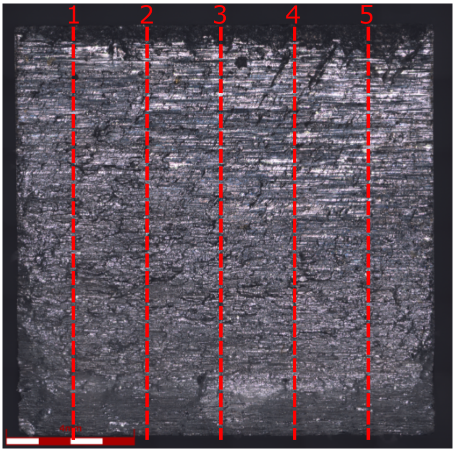

Figure 3.28: Methodology of fretting crack path and initiation angle measurement.

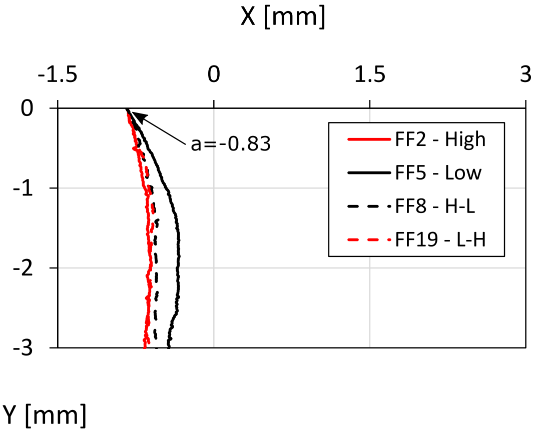

Figure 3.29: Crack propagation path of fretting fatigue specimens FF2, FF5, FF8, and FF19.

3.3.1 Al 7075-T651

Tha basic material monotonic and cyclic properties of aluminum alloy 7075-T651 are provided in Table 3.13. According to [21], the stress intensity factor threshold range, ΔK_{th}, for this aluminium alloy is 3 MPa$\sqrt{m}$ and in [20] the fully reversed fatigue limit range, $\Delta\sigma_{-1}$ (1×10^6 cylces), is 350 MPa, which yields a critical distance parameter $L = 23.4$ μm. The friction coefficient between the contacting surfaces for a cylinder on plane contact configuration may vary from 0.7 to 0.85, according to the tests carried out by the University of Seville fretting fatigue research team [101, 23]. The local wear coefficient κ_w is 1.25×10^{-8} mm^2/N according to [88].

Table 3.13: Mechanical properties of Al7075-T651 [167].

Monotonic properties		
Young's modulus	E	71 GPa
Poisson's modulus	ν	0.33
Yield strength	S_y	503 MPa
Ultimate tensile strength	S_{ut}	572 MPa
Cyclic properties		
Fatigue strength coeff.	σ'_f	1231 MPa
Fatigue ductility coeff.	ε'_f	0.263
Fatigue strength exp.	b	-0.122
Fatigue ductility exp.	c	-0.806

3.3.2 Al 2024-T3

In this thesis, the experimental data of the fretting fatigue tests obtained by Talemi et al. [84] were used to validate the method of life assessment including wear and crack propagation. The material used was aluminum 2024-T3, a tempered aerospace aluminum with good fatigue properties. All the test specimens were produced from a single sheet of aluminum 2024-T3. The mechanical properties from the specification sheet are reported in Table 3.14. Table 3.15 shows the loading conditions in each fretting fatigue test and respective life observed, where B represents the bulk fatigue load, R$_p$ is the pad radius, P is the normal force, Q$_{max}$ is the tangential load and N_f is the experimental total life to the complete failure of the specimens.

The S-N curve was provided by Newman et al. [120] and was obtained considering uniaxial tests for different load ratios as shown in Figure 3.30. To compute the wear using Archard's equation, it is crucial to determine the local wear coefficient k. Ashwin et al. [13] performed wear tests on 2024-T351 aluminum alloy specimens. The results indicate that the wear rate obtained was in the order of $10^{-7} g/Nm$ for the tested parameter conditions. Conservatively, in this work, the lowest value for the wear coefficient was used. According to Eq. 2.71, it is enough to divide the wear rate by the density of the material (7,28

Table 3.14: Mechanical properties of Al2024-T3 [84].

Monotonic properties		
Young's modulus	E	72.1 GPa
Poisson's modulus	ν	0.33
Yield strength	S_y	383 MPa
Ultimate tensile strength	S_{ut}	506 MPa
Fracture toughness	K_{Ic}	2083 MPa$\sqrt{mm}$
Coefficient of friction	f	0.65
Cyclic properties		
Threshold stress intensity factor	ΔK_{th}	100 MPa$\sqrt{mm}$
Uniaxial plain fatigue limit	$\Delta\sigma_{-1}$	263 MPa
Critical distance	$L/2$	23μm

Table 3.15: Test conditions of fretting fatigue experiments [84].

Test no.	**B (MPa)**	**R$_p$ (mm)**	**P (N/mm)**	**Q$_{max}$ (N/mm)**	**Q/P**	p_0 **(MPa)**	N_f **(cylces)**
FF1	100	50	135.8	38.8	0.29	187	1,407,257
FF2	115	50	135.8	46.6	0.34	187	1,105,245
FF3	135	50	135.8	55.9	0.41	187	358,082
FF4	135	50	135.8	48.9	0.36	187	419,919
FF5	160	50	135.8	48.4	0.36	187	245,690
FF6	190	50	135.8	82.5	0.61	187	141,890
FF7	205	50	135.8	80.5	0.60	187	114,645
FF8	220	50	135.8	66.8	0.49	187	99,607
FF9	220	50	135.8	79.5	0.59	187	86,647

g/cm^3) to obtain the local wear coefficient. Thus, the local wear coefficient was defined as $k_w = 5.81 \times 10^{-8} MPa^{-1}$.

3.3.3 Al 7050-T7451

In order to test the accuracy of the proposed method to compute the crack nucleation angle, the experimental data provided by Almeida et al. [2] was used in this thesis. The material considered in [2] was an aluminum 7050-T7451. The average size of the small grains of this material is 8 μm. Flat dog-bone specimens and cylindrical pads both made of AA7050- T7451 were used in the fretting tests. The specimens have a square cross-section of 13×13 mm. Two sizes of cylindrical pads were considered in the tests: a smaller one with a radius of 30 mm and a larger one with a radius of 70 mm.

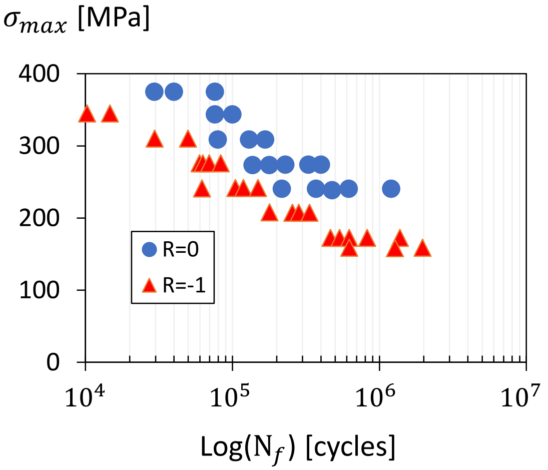

Figure 3.30: Uniaxial fatigue data for the Al 2024-T351 [120].

Table 3.16 lists the mechanical properties of the aluminum alloy considered in this thesis. Table 3.17 reports the loading conditions in each fretting fatigue test, where σ_m represents the mean bulk load, R_p the pad radius, P the normal contact force, Q_a the tangential load amplitude and p_0 the contact peak pressure. The loading history considered in all the tests is depicted in Figure 3.31. Firstly, a mean bulk, B, is prescribed on the specimen. Secondly, a constant normal load, P, presses the cylindrical pad against the specimen. Finally, a fully reversed tangential load with amplitude, Q_a, is prescribed on the pad ensuring partial slip conditions. Notice that the mean bulk stress σ_m is given by the ratio of the mean bulk stress, B, to the cross-section area of the specimen.

Table 3.16: Monotonic and cyclic properties of 7050-T7451 aluminum alloy.

Young's Modulus, E	71.7 GPa
Poisson's ration, ν	0.33 MPa
Yield stress, S_y	469 MPa
Ultimate tensile strength, S_{ut}	524 MPa
Fatigue limit range, $\Delta\sigma_{-1}$	292 MPa
Threshold stress intensity factor range, ΔK_{th}	5.5 MPa$\sqrt{m}$
Friction coefficient, f	0.54
Critical distance, L	113 μm

To compute wear using Archard's equation, it is crucial to determine the local wear coefficient k_w. However, no data were found in the literature for

Table 3.17: Loading and geometry configurations of fretting experiments.

Load config.	$\mathbf{Q}_a$ **(N/mm)**	**P (N/mm)**	$\mathbf{Q}_a$**/P**	$\mathbf{R}_p$ **(mm)**	**a (mm)**	p_0 **(MPa)**	σ_m **(MPa)**
C1	240	800	0.3	70	1.34	380	0
C2	320	800	0.4	70	1.34	380	0
C3	400	800	0.5	70	1.34	380	0
C4	136.4	341	0.4	30	0.57	380	0
C5	136.4	341	0.4	30	0.57	380	25
C6	136.4	341	0.4	30	0.57	380	50
C7	320	800	0.4	70	1.34	380	25
C8	320	800	0.4	70	1.34	380	50

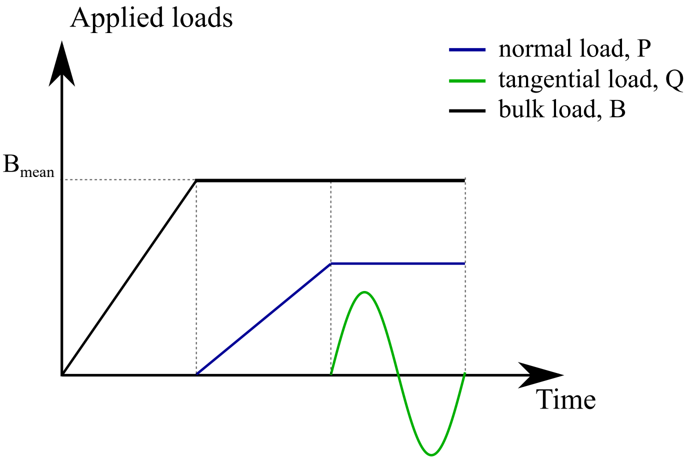

Figure 3.31: Schematic of tests loading history.

the material investigated. To overcome such an issue, the wear coefficient of similar material (Al 7075-T651 [133]) has been considered in the analyses of this material: $k_w = 1.25 \times 10^{-8}$ MPa^{-1}. The S-N curve considered in this work was obtained by [90] from fatigue tests conducted on 7050-T7451 aluminum alloy flat dog-bone specimens subjected to fully reversed push and pull loading conditions, as shown in Figure 3.32. Table 3.18 presents the measured experimental crack initiation angles for all the tests reported in [2].

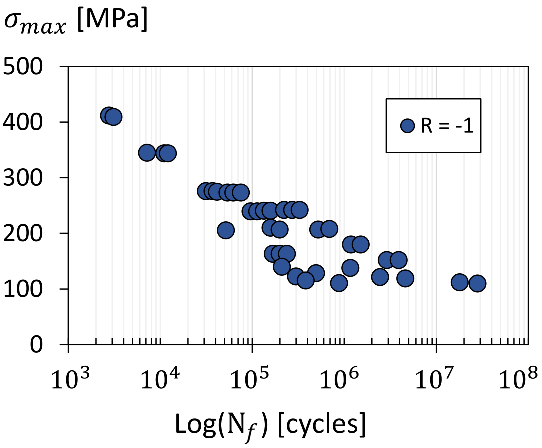

Figure 3.32: Uniaxial fatigue data of Al 7050-T7451 [90].

Table 3.18: Crack orientation measured for all tests.

Load Config.	**Test**	**Exp. (°)**	**Average (°)**
C1	T1	12.8	21.4 +/- °12.2
	T2	30	
C2	T1	28	29.5 +/- °6.4
	T2	36.6	
	T3	24	
C3	T1	25.7	31.4 +/- °8.0
	T2	37	
C4	T1	29.7	25.9 +/- °5.4
	T2	22	
C5	T1	31.3	31.5 +/- °0.3
	T2	31.7	
C6	T1	36.3	30.4 +/- °8.4
	T2	24.4	
C7	T1	40.7	32.4 +/- °13.6
	T2	16.7	
	T3	39.7	
C8	T1	46.5	37.2 +/- °13.2
	T2	27.9	

Chapter 4

Effects of fretting wear process on fatigue crack propagation and life assessment

"This chapter proposes a new methodology for fretting fatigue life assessment. It uses a combination of multiaxial fatigue criteria, the theory of critical distances and a node-displacement wear algorithm to account for the initiation life under fretting. A new method is also introduced to predict the crack propagation path under nonproportional loading conditions"

This chapter was previously published as:
PINTO, André Luis; ARAÚJO, José Alexander; TALEMI, R. Effects of fretting wear process on fatigue crack propagation and life assessment. Tribology International, 2021, 156: 106787.
and
PINTO, A. L.; TALEMI, R.; ARAÚJO, J. A. Fretting fatigue total life assessment including wear and a varying critical distance. International Journal of Fatigue, 2022, 156: 106589.

With respect to the original publication, a few symbols are changed to comply with the general nomenclature and certain paragraphs are modified slightly to avoid redundancy.

4.1 Overview

The small relative movement which occurs between the contact surfaces of mechanical assemblies subjected to vibration can give rise to two different mechanical problems, fretting fatigue and fretting wear [171, 170, 168]. Fretting fatigue presents a small relative slip between the contact faces sufficient for one region of the contact zone to be stuck and the other part to slide (partial slip regime). In this type of fretting the wear effects are small and the initiation and further development of cracks is the dominant phenomenon. On the other hand, in case the amount of slip increases so that all corresponding points within the contact surfaces slide one with respect to the other, a gross slip regime takes place. In such a regime the crack initiation problem is limited due the high level of material removal caused by the wear in the contact region. Here fretting wear is the dominant mechanical problem [22, 60].

Given the high-stress gradient in the contact problem, it is common to use the theory of critical distance (TCD) in the solution of fretting problems by taking advantage of the “notch analogy” approach [128]. As the values of the critical distances under fatigue and static loading are usually different, it can be assumed that the critical distance at the medium-cycle fatigue regime depends on the number of cycles to failure. The majority of works carried out on fretting fatigue, which applied the TCD, did not take into account its dependence on life [27, 175, 166, 43]. Recently, some research has been conducted using TCD as a function of life [9, 93], however, these researchers do not include surface wear or crack propagation. Although Araújo et al. [5] have considered the effects of wear and used a critical distance depending on life in their life estimation approach, they did not separate initiation and propagation lives, and the effect of wear was considered to compute total life based on a critical plane criterion.

In this chapter, a new approach will be presented in which the total life is separated into the nucleation and crack propagation phases. In this new approach, wear effects are computed only up to the crack nucleation life. This new approach will be applied in two different ways, the first considering the critical distance as a fixed value, and the second where the critical distance is considered as a function of life. Fretting wear effects are taken into account using Archard’s law. To compute the initiation life the Smith-Whatson-Topper (SWT) multiaxial fatigue parameter is combined with a linear damage accumulation law (Miner’s law) and the theory of critical distance (TCD, using the point method). The eXtended Finite Element Method (XFEM) is then considered to model crack propagation. Propagation lifetime is obtained by employing a new method introduced to predict crack path under non-proportional loading conditions. Experimental results obtained by Talemi et al. [84], presented in Section 3.3.2, are used to validate the numerical methodology proposed. In the next sections, all the details are provided.

4.2 Methodologies to fretting fatigue life assessment

This thesis presents three methodologies for fretting fatigue life assessment (Methods 1, 2, and 3) which will be applied in two ways, one considering fixed L and the other considering L_m as a function of life. Figure 4.1 presents a flow chart for each of these methods. For all of them, the crack nucleation point was calculated based on the location of maximum dissipated energy at the contact interface during one full cyclic loading. Giner et al. [69] have reported that different crack initiation angles do not strongly affect the orientation after a few crack increments. Based on these facts the crack initiation angle was defined based on experimental observation. The concept of cumulative dissipated energy, E_d, was introduced by Monhrbacher et al. [111]. The total dissipated energy after one cycle can be written as:

$$E_d = \Sigma_{i=1}^{n} \tau_i \times \delta_i, \tag{4.1}$$

where τ_i is the frictional shear traction and δ_i is the local slip amplitude.

In Method 1, easier to implement, the stress/strain history in a single material point is used to estimate life. The horizontal position of such a point is defined as the one where E_d is maximum, while the vertical position is located at a critical distance from the contact surface, $L/2$. Under fatigue limit conditions and considering the Point Method [9, 131], the critical distance, L, is calculated by Eq. 2.46. At the medium-high cycle fatigue regime, the critical distance depends on the number of cycles to failure, N_f. Usually, a power law relationship [155] is used to relate L_M and N_f. The critical distance, L_M, is calculated by Eq. 2.48.

In method 2, the life is divided between crack nucleation, N_i, and crack propagation, N_p. For the calculation of N_i, an approach similar to the first method is used. However, in this case, the multiaxial fatigue parameter used is calibrated for crack nucleation life and not for total failure. The crack is modeled using the XFEM method. The propagation life, N_p, is obtained using Paris' law.

Method 3, also presented in Figure 4.1, is the most robust among the methods used in this work. In this method, in addition to the separation between crack nucleation and propagation life (method 2), the effects of surface wear are computed in the crack nucleation phase. The crack initiation point is defined in the first cycle of the wear simulation, and this point is the one where E_d is maximum.

4.3 Numerical aspects

Three methodologies were presented for fretting fatigue total life assessment. One of the methodologies includes surface wear and crack propagation, however, the others are simpler (without surface wear), which may or not include crack propagation. Therefore, the next subsections (4.3.1 to 4.3.5) will be dedicated to detail the numerical aspects.

4.3.1 Critical distance application

The critical distance as a function of life was implemented as shown in Figure 4.2. To obtain the number of cycles to failure, an initial value of life ($N = N_0$) is guessed to calculate the critical distance that is determined according to Eq. 2.48. The history of stress/strain is then evaluated at a point that is at this critical distance from the surface, L_M, and the fatigue damage accumulation is maximum, Figure 4.2(a). The number of cycles to failure, $N_{f,e}$, is calculated using the multiaxial fatigue parameter. If the calculated $N_{f,e}$ is different from the trial value N, a new interaction is started considering $N = N_{f,e}$. This recursive procedure is repeated until convergence between the calculated $N_{f,e}$ and the trial value N, Figure 4.2(b). In Methods 1 and 2 this process is done only once, however, in Method 3 is repeated every time the surface is updated due to the wear process.

4.3.2 Multiaxial fatigue parameter calibration

In this work, two methodologies separate the life, N_f, into nucleation and crack propagation lives. When wear is neglected, the multiaxial parameter is calibrated using an S-N curve obtained for the total failure of the specimens. In this case, the calculated life or damage will always refer to total life, N_f. However, should wear be considered, the fatigue damage is computed only up to the crack nucleation life, N_i. Therefore, the multiaxial parameter must be calibrated with a crack nucleation S-N curve.

To obtain the S-N curve for crack nucleation, it is necessary to discount the crack propagation life, N_p, for each fatigue test data of the S-N curve for failure. Figure 4.3 demonstrates how this procedure is conducted. Note that it is

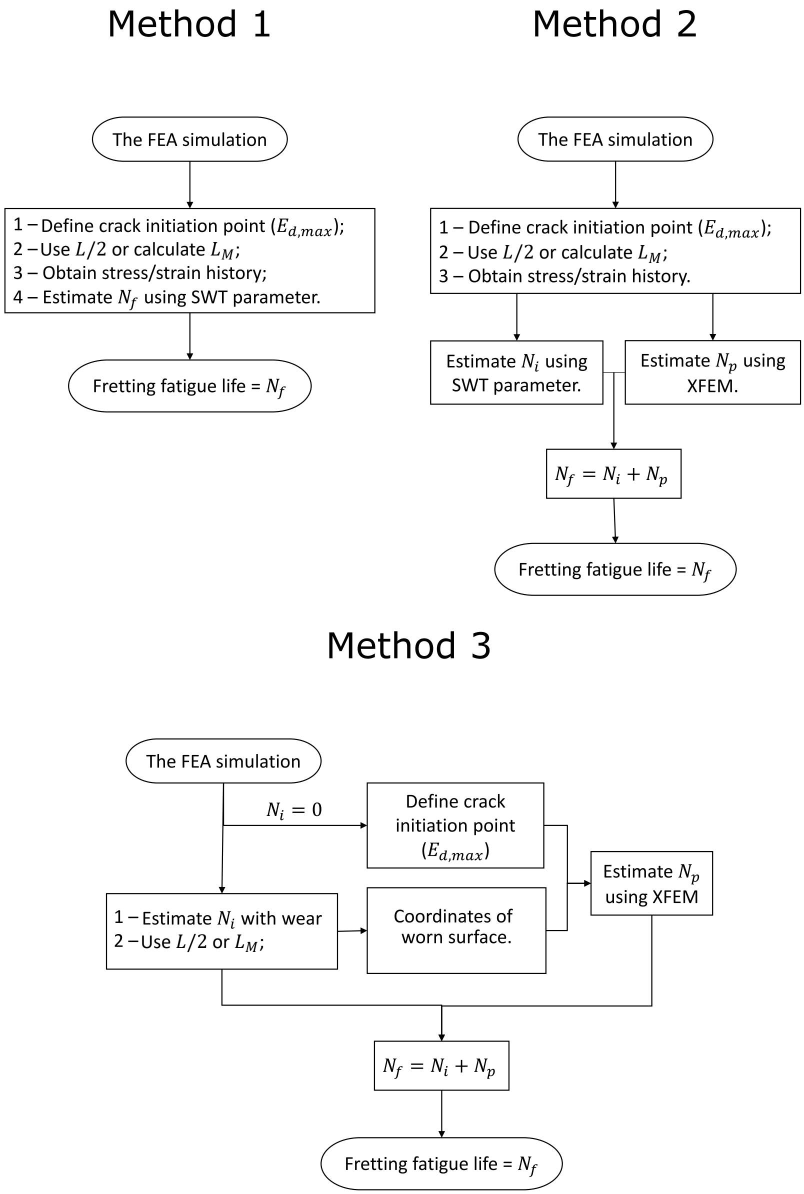
Method 1
The FEA simulation
1 – Define crack initiation point ($E_{d,max}$);
2 – Use $L/2$ or calculate L_M;
3 – Obtain stress/strain history;
4 – Estimate N_f using SWT parameter.
Fretting fatigue life = N_f
Method 2
The FEA simulation
1 – Define crack initiation point ($E_{d,max}$);
2 – Use $L/2$ or calculate L_M;
3 – Obtain stress/strain history.
Estimate N_i using SWT parameter.
Estimate N_p using XFEM.
$N_f = N_i + N_p$
Fretting fatigue life = N_f
Method 3
The FEA simulation
$N_i = 0$
Define crack initiation point ($E_{d,max}$)
1 – Estimate N_i with wear
2 – Use $L/2$ or L_M;
Coordinates of worn surface.
Estimate N_p using XFEM
$N_f = N_i + N_p$
Fretting fatigue life = N_f

Figure 4.1: Flowchart of the third method for fretting fatigue life assessment.

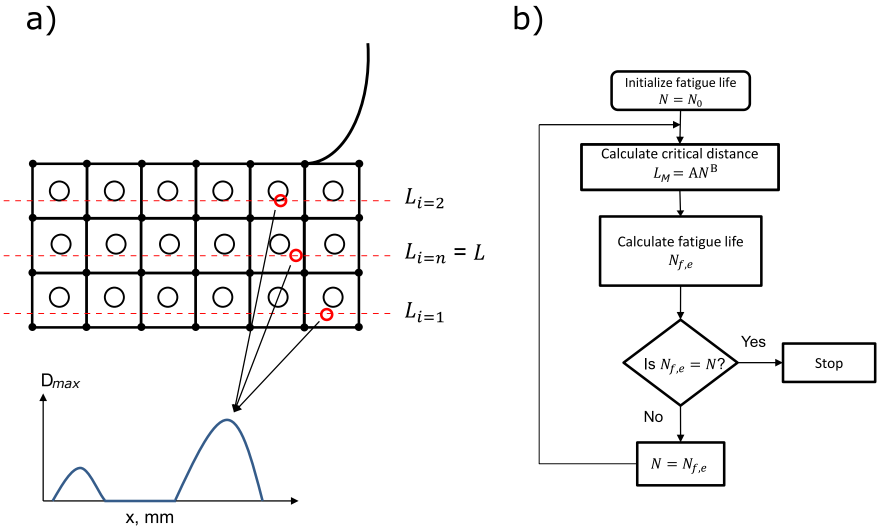
a)
b)
$L_{i=2}$
$L_{i=n}$ = L
$L_{i=1}$
D$_{max}$
x, mm
Initialize fatigue life
$N = N_0$
Calculate critical distance
$L_M = AN^B$
Calculate fatigue life
$N_{f,e}$
Is $N_{f,e} = N$?
Yes
Stop
No
$N = N_{f,e}$

Figure 4.2: Procedure to estimate the critical distance L_M: (a) definition of the critical distance L_M and (b) flowchart of the algorithm for fatigue life calculation.

necessary to define an initial crack size, a_i. According to [73], the 2024-T351 aluminum alloy has a grain size of 50 μm. Therefore, in this work, the initial crack size was used as 100 μm, which is two times the grain size. The S-N curve used in this work was obtained by conducting fatigue tests on flat dog-bone specimens made of the 2024-T3 aluminum alloy under R = 0 and R = -1 loading, and the specimens were electro-polished. In this way, N_p could be obtained as follows:

$$N_p = \sum \Delta N = \sum \frac{\Delta a}{C \Delta K^m}, \tag{4.2}$$

where, C and m are constants of material and Δa is the crack incremental size (100 μm). ΔK was obtained according to the equation below:

$$\Delta K = K_{max} = \sigma_{max} F \sqrt{\pi a}, \tag{4.3}$$

σ_{max} is maximum stress applied to the specimen and S is the shape factor that for this geometry is obtained according to Eq (4.4) [48], where, a is the crack size and b is the width of the specimen.

$$F = 0.265\left(1-\frac{a}{b}\right)^4 + \left(\frac{0.857+0.265\frac{a}{b}}{\left(1-\frac{a}{b}\right)^{\frac{3}{2}}}\right). \tag{4.4}$$

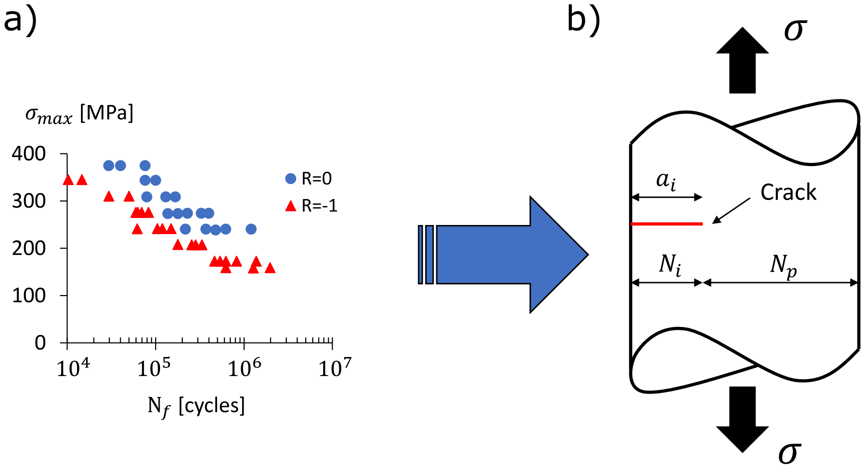

Figure 4.3: Process of calibration of uniaxial fatigue data (Al 2024-T351 [120]) for crack nucleation life estimation.

Two multiaxial fatigue models were used for life assessment, SWT (Smith-Watson-Topper) and FS (Fatemi-Socie), defineds in Sections 2.2.2 and 2.2.3 respectively. To calibrate these fatigue models data provided by Newman et al. were used [120]. The S-N curve was obtained considering uniaxial tests for different load ratios as shown in Figure 4.3(a). The parameters SWT and FS were calibrated for total life, N_f, and crack nucleation life, N_i, see Figures 4.4 and 4.5. To calibrate the parameters for total life, we have just used the same data obtained in the literature, as they are for total fracture. However, for crack nucleation life, it is necessary to subtract the crack propagation life from the data, as in Figure 4.3(b). Therefore, considering an initial crack of $100\mu m$, the propagation life N_p was estimated for all data using Paris' law. In this way, it was enough to subtract the propagation from the total life. Then calibrate the multiaxial parameter for crack nucleation.

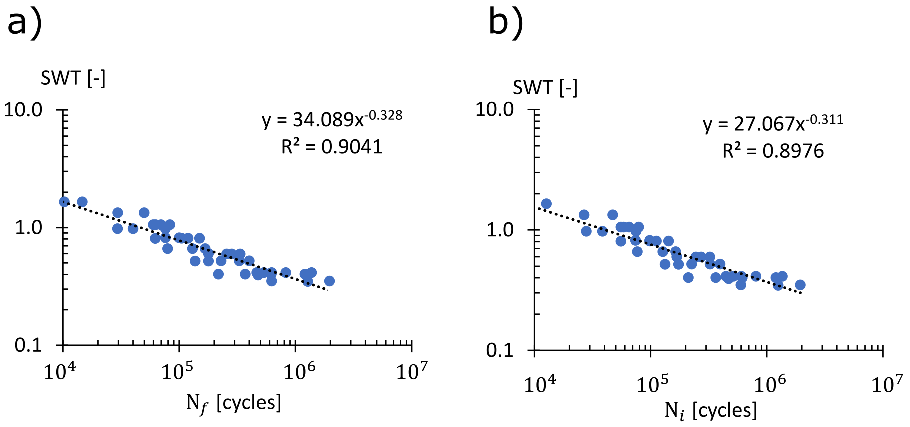

Figure 4.4: Uniaxial fatigue data for the Al 2024-T3 expressed in terms of the SWT parameter: total failure (a) and nucleation life (b).

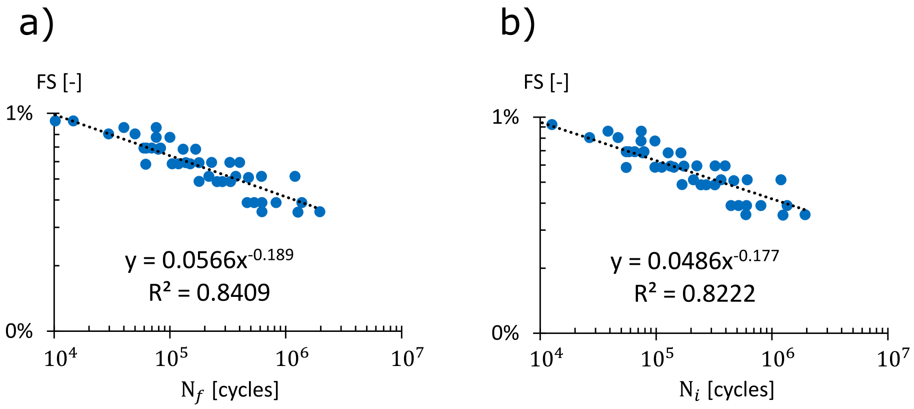

Figure 4.5: Uniaxial fatigue data for the Al 2024-T3 expressed in terms of the FS parameter: total failure (a) and nucleation life (b).

4.3.3 Wear modeling and damage accumulation

The strategy for the wear modeling and damage accumulation is the same used in [26, 133] and can be accessed in Section 2.7. However, this research work proposes a different technique for the contact surface update. Instead of using the remesh technique like in previous works, the moving node technique was used, where the position of the nodes on the contact surface is changed in each step using the same mesh in all simulations.

In this setting, Figure 4.6 displays a flowchart illustrating the FE-based wear model coupled with the moving node technique. Herein, the main Python script manages all the process which consists of the simulation of each fretting cycle i followed by the contact surfaces updating, where contact nodes are vertically moved according to Eq. (2.75). As can be seen in Figure 4.6, instead of creating a new CAE file and consequently a new mesh, it is used the input file to run the simulation. This way there is no need to create another mesh.

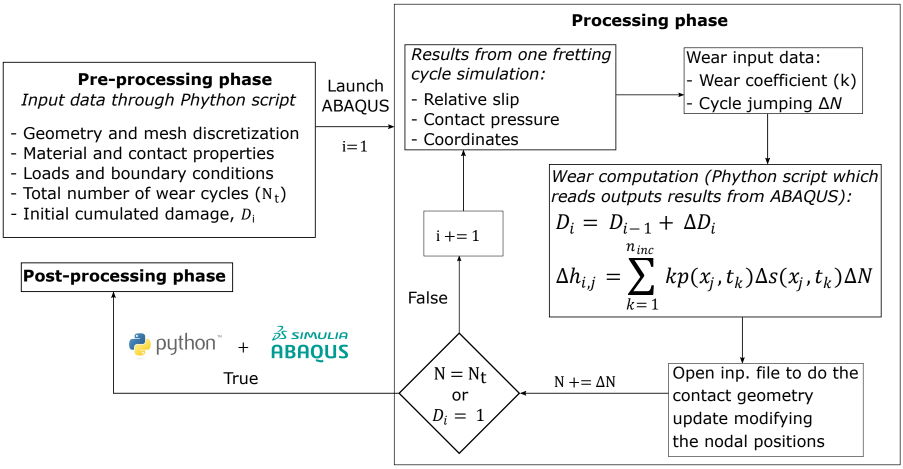
Processing phase
Pre-processing phase
Input data through Phython script
- Geometry and mesh discretization
- Material and contact properties
- Loads and boundary conditions
- Total number of wear cycles (N_t)
- Initial cumulated damage, D_i
Launch ABAQUS
i=1
Results from one fretting cycle simulation:
- Relative slip
- Contact pressure
- Coordinates
Wear input data:
- Wear coefficient (k)
- Cycle jumping ΔN
Wear computation (Phython script which reads outputs results from ABAQUS):
$D_i = D_{i-1} + \Delta D_i$
$\Delta h_{i,j} = \sum_{k=1}^{n_{inc}} kp(x_j,t_k)\Delta s(x_j,t_k)\Delta N$
i += 1
False
Post-processing phase
python + SIMULIA ABAQUS
True
N = Nt or $D_i = 1$
N += ΔN
Open inp. file to do the contact geometry update modifying the nodal positions

Figure 4.6: FE-based model for wear analysis using the moving node technique.

4.3.4 Crack propagation direction

There are several methods available in the literature widely used to predict the crack trajectory such as: the Maximum Tangential Stress criterion (MTS) [57], the Maximum Energy Release Rate criterion (MERR) [75] and the zero K_{II} criterion ($K_{II} = 0$) [40]. These methods are already implemented in the commercial FE software ABAQUS 6.14. Despite the popularity and easy implementation of these methods, their performance in applications such as fretting fatigue was unsatisfactory. It was demonstrated in the work carried out by [84] and [132]. The fretting problem not only presents a non-linear behavior, i.e., it is load history-dependent, but also has a non-proportional load [158]. This explains why traditional methods are unable to predict the crack path in fretting problems.

Navarro et al. [117] proposed a methodology to predict the crack propagation in fretting fatigue problems without including one crack on the mesh. This methodology is based on multiaxial models of critical plane. Where the parameter is calculated for all points along a straight line of an arbitrary length starting from the contact trailing edge ($x = a$) and forming an angle θ with a line perpendicular to the contact surface, as shown in Figure 4.7(a). The material plane that coincides with that defined by θ is considered for the criterion parameter evaluation instead of use that plane that produces the maximum parameter value. This is repeated for different values of θ and using the average value of each straight line is obtaining the polar contour depicted in Figure 4.7(b). This methodology assumes that those lines having the higher mean values of the parameter along a certain length are more likely to initiate cracks. The results obtained by Navarro et al. [117] shown that the prediction by using the SWT parameter has been much closer to the experimental crack path than the FS parameter.

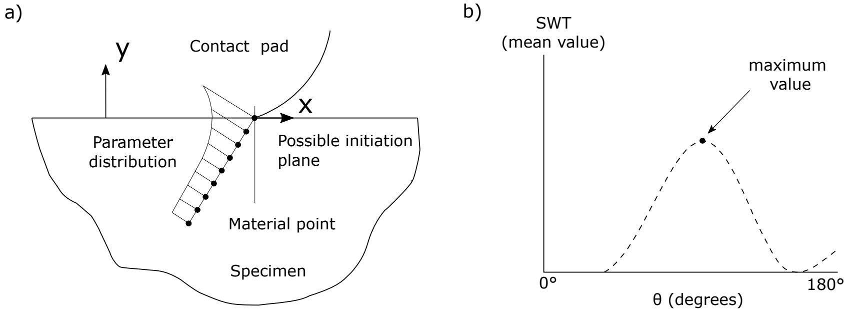

Figure 4.7: Illustration of the strategy used to $(SWT_{mean})_{max}$.

In this work, an adaptation of this method described above was carried out. For a better understanding, we call this approach $(SWT_{mean})_{max}$. The procedure is exactly the same with the difference that now a crack is included in the mesh using the XFEM method. Basically the $(SWT_{mean})_{max}$ defines that the crack will grow in the plane where the average of the SWT parameter values is maximum.

Two other alternative methods to compute the crack path, also based on the SWT

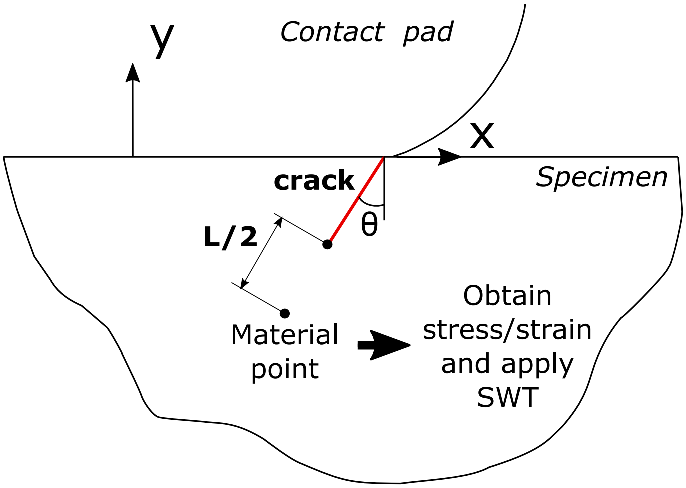

Figure 4.8: Illustration of the strategy used to SWT_L.

parameter, are here proposed. The first, SWT_{tip}, considers the stress/strain history at a single material point on the crack tip to obtain the orientation of the incremental crack growth plane. Such procedure is then repeated at each step of the simulation until the crack reaches 2 mm size (size of the experimentally detected cracks to stop the tests). The second method, denominated SWT_L, computes the SWT crack orientation plane from the stress/strain history of material point distant $L/2$ from the crack tip, Figure 4.8, where L is the critical distance given by Eq. (2.46).

The XFEM approach (eXtended Finite Element Method) was used to model the crack and apply the SWT_L method. Regarding the contact conditions between the crack faces, the Penalty approach was used to define the frictional contact constraints for both normal and tangential behavior of the surface. The Paris law was then used for calculating the number of cycles to final rupture. After a convergence analysis, the crack propagation increment, Δa, was chosen as 100 μm and the crack propagated until $\Delta K_{eq} = K_{Ic}$. The crack growth rate is related to ΔK and written as:

$$\frac{\Delta a}{\Delta N} \approx \frac{da}{dN} = C\left(\Delta K\right)^m, \tag{4.5}$$

where 1.41×10^{-12} (mm/cycle)/(MPa$\sqrt{mm}$) and m = 3.353 are material constants [84]. In this investigation for mixed-mode loading, ΔK was replaced by an equivalent SIF given by:

$$\Delta K_{eq} = \sqrt{\Delta K_I^2 + \Delta K_{II}^2}. \tag{4.6}$$

Therefore, the number of cycles to crack propagation was calculated using:

$$\Delta N = \frac{\Delta a}{C\left(\Delta K_{eq}\right)^m}. \tag{4.7}$$

4.3.5 Numerical model and boundary conditions

Figure 4.9 depicts the FE model. A coarser mesh is used far from the contact region, whereas, a refined one is considered near the contacting surfaces. In the refined region, a structured mesh with linear quadrilateral elements are used with an approximate size of 11.5 μm. Outside the refinement zone, the mesh is not structured but is formed by the same kind of elements. For all simulations plane strain elements are considered in the analyses. P is the normal load, Q represents the tangential load, and B is the bulk fatigue load. In all tests, P is remained constant while Q and B have loading ratios R = -1 and R = 0.1 respectively. As shown in Figure 4.10, the mean bulk fatigue load is applied first and remains constant, on the second step of the simulation is applied the normal load and in the third step, the bulk fatigue and tangential load are cycled. Pad radius is R_p = 50 mm. Multi-point constraints are enforced on the upper surface of the pad so that rotation is prevented. Regarding the contact conditions, the Lagrange multiplier approach was used to define the frictional contact constraints, and the contact nodes located at the specimen were defined as the master ones while the slave nodes were set on the pad.

4.4 Results and discussions

4.4.1 Validation of the XFEM method for crack propagation

The first tests done with the XFEM method were performed using a cracked plate under tension as illustrated in Figure 4.11(a). Where, b=50mm, h=50mm, t=10mm and a=5mm (a_i/b = 0.1 and a_f/b = 0.28). The crack was modeled using the software ABAQUS 6.14. Figure 4.11(b) shows how this crack was modeled and the mesh size used. The mesh size was 0.7mm and the crack face was modeled through the elements. Note that the crack tip is located at the edge of the last element.

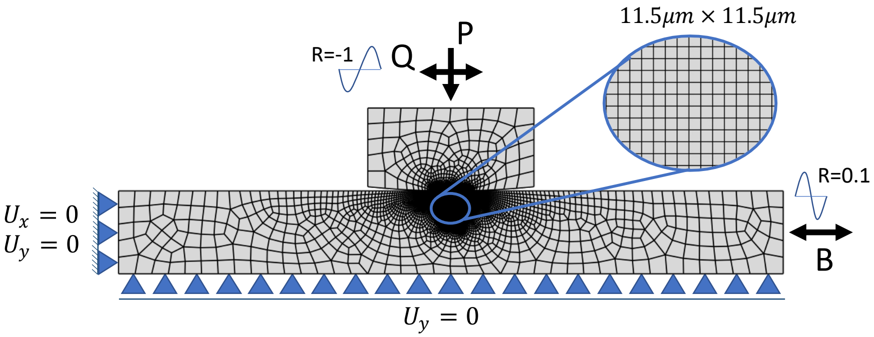

Figure 4.9: FE model for the fretting fatigue problem.

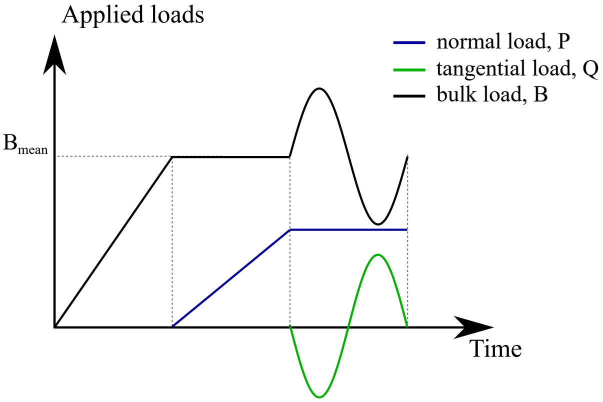

Figure 4.10: Loading scheme.

Figures 4.12(a) and (b) show the variation of the stress intensity factor K_I and K_{II} respectively for an initial crack of 2mm in a loading cycle with R = 0. For two-dimensional problems, the XFEM method was implemented on Abaqus to crack growing in monotonic loading. Therefore, the XFEM formulation related to the enrichment of the nodes at the crack tip is neglected. Thus, the K_I and K_{II} values obtained using the first contour (crack tip position) are underestimated, as can be seen clearly in Figure 4.12(a).

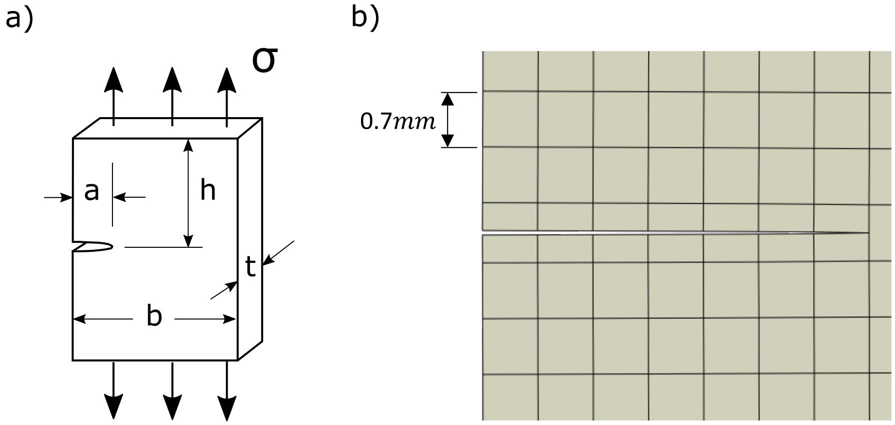

Figure 4.11: Cracked plate under tension (a) and crack modeling with XFEM(b).

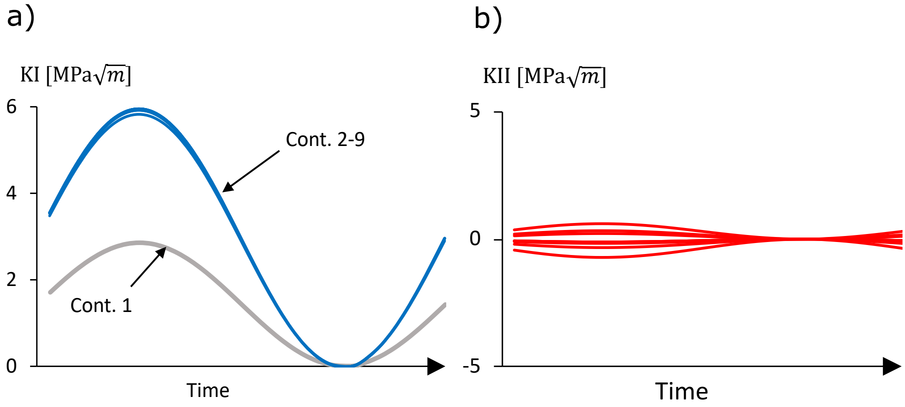

Figure 4.12: Time variation of K_I (a) and K_{II} (b).

With these in mind, the analysis was carried out using only the contours up 2 to 9. Figure 4.13(a) shows the results of $\Delta K_{I,XFEM}$ and $\Delta K_{II,XFEM}$ obtained numerically against analytical values. The MTS method was used to estimate the crack propagation angle. The final result of the crack trajectory and the stress field around the crack tip can be seen in Figure 4.13(b).

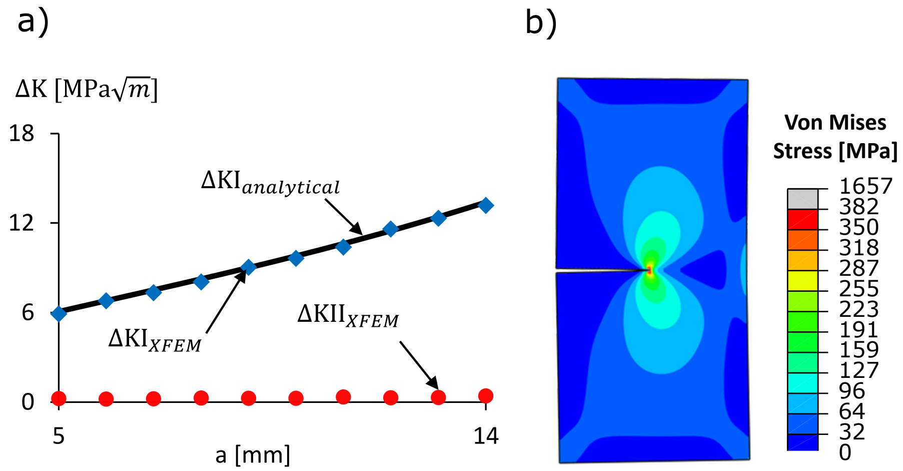

Figure 4.13: Analytical vs numerical stress intensity factor (a) and numerical results of the stress field at the crack tip (b).

As previously mentioned, when the crack is modeled in two-dimensional problems with XFEM in Abaqus the crack tip enrichment is neglected. So, the best strategy would be to ignore the K_I and K_{II} values obtained on the first contour. The numerical values for K_I and K_{II} obtained this way showed to be in good agreement with the analytical solution, the divergence is insignificant. As the loading condition used for this validation is proportional the MTS method resulted in a good crack trajectory prediction.

4.4.2 Comparison between different crack path prediction methods

The well-known methods for crack path prediction are Maximum Tangential Stress (MTS), $K_{II} = 0$, and Maximum Energy Release Rate (MERR) among others. These three methods are already implemented as a standard tool in Abaqus. Despite being well known and used, these methods do not take into account the non-linear behavior and the effects of non-proportional loading. Therefore, a new method is introduced to predict the crack propagation path under non-proportional loading conditions which is based on calculating the critical plane, based on the SWT damage parameter, at and near the crack tip. Three different values of SWT damage parameters are calculated, i.e. $(SWT_{mean})_{max}$, SWT_{tip}, SWT_L.

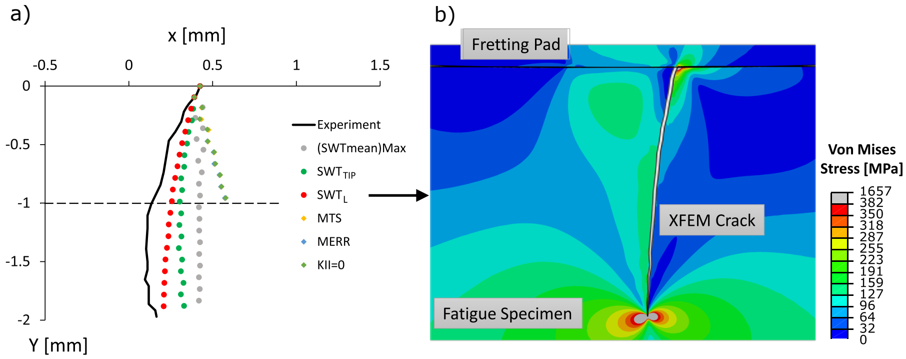

Figure 4.14: Comparing the estimated crack propagation path using different criteria and the experimental observation.

Figure 4.14 compares the estimated crack propagation path using different criteria and experimental observation. As expected, the traditional methods (MTS, MERR, and $K_{II} = 0$) that do not take into account the effects of non-proportional loading underperformed, where the crack propagates in the opposite direction to the direction of propagation observed experimentally. The three methods based on the critical plane multiaxial model had better results, where the method that applies the SWT parameter at a critical distance, $L/2$, had a better response. The use of stress in $L/2$ for the calculation of the critical plane avoids the effects of the stress gradient at the crack tip, this may explain the crack path estimated smoother than with the other methods.

Convergence analysis

The previous analyses have shown that the SWT_L method performed better to predict the crack path. Therefore, three tests were carried out with different mesh sizes to verify the influence of the mesh on the crack path and later on the K_I and K_{II} values.

Figure 4.15(a) shows that the mesh size does not interfere with the expected crack path. This is because the proposed method is based on the stress and strain field close to the crack. Therefore, as long as the mesh is refined enough to obtain a good estimate of the stress/strain field, the size of the elements will no longer interfere with the estimate of the crack propagation angle.

However, Figure 4.15(b) shows that when is used mesh size of 46μm there is a small variation for $\Delta K_{eq}/K_c$ in the initial crack growth phase, in which $\Delta K_{eq} = \sqrt{\Delta K_I^2 + \Delta K_{II}^2}$ and K_c is the fracture toughness. As the XFEM method allows complete separation of the element at the crack tip. The ratio between mesh and crack increment size, $Mesh/$da, should be as small as possible. In this study da=100μm was used, so a mesh with 46μm elements size represents almost 50% of da. This makes the crack after the simulation greater than expected, causing a significant error in the life estimate, as shown in Figure 4.16. Note that for meshes with elements smaller than 23 μm the results start to converge.

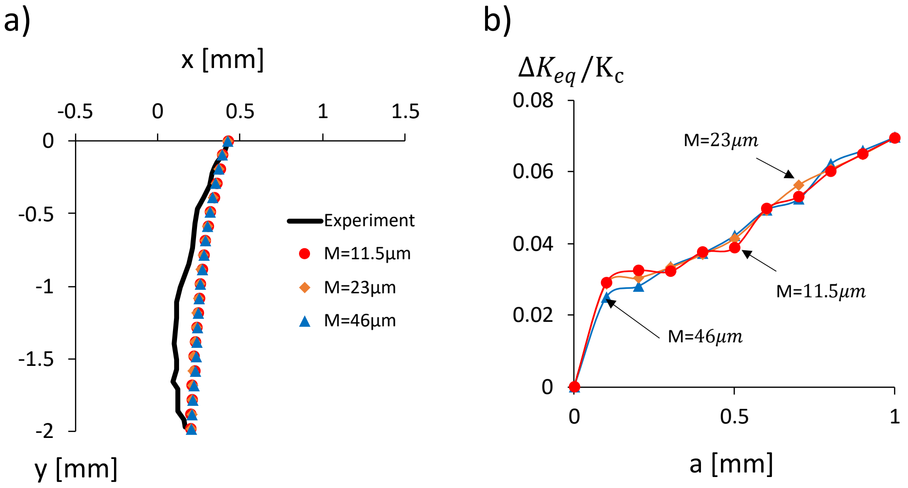

Figure 4.15: Convergence analysis using different mesh size: crack path (a) and Stress Intensity Factor variation (b).

4.4.3 Application of XFEM and SWT_L method for crack propagation life and path estimation

The previous results showed that the XFEM method can be used to calculate the SIFs (Stress Intensity Factors) with good accuracy. It was also observed that the SWT_L method has a better performance for crack trajectory prediction

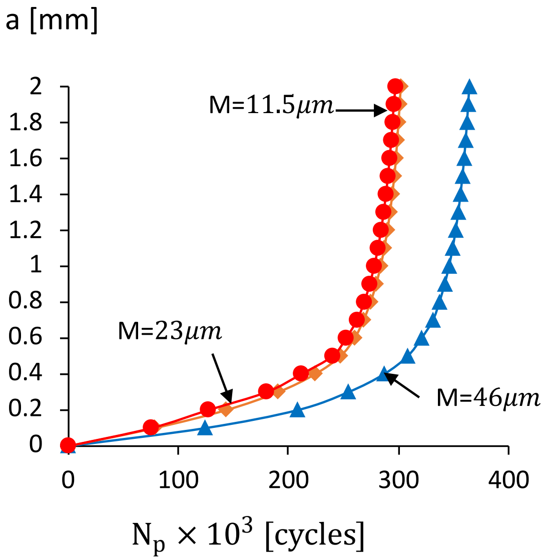

Figure 4.16: Life estimation using different mesh size.

than the usual methods that do not consider non-proportional loading effects. With this in mind, these two techniques were used to estimate the life and crack trajectory of the fretting fatigue tests performed by Talemi et al. [84].

Crack path and propagation life analyses

The crack nucleation position was calculated based on the maximum energy dissipated at the contact interface during one full cyclic loading condition. The crack initiation angle was defined as based on experimental observation. Figure 4.17(a) shows the trajectories obtained using the methods proposed in this work. It is noted that, even with the increase in the magnitude of the loads and different initial crack location, the trajectory of the crack is practically the same for all cases. However, despite a similar trajectory, the crack propagation life can be quite different, as shown in Figure 4.17(b).

The large variation in the estimated life is because tests with load configurations of greater magnitudes have a higher initial $\Delta K_{eq}/\Delta K_{Ic}$ ratio, as shown in Figure 4.18(a). This implies that loads with this higher initial ratio will reach faster the crack propagation stage III, in other words, will have shorter lives.

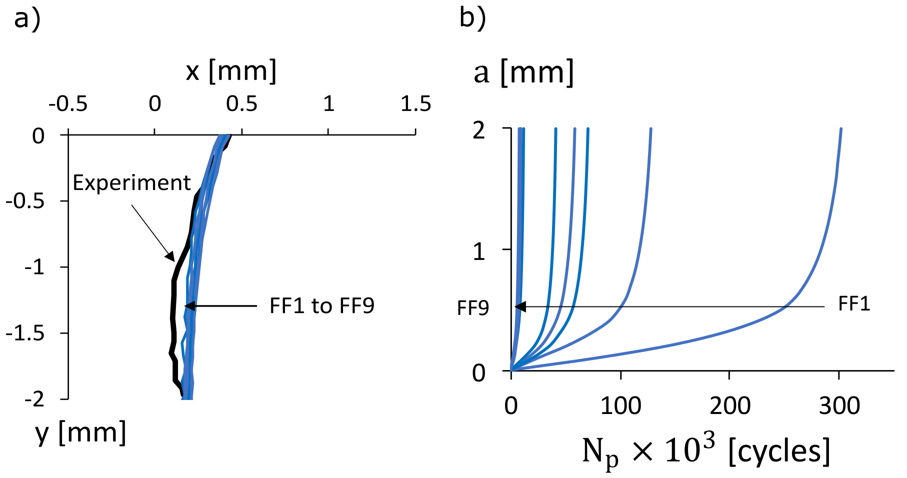

Figure 4.17: Crack propagation trajectory (a) and Variation of the crack length versus crack propagation life time (b) for FF1–FF9.

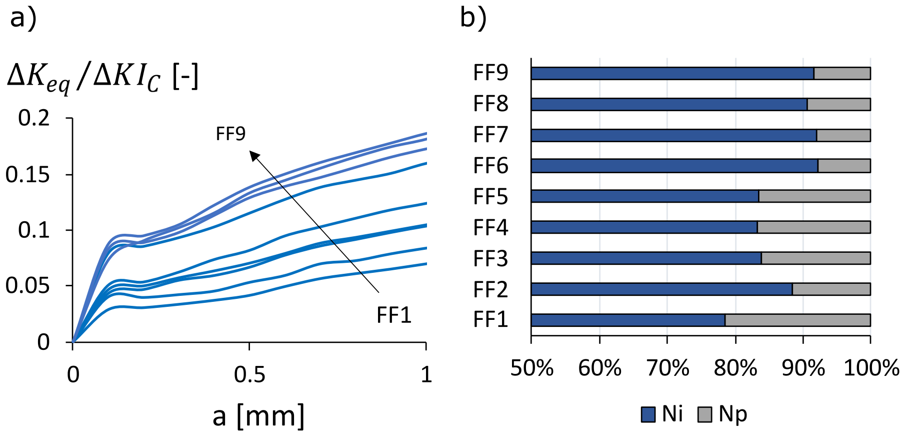

Figure 4.18: Variation of normalized equivalent SIFs versus the crack length for FF1–FF9 (a) and Estimated percentage of fretting fatigue crack initiation and propagation lifetime (b).

Figure 4.18(b) shows the percentage of crack propagation life estimated for all tests performed in this work. As can be seen, subtracting the crack propagation life estimated by the total experimental life, we have an average estimation of 86% of the total life composed by the crack initiation life.

Life assessment without the wear effects

In this section, two different approaches were used to estimate life (method 1 and 2). In the method 1, the stress/strain history in a single material point is used to estimate life. The abscissa of such a point is defined where the dissipated energy is maximum, Eq. (4.1), while the ordinate is located at a critical distance from the contact surface, $L/2$. L, is determined by Eq. (2.46). Generally, stresses/strains at a distance $L/2$ from the contact surface are used to mitigate the effects of the high-stress gradient generated by the contact surface. In this first approach, the parameters SWT and FS, calibrated for total failure, are used to estimate life.

In the method 2, more complex than the first, life is divided between crack nucleation, N_i, and crack propagation life, N_p. In which, the sum of the two represents the total life. For the calculation of N_i, an approach similar to the first method is used. The stress/strain history of a given point is also used to estimate life. However, in this case, the multiaxial parameters used are calibrated for crack nucleation and not to total failure. In addition, the coordinates of this point is defined horizontally as the one where the dissipated energy is maximum, Eq. (4.1). Figure 4.19 shows the dissipated energy profile in all the tests analyzed and a table with the location where the E_d is maximum. Vertically, it is defined as the critical distance from the contact surface, $L/2$. The propagation life, N_p, is obtained through the solutions proposed by means of Paris law and the techniques developed in Section 4.4.3. Thus, the total life is $N_f = N_i + N_p$.

Figure 4.20 presents the results for the two approaches. In which, $N_{f,SWT}$ and $N_{f,FS}$ are the results for the method 1 (without crack propagation) using the parameters SWT and FS respectively. And the results of the method 2 are $N_{i,SWT} + N_{p,XFEM}$ and $N_{i,FS} + N_{p,XFEM}$ for the parameters SWT and FS respectively. In this figure, the predicted life is plotted against the experimental life and delimited by a scatter band equal to 2. The results in Figure 4.20 show that for long lives FS parameter has a greater error since most of the results are above the solid line, while SWT presents better and more conservative performance. On the another hand, for short lives both SWT and FS are conservative. Although $N_{f,SWT}$ fall out the scatter band 2, the error is close to

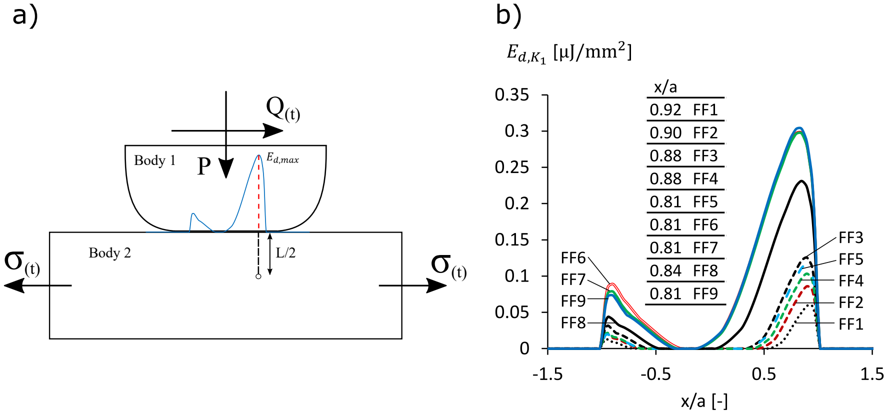

Figure 4.19: The energy dissipated along the surface contact for FF1-FF9.

50%. However, using the method $N_{i,SWT} + N_{p,XFEM}$ this problem is solved and all data fall into the scatter band 2.

4.4.4 Effects of fretting wear process on fatigue crack propagation

In this section, results will be presented including the effect of surface wear on the contact region during the crack nucleation phase (method 3). Wear effect can be computed using the local formulation of Archad's equation or the dissipated friction energy. In this work was adopted Archad's equation, which can be computed using Eq. (2.75). As shown in Section 4.4.3, the parameter SWT provides more conservative results than FS for the material in question. Therefore, in all tests including the wear effect, only the multiaxial parameter SWT was applied.

Figure 4.21(a) shows the difference between the contact surfaces before and after the effect of wear in the specimen FF4. There is a clear separation between the stick zone and slip zones. This is because the region where there is no relative slip the wear is not computed. The pressure distribution profile, depicted in Figure 4.21(b), has a small increase in the central region of the contact. However, while in the slip zones the pressure values are almost zero, peaks in the transitions between stick and slip zones are observed.

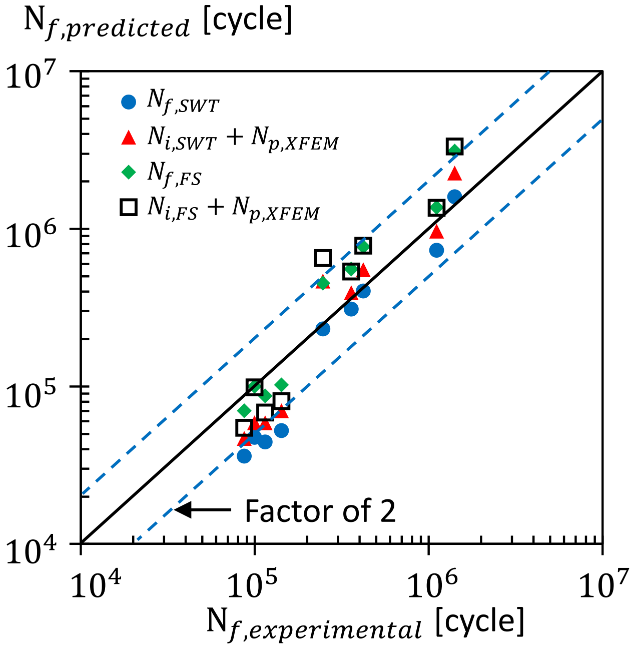

Figure 4.20: Estimated and observed fretting fatigue lives without and with crack propagation.

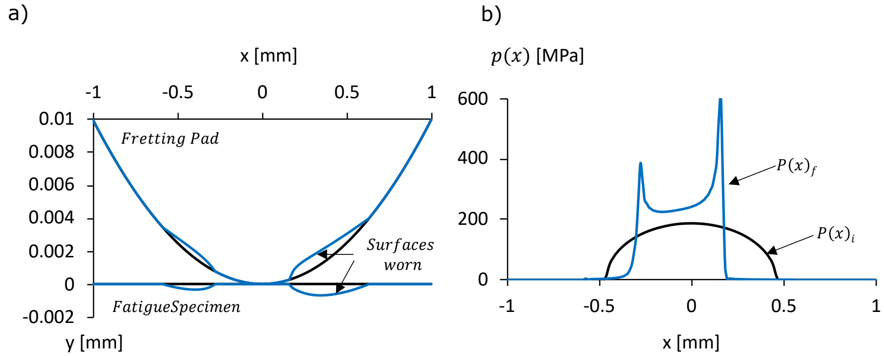

Figure 4.21: Comparison between surfaces (a) and normal pressure distribution (b) after wear process to FF4 test.

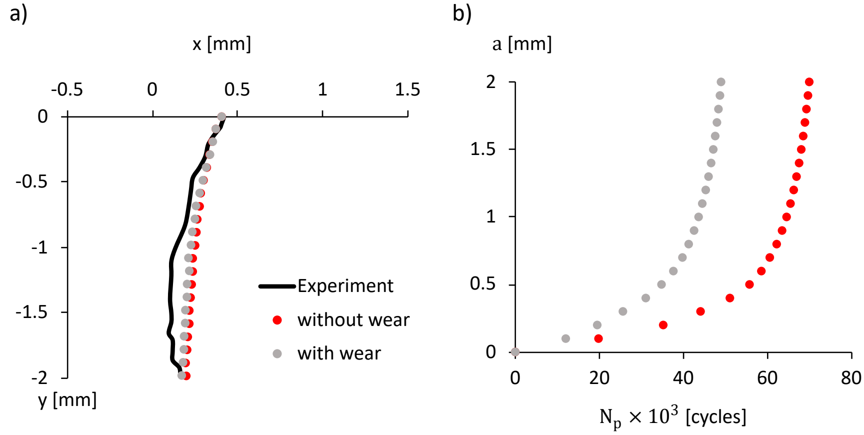

Figure 4.22: Comparison between crack path (a) and crack propagation life (b) after wear process to FF4 test.

Figure 4.22 shows the crack propagation results using the methods described in the previous sections with and without the wear effect. In Figure 4.22(a) it is observed that the inclusion of wear practically does not change the crack path. On the other hand, the crack propagation life with the worn surface is approximately 30% less than when the wear effect is neglected. The results presented in this section are only for the FF4 test. The same behavior was observed for all tests.

As stated earlier, the SWT parameter has been more conservative in general than the FS. Therefore, the analysis including wear was performed only with the SWT. The results of life assessment can be seen in Figure 4.23. It is noted that when the model is applied conventionally (method 1), i.e., without including wear effect and crack propagation, the life predictions are close to the experimental results for longer lives. While, in tests with shorter lives, the results fall out the scatter band 2.

Using the methodology where life is separated into nucleation and crack propagation life (method 2), there is a small improvement in data that fell out the scatter band 2. The other tests continue within the desired region, but with less conservative predictions and a dispersion a little higher in these cases. Taking wear into account in the crack initiation phase (method 3) could correct the dispersion previously found for tests with longer life and the life estimation remained conservative. However, the life predictions were very close to those

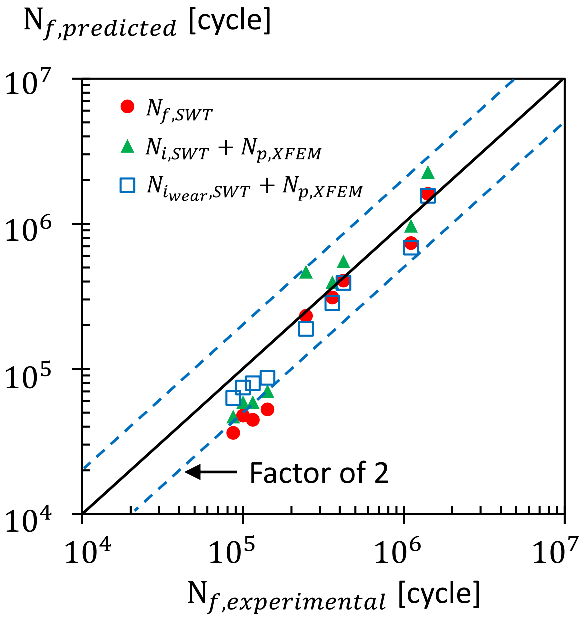

Figure 4.23: Estimated and observed fretting fatigue lives without and with crack propagation including wear effect.

obtained without wear effect and crack propagation life. The inclusion of the wear effect brought a clear benefit for tests with a shorter life, which not only falls into the scatter band 2, but the error in the prediction became smaller than in the other two approaches.

Over time, surface wear changes the contact geometry by increasing the stress concentration. Apparently, with higher stresses, the life estimate should be lower. However, the material loss on the contact surface, in theory, can remove micro-cracks causing retardation in the nucleation of new cracks. Consequently, this behavior generates an extension of life. In numerical terms, the movement of the nodes on the contact surface represents this loss of material. This movement reflects the damage accumulation in each element since the incremental damage from the previous step is interpolated to the new position with the worn surface. This process delays the evolution of the damage providing a longer life estimate. This behavior explains why there was an improvement in the estimated data, mainly in those tests with shorter lives.

In this work, among the three methodologies covered, two of them separate the total life between crack nucleation life, N_i, and crack propagation life, N_p.

Table 4.1: Result of life assessment: with and without take wear into account, checking the influence of wear in N_i and N_p.

	With wear		**Without wear**		$(\mathbf{N_{i,p_{wear}}} - \mathbf{N_{i,p}})/\mathbf{N_{i,p}}$		
Test	$\mathbf{N_i}$	$\mathbf{N_p}$	$\mathbf{N_i}$	$\mathbf{N_p}$	$\mathbf{\Delta N_i}$	$\mathbf{\Delta N_p}$	$\mathbf{\Delta N_f}$
FF1	1,390,000	168,200	1,967,600	301,761	-29%	-44%	-31%
FF2	600,000	86,010	840,270	128,359	-29%	-33%	-29%
FF3	242,000	41,600	336,880	57,788	-28%	-28%	-28%
FF4	342,000	48,690	480,560	69,944	-29%	-30%	-29%
FF5	162,000	26,600	425,140	40,705	-62%	-35%	-60%
FF6	78,000	9,003	59,164	11,218	32%	-20%	24%
FF7	72,500	7,192	49,763	9,087	46%	-21%	35%
FF8	67,000	7,129	49,418	9,348	36%	-24%	26%
FF9	57,000	5,981	39,741	7,244	43%	-17%	34%
				Mean	-2%	-28%	-6%

However, in one of these approaches, the wear effect is considered to compute N_i. Table 4.1 presents the results of life estimates for these two methodologies and compares the difference in the estimate of N_i and N_p. It is noted that the inclusion of wear has increased the estimated total life for some tests while for others there is a reduction. As previously mentioned, the inclusion of wear in the analysis generated a reduction in the estimated values of N_p for all tests, with an average reduction of -28%. However, the tests with shorter lives (FF6 to FF9) had an average increase in N_i of 39%, while the other tests (FF1 to FF5) showed an average reduction of -35.4%. A similar result is seen when assessing total life.

The variation in energy dissipated at the contact surface can be used to explain why the inclusion of surface wear has brought clear benefits for some cases and others not. Ruiz et al. [140] proposed two damage parameters for the fretting fatigue problem. One of these parameters, the fretting wear parameter, basically calculates the amount of frictional work at the contact interface and can be written as $K1 = \tau \times \delta$. The second parameter is called fretting fatigue parameter and can be written as $K_2 = \tau \times \delta \times \sigma_x$. The concept of cumulative dissipated energy, E_d, introduced by [111] is the summation of parameter $K1$ in each increment of the time during one full cyclic loading condition.

With this in mind, it can be said that the higher the value of $K1$ and consequently E_d, the greater will be the effect of wear in the failure mode of the material. Figure 4.19 shows that the tests FF6 to FF9 are the tests with the highest values of dissipated energy. The hypothesis that tests with a higher E_d values would be more affected by wear is confirmed when we verify the results in Figure 4.24. In this figure, the maximum energy dissipated is related to the error in life assessment of each test for each numerical model proposed. This error is the subtraction between the experimental life and the life estimated numerically. The tests that presented the highest values of E_d had fewer errors in the life prediction when the wear is taken into account. It is also noted that for $E_d < 0.2\mu J/mm^2$, in terms of life assessment there is no need for computed wear, as the results are very close to the results obtained by the conventional method where the processing cost is much lower.

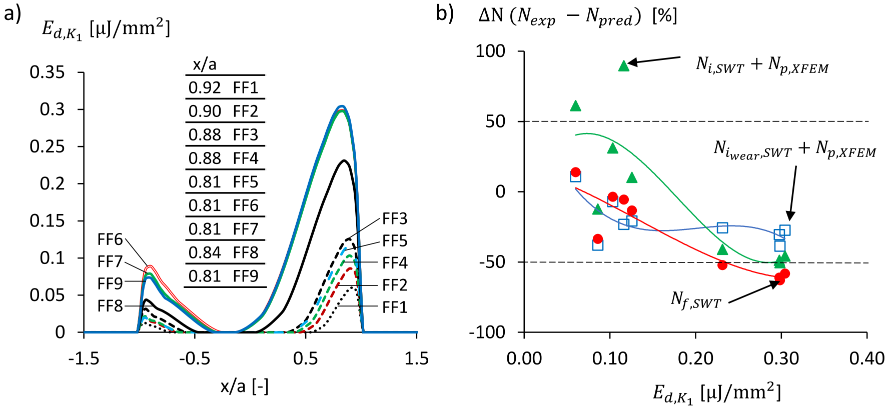

Figure 4.24: Correlation between maximum energy dissipated with life prediction error.

Parameter $K1$ does not consider the effects of tangential stress on the fatigue specimen or the normal load on the pad. The inclusion of the load effect can be done by normalizing parameter $K2$ with the maximum normal pressure, p_0, as shown in Figure 4.25. Note that considering the normalized $K2$ parameter, the observed behavior is similar to that in Figure 4.24(b). But now it can be said that for dissipated energy values $E_d < 0.04\mu J/mm^2$ there is no need to compute the surface wear.

4.4.5 Results using the critical distance as a function of life

In the previous sections, the results presented were obtained using the critical distance as a fixed value. In this section, on the other hand, the three methods presented in Section 4.2 will be applied considering using the critical distance as a function of life, L_M. The wear was computed only during the crack nucleation phase, as described in Section 2.7. Figures 4.26(a) and (c) present the results

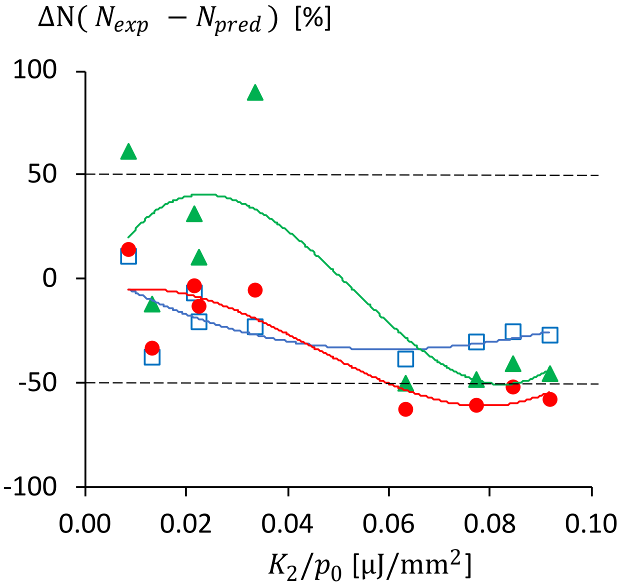

Figure 4.25: Correlation between maximum energy dissipated normalized with life prediction error.

of the worn profiles and Figures 4.26(b) and (d) present the contact pressure distribution, σ_y, after wear. As can be seen, all tests are in a partial slip regime, that is, there is one stick zone and two slip zones. However, the FF6-FF9 tests have much larger slip zones and consequently a small stick zone. This characteristic of the FF6-FF9 tests, in addition to causing a higher pressure peak than in the other tests, also generates higher wear damage. Thus, the inclusion of such an effect in the life estimation methodology can be extremely important. Although the contact pressure is quite high, especially in the FF6-FF9 tests, this occurs locally, only near the stick zone and after wear has been almost completely evolved. Therefore, there is no need to be taken into account the plastic deformation flow.

The crack initiation point is defined as the one where E_d is maximum, as in Figure 4.19. For all cases, the initial crack size is 100 μm and θ =75° (θ was represented in Figure 4.8). The initial crack angle was measured for a crack of the same length based on the experimental results presented by [84] Figures 4.27 and 4.28 present respectively the prediction of the crack path and the propagation life, N_p. Note that the inclusion of wear did not change the

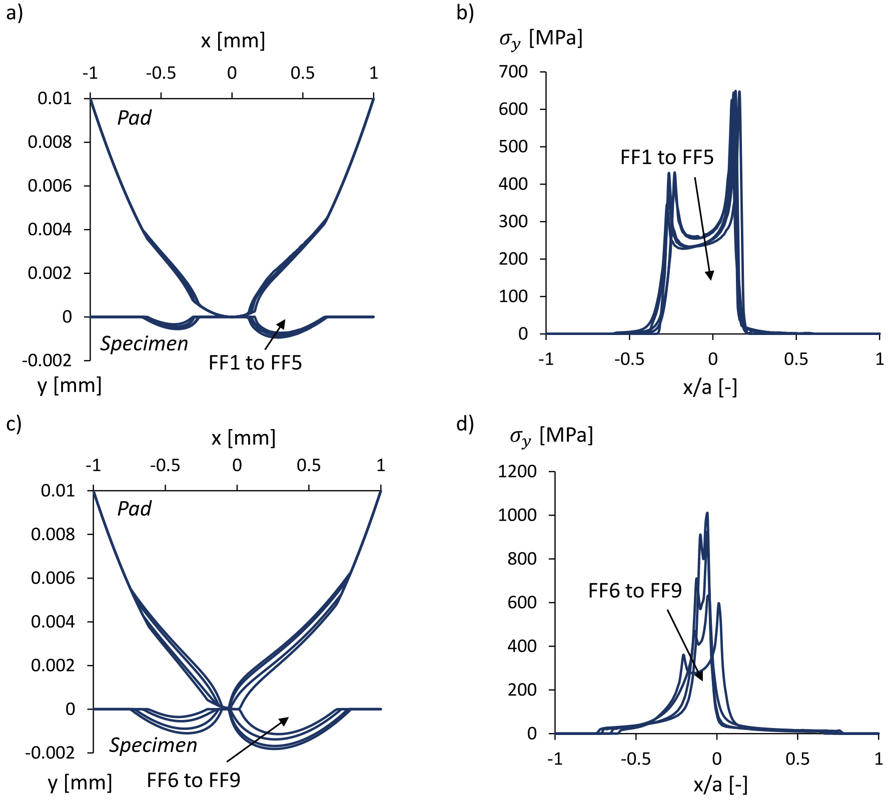

Figure 4.26: Comparison between surfaces worn from FF1 to FF5 (a) and from FF6 to FF9 tests (c), normal pressure distribution from FF1 to FF5 (b), and from FF6 to FF9 tests (d).

crack path, however, there is a significant reduction in propagation life (Figure 4.28(b)). This variation in life is due to a change in the distribution of normal pressure. With higher stress the values of ΔK_{eq} also increase, causing a decrease in the life estimate.

Figure 4.29 shows the results of life estimation for the three methods proposed. Figure 4.29(a) presents these results considering the fixed critical distance, $L/2 = 23\mu m$. Figure 4.29(b) in turn, presents the results considering $L_M = A(N)^B$. Note that N_f = Method 1, $(N_i + N_p)$ = Method 2 and $(N_{i,wear} + N_p)$ = Method 3. When the critical distance with a fixed value is used, Figure

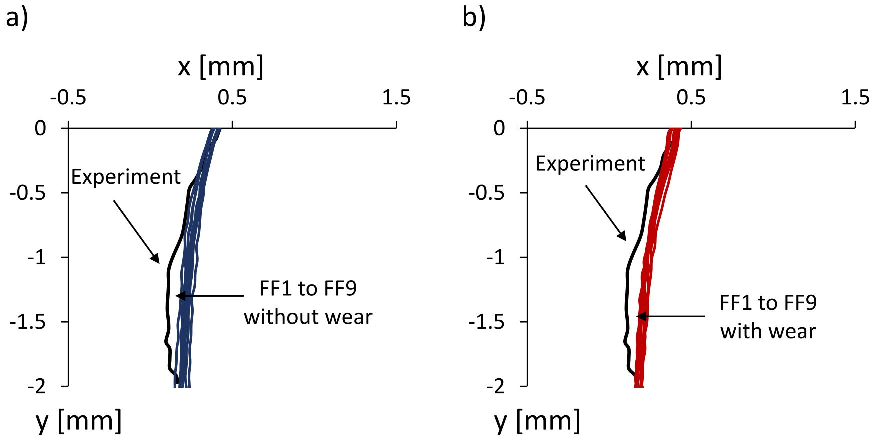

Figure 4.27: Crack path without wear (a) and with wear effects (b).

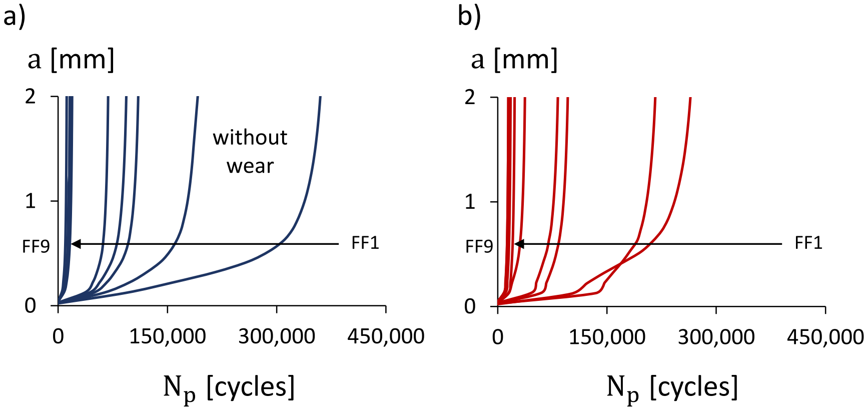

Figure 4.28: Crack propagation life without wear (a) and with wear effects (b).

4.29(a), it is observed that only method 3 obtains all results within a scatter band of 2. An analysis of the energy dissipation showed that the tests FF6-FF9 had $E_d > 0.2\mu J/mm^2$, and Figure 4.26(c) shows that these are the tests with the highest surface wear. For this reason, the inclusion of wear (method 3) becomes essential in the methodology with constant L. On the other hand, when using the critical distance as a function of life, $L_M = A(N)^B$, all methods present results within a scatter band of 2. As shown in Figure 4.29(b), methods 1 and 2 have similar results, and only for the FF6-FF9 tests (those with greater wear sensitivity) method 3 provided more accurate results. It is important to mention that the computational cost of method 1 is extremely low, a test takes about 5min. Method 2 has a slightly higher cost as it includes crack modeling, something around 2h. On the other hand, method 3 has an extremely high computational cost and depends on the estimated life, which can vary between 5 or 10h (considering the simulation of wear and crack propagation).

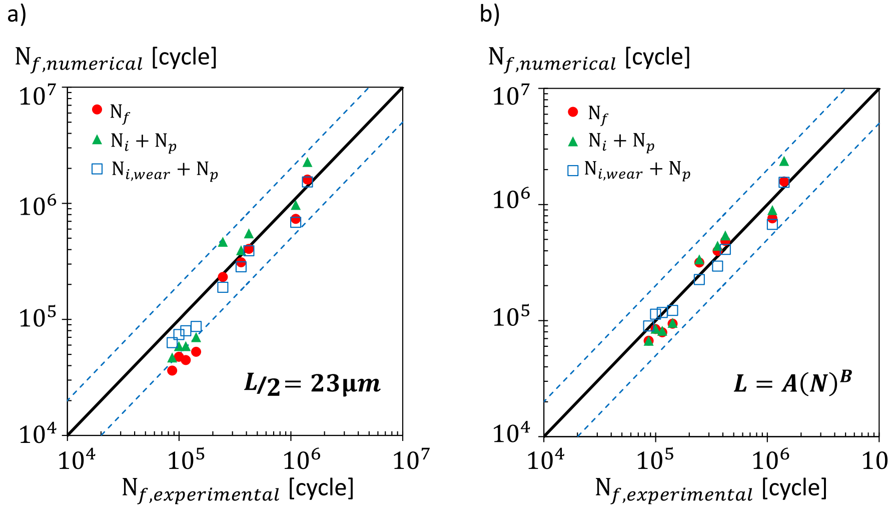

Figure 4.29: Fretting fatigue life assessment for tests FF1-FF9 with fixed (a), and variable (b) critical distance.

Table 4.2 presents the results of Figure 4.29 and Table 4.3 shows the percentage of the total fatigue life related to the crack initiation phase. As can be seen, N_i represents 86% and 89% of N_f for methods 2 and 3 respectively when using fixed L. When L is used as a function of life N_i represents 89% in both methods.

Table 4.2: Fretting fatigue life assessment for tests FF1-FF9.

	$L/2 = 23\mu m$			$L = A(N)^B$		
Method	**1**	**2**	**3**	**1**	**2**	**3**
FF1	1,603,400	2,269,361	1,528,200	1,581,703	2,371,374	1,550,500
FF2	734,520	968,629	686,010	760,625	894,489	673,670
FF3	310,270	394,668	283,600	397,724	440,621	294,570
FF4	405,000	550,504	390,690	485,803	541,034	410,490
FF5	232,130	465,845	188,600	316,379	336,589	226,030
FF6	52,620	70,382	87,003	93,920	95,503	122,250
FF7	44,612	58,850	79,692	79,184	81,814	117,297
FF8	47,650	58,766	74,129	84,631	85,082	113,407
FF9	36,194	46,985	62,981	67,080	67,095	89,871

Table 4.3: Percentage of the total fatigue life related to the crack initiation phase.

	$L/2 = 23\mu m$		$L = A(N)^B$	
Method	**2**	**3**	**2**	**3**
FF1	87%	91%	88%	90%
FF2	87%	87%	85%	88%
FF3	85%	85%	88%	88%
FF4	87%	88%	88%	90%
FF5	91%	86%	90%	75%
FF6	84%	90%	89%	92%
FF7	85%	91%	89%	94%
FF8	84%	90%	90%	93%
FF9	85%	91%	90%	93%
Mean	**86%**	**89%**	**89%**	**89%**

Table 4.4 presents the results of Figure 4.29 in terms of the error in life estimation. This error is calculated as follows:

$$Error = \frac{(N_{f,numerical} - N_{f,experimental})}{N_{f,experimental}}. \tag{4.8}$$

The results of Table 4.4 show that the average errors in the life estimate are smaller when using $L = A(N)^B$. Except for method 2, however, it presented a very large dispersion when using constant L and a standard deviation of 52%. Methods 1 and 3 showed more conservative results considering the average error for both situations, constant or variable L.

Table 4.4: Life estimation error, the mean and standard deviation of the error.

	$L = A(N)^B$			$L/2 = 23\mu m$		
Method	**1**	**2**	**3**	**1**	**2**	**3**
FF1	12%	69%	10%	14%	61%	9%
FF2	-31%	-19%	-39%	-34%	-12%	-38%
FF3	11%	23%	-18%	-13%	10%	-21%
FF4	16%	29%	-2%	-4%	31%	-7%
FF5	29%	37%	-8%	-6%	90%	-23%
FF6	-34%	-33%	-14%	-63%	-50%	-39%
FF7	-31%	-29%	2%	-61%	-49%	-30%
FF8	-15%	-15%	14%	-52%	-41%	-26%
FF9	-23%	-23%	4%	-58%	-46%	-27%
Mean	**-7%**	**4%**	**-6%**	**-31%**	**-1%**	**-22%**
Standard deviation	**24%**	**36%**	**16%**	**29%**	**52%**	**15%**

Chapter 5

Early crack orientation prediction methods under fretting fatigue loading including wear effects

“In this chapter is investigated two different methods to predict crack initiation direction in fretting problems subjected to partial slip conditions. In addition, the influence of considering wear in the crack initiation direction estimates is also investigated”

This chapter was previously published as:
PINTO, A. L., et al. Early crack orientation prediction methods under fretting fatigue loading including wear effects. International Journal of Fatigue, 2022, 161: 106893.

With respect to the original publication, a few symbols are changed to comply with the general nomenclature and certain paragraphs are modified slightly to avoid redundancy.

5.1 Overview

Strong optimum designing requirements by the modern industry in the recent decades led engineers and scientists to investigate fretting crack nucleation mechanisms closely, which resulted in the development of several methods aiming to predict early crack orientation. In 1994, Cheng et al. [35] considered dislocation pile-up to predict crack initiation life under contact fatigue. Seeking to apply a more practical approach, Szolwinski and Farris [157] used the Smith, Watson, and Topper (SWT) multiaxial fatigue damage parameter to assess fretting crack initiation lifetime, crack site location, and direction of early propagation. In 1997, Lamacq et al. [94] developed a theoretical model to predict fretting crack sites as well as their initiation directions. Besides, according to them, Stage I cracks might be divided in two groups: Type 1 when crack initiation is mainly influenced by the shear stress range and Type 2 when the normal stress range governs the process. Similar to the work of Lamacq et al. [94], Neu et al. [118] used several different critical plane approaches in an attempt to correlate the location of the fretting crack with experimental results on pH 13-8 Mo stainless steel. The fretting fatigue damage parameter proposed by Ruiz and Chen [141] was also investigated, and they stressed that this parameter could not capture the crack orientation, however, it could predict the crack initiation location.

Recently, Araújo et al. [25, 11] proposed The Critical Direction Method (CDM) in an attempt to predict crack initiation orientation in fretting problems. Since then, this method has become widespread because of its good accuracy and easy implementation. Firstly, the CDM was confronted with fretting tests conducted on steel alloys [65, 16]. In this case, [25] verified that the CDM in conjunction with the maximum normal stress range (Type 2 cracks) provided the best estimates. In [11] the same experimental data was considered; however, authors have obtained better estimates by applying the CDM in conjunction with a stress-based version of SWT parameter. Vantadori et al. [165] have considered the CDM for predicting the crack initiation angle of fretting tests conducted on an Al 7050-T7451 alloy. In this case, Carpinteri et al. [30] multiaxial fatigue model was utilized in the analyses. Almeida et al. [2] carried out fretting tests on an Al 7050-T7451 alloy aiming to investigate the influence of the following parameters on the crack initiation direction: tangential load amplitude, mean bulk stress and pad radius. This chapter also confronted the experimental observations with the CDM combined with different multiaxial fatigue parameters. In this setting, the SWT criterion yielded better estimates than the other two shear stress-based models assessed.

This chapter investigates two methods for predicting crack initiation direction in fretting problems. In one of them, the CDM is combined with the standard strain-based SWT parameter. In the second, early crack propagation is simulated using a Linear Elastic Fracture Mechanics (LEFM) approach associated with the SWT parameter. In addition, also investigates the influence of considering wear in the prediction of crack initiation path. The motivation for so comes from the fact that recent fretting modelling works [28, 5, 132] demonstrated that fatigue life estimates either considering or neglecting wear provide similar levels of accuracy when one has partial slip conditions. However, concerning crack initiation path, it is still needed to verify the impact of modelling wear on the results. For the simulation of wear, Archard's law is applied on a nodal basis through finite element (FE) simulations.

The methodologies for estimating the crack initiation angle presented in this chapter use the multiaxial fatigue parameter SWT. This was implemented as described in Section 2.2.2. The initial crack size, at which the initiation angle is to be estimated, has as a reference twice the size of the material critical distance, $2L$. This value is obtained by Eq. 2.46. More details on the Theory of Critical Distance can be found in Section 2.5. As mentioned, the methodologies proposed in this chapter will be investigated considering or not the effects of surface wear. To this end, wear modeling and damage accumulation is implemented as described in Section 2.7. The procedure for accumulating damage and updating the worn surface is the same as shown in flowchart 4.6. Results from the CDM and the LEFM approach assessed here are confronted with experimental data in the literature [2] and are presented in Section 3.3.3. Table 3.17 reports the loading conditions in each fretting fatigue test.

5.1.1 Multiaxial fatigue parameter calibration

One of the aims of this chapter is to investigate the wear effects on the estimate of crack initiation path in fretting problems. Therefore, wear has to be simulated up to the crack initiation lifetime. In this setting, the multiaxial fatigue model considered in the computation of fatigue damage (Eq. 2.78) has to be calibrated for crack initiation lifetime instead of total fatigue life. This subsection presents the strategy adopted in the calibration of the SWT materials' parameters for predicting crack initiation lifetime.

To obtain the S-N curve for crack initiation, it is necessary to discount the crack propagation life, N_p, for each fatigue test data of a given S-N curve for failure. Figure 5.1 illustrates how this procedure is conducted. Firstly, it is necessary to define an initial crack size, a_i, which was set as $2L$ in this chapter. The reason for so comes from the fact that the experimental fretting data assessed in this chapter evaluated crack paths up to this length. The S-N curve considered in this chapter was obtained from fatigue tests conducted on 7050-T7451 aluminum alloy flat dog-bone specimens subjected to fully reversed push and pull loading conditions, as shown in Figure 5.1 [90]. In this case, for each data on the S-N curve, crack propagation lifetime, N_p, can be computed according to Paris Law:

$$N_p = \sum \Delta N = \sum \frac{\Delta a}{C \Delta K^m} \tag{5.1}$$

where, C and m are materials constants and Δa is the crack size increment in the propagation process. The stress intensity factor range, ΔK, was obtained according to:

$$\Delta K = K_{max} = \sigma_{max} F \sqrt{\pi a} \tag{5.2}$$

where σ_{max} is the maximum stress in each test, a is the crack size and S is the shape factor for the specimen's geometry considered [49]:

$$F = 0.265 \left(1 - \frac{a}{w}\right)^4 + \left[\frac{0.857 + 0.265\frac{a}{w}}{\left(1 - \frac{a}{w}\right)^{\frac{3}{2}}}\right] \tag{5.3}$$

where w stands for the specimen's width. Notice that, in Eq. 5.2, negative stress intensity factor values were disregarded in the computation of ΔK by assuming that cracks do not propagate while closed. The crack propagation life in Eq. 5.1 is obtained when $K_{max} \geq K_{Ic}$.

Finally, from the S-N curve for crack initiation, the SWT parameter (Eq. 2.12) can be set for predicting the number of cycles necessary to initiate a crack of length a_i, as depicted in Figure 5.2.

5.2 Methodology

This sectoin presents two different methodologies for predicting the crack initiation direction when fretting under partial slip conditions takes place. In one of them, the CDM is used in conjunction with the SWT parameter. Alternatively, one also investigates a methodology based on LEFM crack propagation principles, which also relies on the SWT model. Although the CDM method has already been evaluated in other works [11, 165, 2], to the authors best knowledge, this is the first time that the influence of wear is included in the analysis in an attempt to see whether better predictions are achieved or not. Furthermore, the LEFM approach here investigated is often applied to model Stage II cracks. Here, on the other hand, one tests the applicability of this theory in modelling early

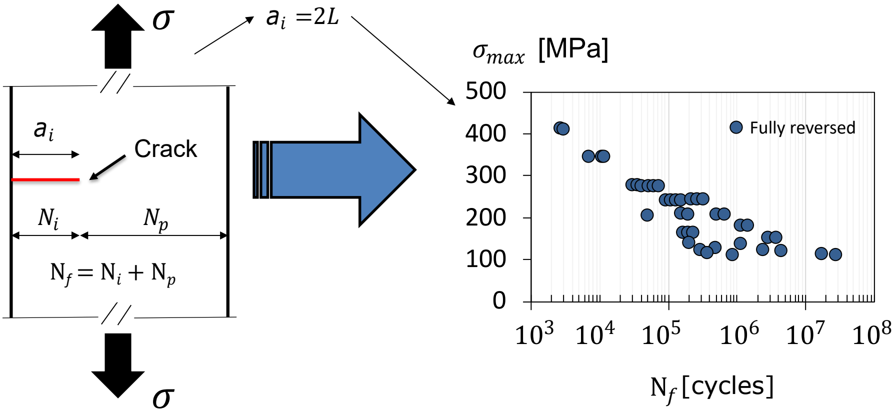

Figure 5.1: Calibration procedure to represent uniaxial fatigue data (Al 7050-T7451 [90]) in terms of crack initiation lifetime.

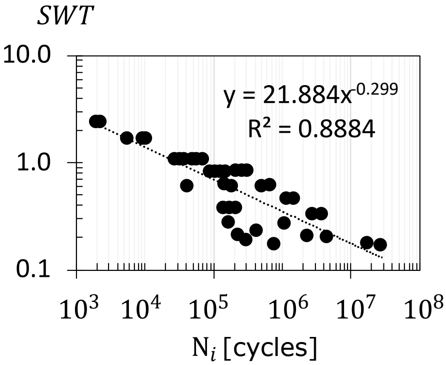

Figure 5.2: SWT parameter calibrated for crack initiation life.

crack propagation, including or neglecting wear effects. In the next subsections, more details are given concerning methods here investigated.

5.2.1 Method 1: Critical Direction Method

Consider a $2L$ length line oriented by an angle θ with respect to the axis perpendicular to the contact surface, Figure 5.3(a). In this case, the CDM basically consists in averaging stresses and strains over each possible θ line for further application in some multiaxial fatigue parameter. In this setting, the critical direction, i.e., the crack initiation orientation, is given by the angle that maximizes the considered multiaxial fatigue parameter. It is worth noting that during the averaging process along any θ oriented line, stresses and strains are always computed on the same θ planes (Figure 5.3(a)).

For the application of the CDM in conjunction with SWT parameter one needs to compute average normal stresses and strains for each possible orientation θ over time:

$$\bar{\sigma}_n(\theta,t) = \frac{1}{2L}\int_0^{2L} \sigma_n(r,\theta,t)dr \tag{5.4}$$

$$\bar{\varepsilon}_n(\theta,t) = \frac{1}{2L}\int_0^{2L} \varepsilon_n(r,\theta,t)dr \tag{5.5}$$

where $\sigma_n(\theta,t)$ and $\varepsilon_n(\theta,t)$ are the average normal stress and strain components, respectively, for a given θ line at the time t. Now, the obtaining of terms appearing in the SWT parameter (Eq. 2.12) is straightforward:

$$\bar{\sigma}_{n,max}(\theta) = \max_t[\bar{\sigma}_n(\theta,t)] \tag{5.6}$$

$$\bar{\varepsilon}_{n,a}(\theta) = \frac{1}{2}(\max_t[\bar{\varepsilon}_n(\theta,t)] - \min_t[\bar{\varepsilon}_n(\theta,t)]) \tag{5.7}$$

where $\bar{\sigma}_{n,max}(\theta)$ and $\bar{\varepsilon}_{n,a}(\theta)$ are the maximum normal stress and normal strain range, respectively, for a given θ direction. According to the critical plane definition considered in this work, crack initiation direction can be found by maximizing Eq. 5.7 with respect to θ.

Concerning the CDM, two different approaches namely Method 1-A and Method 1-B are considered in this work. In the former, the contact trailing edge, $-a$, is considered as the crack initiation point and the wear effects are not included in the analysis as can be seen in Figure 5.3(a). Method 1-B, on the other hand, has the same crack initiation point but includes contacting surface changes due to wear, Figure 5.3(b). The main difference between these two methods is that in the Method 1-A the CDM is applied to the initial contacting geometries, whereas in the Method 1-B, the CDM is employed considering the worn contacting surfaces in both fretting pad and fatigue specimen. In this case, the shape of the worn geometries is obtained by simulating wear up to the number of cycles necessary to initiate a crack of length $2L$.

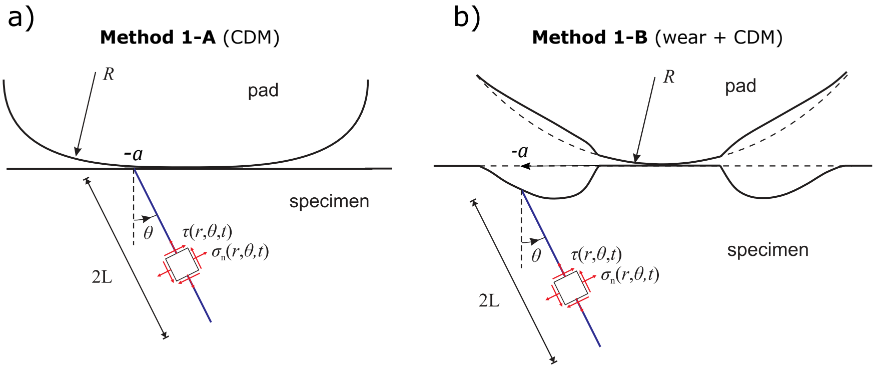

Figure 5.3: Schematic representation of CDM at the contact trailing edge: (a) without wear and (b) with wear. Positive θ angles in the counterclockwise direction.

It is worth mentioning that microcrack paths in fretting problems are affected by microstructural features (e.g., grain boundaries and crystallographic orientations) and localized plastic deformation near the surface. It is also noted that the orientation of the microcrack varies as the crack grows away from the contact. However, the average stress/strain quantities used in the CDM are based on homogeneous continuum elasticity assumptions. Accordingly, the critical direction provided by the proposed method should be regarded as an engineering estimate of the average path of a crack of length $2L$ emanating from the crack initiation site.

5.2.2 Method 2: Method based on LEFM

In the Method 2, crack initiation path is estimated by actually propagating a crack through LEFM concepts, Figure 5.4(a). In this case, consider a small crack increment of size Δa with orientation θ_i emanating from the contact trailing edge ($x = -a$). This problem can be solved through FE modelling in order to obtain crack's stress intensity factors (K_I and K_{II}) over time. Those, on the other hand, can be used to estimate the propagation direction of the next crack increment Δa. In this work, this process is undertaken up to the crack reaches the size of $2L$. Concerning the Method 2, two different cases are here investigated. In the Method 2-A, wear is neglected, i.e., crack propagation simulation is carried out considering the initial cylinder-on-flat contact configuration. In the Method 2-A, in its turn, crack propagation is performed by accounting surface changes due to wear in both fretting pad and fatigue specimen, Figure 5.4(b). In this setting, as in the Method 1-B, the shape of the worn geometries is obtained by simulating wear up to the number of cycles necessary to initiate a crack of length $2L$. It is noteworthy that in both cases the crack initiation point is the contact trailing edge ($x = -a$). In this work, the crack propagation increment, Δa, was set to 25 μm, whereas the initial propagation angle, θ_i, was set to 45°. A convergence analysis showed that 25 μm was an adequate size for the simulation, furthermore this length is almost ten times smaller than the final length of the crack. Such angle was chosen since this is the direction that maximizes shear stress amplitude at the contact trailing edge. In this case, one assumes that crack nucleation is governed by the formation of slip bands.

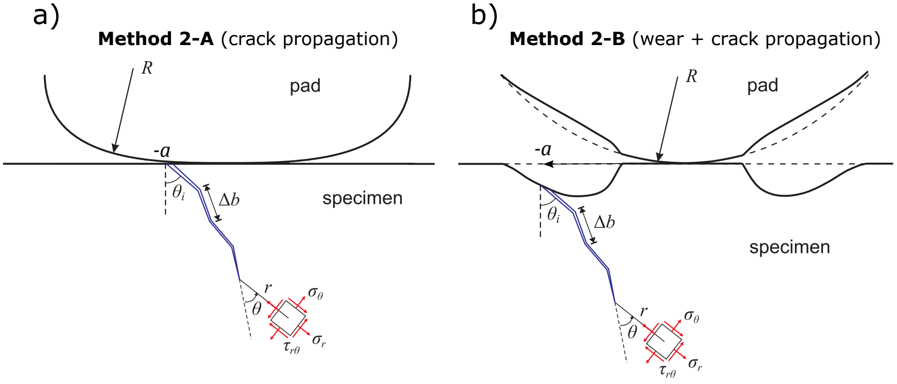
a)
Method 2-A (crack propagation)
R
pad
-a
specimen
θ_i
Δb
r
θ
σ_θ
σ_r
$\tau_{r\theta}$
b)
Method 2-B (wear + crack propagation)
R
pad
-a
specimen
θ_i
Δb
r
θ
σ_θ
σ_r
$\tau_{r\theta}$

Figure 5.4: Schematic representation of Method 2 at the contact trailing edge: (a) without wear and (b) with wear. Positive θ angles in the counterclockwise direction.

In order to obtain crack propagation direction, one maximizes the tangential strain range in accordance to the critical plane definition adopted in this work. In this case, the reconstruction of the stress components near the crack tip in terms of stress intensity factor are given by:

$$
\begin{aligned}
\sigma_r(r,\theta,t) = \frac{K_I(t)}{\sqrt{2\pi r}} & \left\{ cos\left(\frac{\theta}{2}\right) \left[1 + sin^2\left(\frac{\theta}{2}\right)\right]\right\} \\
+ \frac{K_{II}(t)}{\sqrt{2\pi r}} & \left\{ sin\left(\frac{\theta}{2}\right) \left[1 - 3sin^2\left(\frac{\theta}{2}\right)\right]\right\}
\end{aligned}
\tag{5.8}
$$

$$
\sigma_\theta(r,\theta,t) = \frac{K_I(t)}{\sqrt{2\pi r}} cos^3\left(\frac{\theta}{2}\right) - \frac{K_{II}(t)}{\sqrt{2\pi r}}\left[3sin\left(\frac{\theta}{2}\right)cos^2\left(\frac{\theta}{2}\right)\right]
\tag{5.9}
$$

where σ_r and σ_θ are the radial and tangential stress components according the reference system depicted in Figure 5.5. From plane strain assumptions, the tangential strain component over time is given by:

$$
\varepsilon_\theta(r,\theta,t) = \frac{\sigma_\theta}{E} - \frac{\nu}{E}\left[\sigma_r + \nu\left(\sigma_r + \sigma_\theta\right)\right]
\tag{5.10}
$$

Therefore, the expression for the tangential strain range in terms of θ becomes:

$$
\Delta\varepsilon(r,\theta) = \frac{1}{2}\left(\max_t \varepsilon_\theta(r,\theta,t) - \min_t \varepsilon_\theta(r,\theta,t)\right)
\tag{5.11}
$$

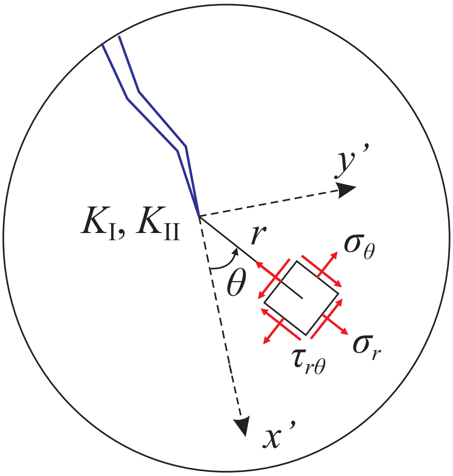

Figure 5.5: Schematic representation of stresses near the crack tip.

In this case, the direction θ of crack's next propagation increment is obtained by maximizing Eq. 5.11. Notice that the distance from the crack tip r in Eq. 5.8 to 5.11 does not influence the results.

5.2.3 Numerical model and boundary conditions

FE model considered in the present analysis is the same presented in Section 4.3.5. The difference lies in the element's size and the loads' application sequence. In the refined region, a structured mesh with linear quadrilateral elements is used with an approximate size of 28 μm. Loading conditions considered in the FE model are as follows: firstly, a mean bulk, B, is prescribed on the right side of the specimen while its bottom and left sides have their appropriate movement constraints. Secondly, a constant normal load, P, is applied on the upper surface of the pad. Finally, a tangential fully reversed load, Q, is prescribed on pad's upper surface ensuring partial slip conditions.

In the Method 2, it is necessary to model the crack and calculate the stress intensity factors (SIF's). In this case, the conventional FE model was used to model the crack and ABAQUS' interaction integral method, J-integral, was used to extract the individual SIF's, K_I and K_{II}. Contact interactions between the crack faces were also considered in the analyses, where the friction coefficient adopted for the crack faces was the same as the one observed in the fretting contact. Crack propagation analyses were performed by redefining crack's geometry and re-meshing the model for each crack propagation increment.

5.3 Results and discussions

Figure 5.6(a) depicts the worn contact profile for each experimental configuration presented in Table 3.17. In this case, wear simulations were performed up to the number of cycles necessary to initiate a crack of length $2L$ (226 μm). The wear modelling strategy is presented in Section 2.7. However, it is worth noticing that due the strong stress gradient found in contact problems, damage computations (Eq. 2.78) were considered only for points $L/2$ distant from the contact surface. In this case, the TCD by means of the point method helps dealing with the stress gradient effects.

As can be seen in Figure 5.6(a), wear is noticeably higher in the 30 mm pad radius tests. It happens once smaller contacts generate stronger stress decays. In other words, it takes more cycles to reach a critical damage inside the fatigue process zone. Larger contacts, on the other hand, present smother stress decays, favoring crack initiation. This behavior can be reaffirmed by looking at the estimated crack nucleation life, Table 5.1. As can be seen, the 30 mm pad radius tests (C4, C5 and C6) experienced longer crack initiation lives and consequently higher levels of wear compared with the 70 mm pad radius configurations. Figure 5.6(b) shows the contact pressure distribution by considering the worn surfaces for each test investigated in this work. As can be seen, contact pressure distribution for the 70 mm pad radius experiences only small changes while keeping its near Hertzian shape. Pressure distributions for the 30 mm pad radius, one the contrary, show a very strong variation with wear. In this case, contact tractions resemble the ones found in complete contacts.

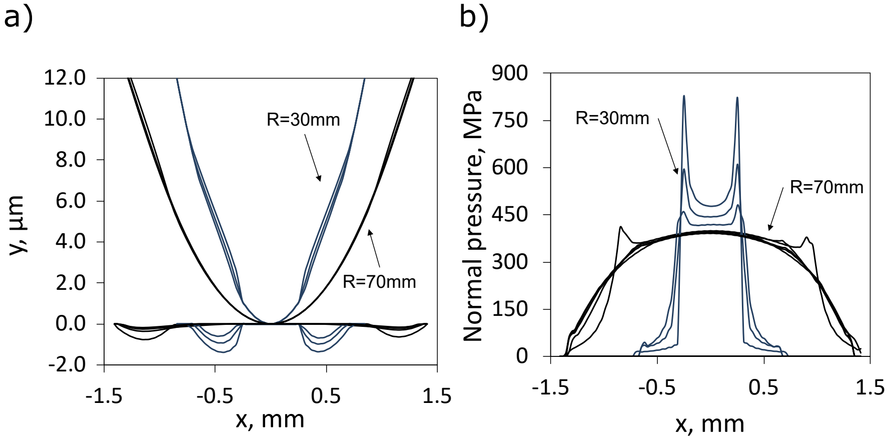

Figure 5.6: Wear results for each test configuration: (a) worn surface and (b) normal pressure distribution.

Table 5.1: Crack nucleation life prediction for tests C1-C8.

Load config.	**Crack nucleation life, N_i**
C1	182,000
C2	38,000
C3	13,000
C4	579,000
C5	354,000
C6	220,000
C7	26,000
C8	27,000

Figure 5.7 presents crack path estimates for the tests C2, C3 and C4. The solid black lines represent the experimental crack path. The dashed and dash-dotted red lines depict, respectively, results from Method 1-A and Method 1-B. The dash-x and dotted blue lines, on the other hand, present the results for Method 2-A and Method 2-B, respectively. Note that the crack paths obtained by Method 1 are very close to the experimental ones. It is also possible to see that the inclusion of wear (Method 1-B) had little effect on the results.

Considering Method 2, crack path estimates presented a deviation from the experimental observations. Besides, as in Method 1, wear does not seem to impact the crack path results. However, this deviation is not so pronounced when compared to other methods such as the maximum tangential stress criterion which cannot predict the crack propagation path under non-proportional loading conditions.

Table 5.2 presents the predicted crack initiation angles for all the methods investigated in this work. It also shows the measured experimental angles reported in [2]. It is worth noticing that the Method 2-A/B does not provide straight crack estimates. In this case, results displayed in Table 5.2 consider the straight line connecting the crack initiation site with its tip. A similar approach is considered for the experimental angles. Through the data presented in Table 5.2, it is noted that 93.75% of the results obtained with Method 1-A/B are within the experimental error margin, however, only 18.75% of the results obtained by Method 2-A/B are within the experimental scatter. Besides, these results reinforce that including wear in the analysis has little effect on the estimates, whether considering Method 1-A/B or Method 2-A/B.

Concerning the worst estimates provided by the Method 2, it seems that microstructural features and localized plasticity near the surface might not be fully neglected when simulating the propagation of very small cracks. However, the average stress/strain evaluations considered in the CDM approach seemed to properly capture the macro behavior of initiation cracks.

Table 5.2: Crack angle prediction for all tests using Methods 1 and 2.

Load config.	**Test**	**Exp. (°)**	**Average (°)**	**Method 1-A (°)**	**Method 1-B (°)**	**Method 2-A (°)**	**Method 2-B (°)**
C1	T1	12.8	21.4 +/- °12.2	27	24	10	14
	T2	30.0					
C2	T1	28.0	29.5 +/- °6.4	25	24	10	13
	T2	36.6					
	T3	24.0					
C3	T1	25.7	31.4 +/- °8.0	23	23	9	12
	T2	37.0					
C4	T1	29.7	25.9 +/- °5.4	35	30	20	9
	T2	22.0					
C5	T1	31.3	31.5 +/- °0.3	35	32	16	10
	T2	31.7					
C6	T1	36.3	30.4 +/- °8.4	35	33	15	11
	T2	24.4					
C7	T1	40.7	32.4 +/- °13.6	25	24	9	12
	T2	16.7					
	T3	39.7					
C8	T1	46.5	37.2 +/- °13.2	25	24	10	12
	T2	27.9					

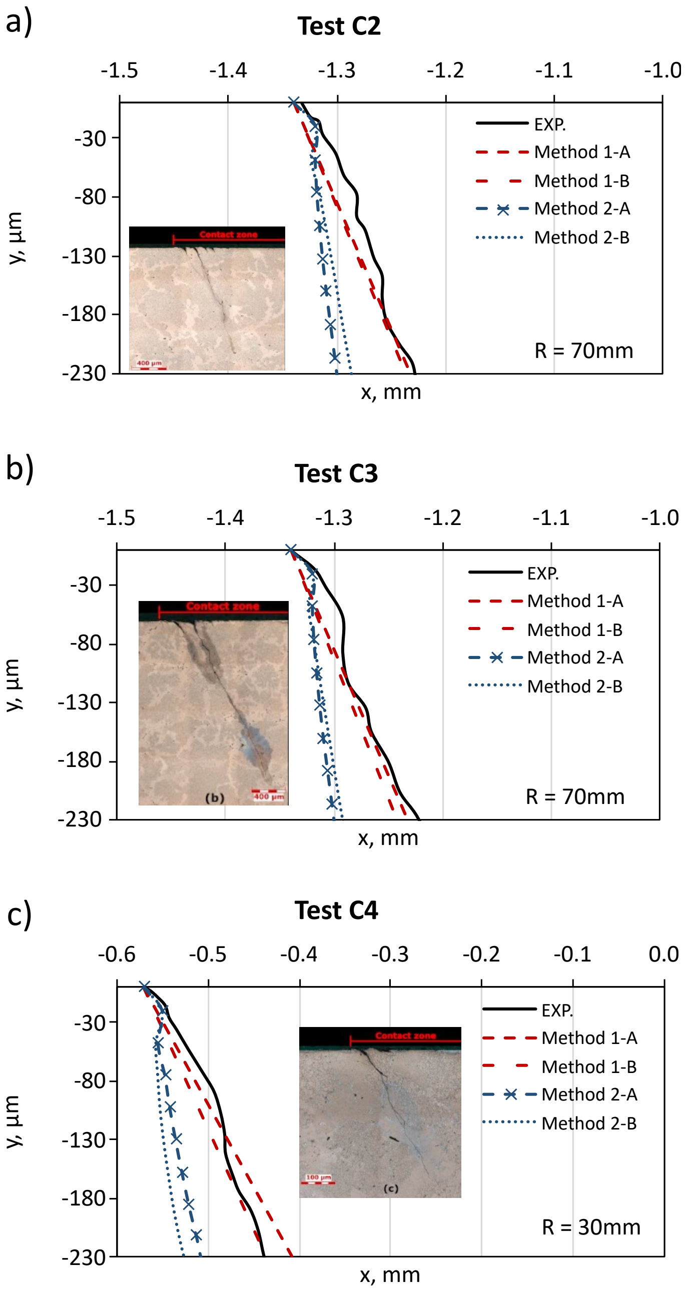

Figure 5.7: Crack angle prediction for tests C2 (a), C3 (b) and C4 (c).

Chapter 6

Fretting fatigue under variable amplitude loading considering partial slip regime: numerical analysis

"A robust numerical methodology for accessing component life under fretting fatigue conditions is presented in this chapter. This method is applied to fretting fatigue under variable amplitude load and validated with experimental results"

6.1 Overview

One of the main reasons for not having so many studies carried out with variable amplitude loading may have been the limitations of the testing equipment and fretting apparatus initially developed. Many of the fretting apparatuses did not allow the application of loads independently, so the few tests of variable amplitude available in the literature present results in which the bulk fatigue and fretting loads change the amplitude simultaneously. With the development of the fretting apparatus performed by Almeida et al. [1], the loading configuration possibilities increase significantly. As presented in Section 3.2.1, it is possible to independently control all the loads involved in the fretting tests (bulk, normal and tangential loads), and can also vary in-phase or out-of-phase, and they can also be applied in their waveforms synchronously or asynchronously.

Therefore, the main objectives of this doctoral thesis are to investigate the effects of the loading sequence on the life of components under fretting fatigue conditions and to propose a numerical methodology capable of estimating the life under these conditions. The experimental work was developed in Chapter 3, where the experimental set-up, the test procedure, and the experimental results are presented in detail. The tests were performed with constant normal load and constant amplitude of bulk fatigue load. Therefore, the only load applied with variable amplitude was the tangential load. Figure 3.21 illustrates the H-L and L-H load blocks that were applied. This chapter, therefore, is dedicated to the presentation of the numerical approach proposed to access the life of components subjected to fretting fatigue under variable amplitude loads. All numerical tools used here were developed and validated in previously published papers, and are presented in Chapters 4 and 5. In the next sections of this chapter, a summary of these tools will be presented, an analysis of the numerical results and a comparison with the experimental results will be presented.

6.2 Numerical methodology

This section systematically summarizes the application of the numerical tools developed in Chapters 4 and 5. The use of all these tools forms a single robust method that includes the main steps and phenomena involved in the fretting fatigue failure process. More specifically, the proposed approach separates the crack nucleation and propagation phases, in addition to estimating the crack initiation angle and computing the surface wear in the nucleation phase. Each of these steps and the numerical tools used is explained below.

6.2.1 Summary

The flowchart in Figure 6.1 summarizes the procedure to perform each step of the proposed numerical method. The steps can be divided into two. First, the crack nucleation life, N_i, and the worn contact profile are determined using Archard's law and L_M as presented in Section 2.7. In the second stage, the Critical Direction Method (CDM) is used to obtain the crack initiation angle, as presented in Section 5.2.1. The crack initiation point is assumed to be the contact trailing edge, $-a$. The crack is modelled and propagated until the fracture of the specimen. In this stage, the propagation life, N_p, and crack path are obtained. The sum of N_i and N_p is the total life to failure of the material, N_f.

As the flowchart shows, data such as specimen geometry, mesh discretization, material properties, contact conditions, and boundary conditions need to be provided in the pre-processing phase. Section 6.3 lists all material properties used in simulations and the calibration of multaxial fatigue parameter. In the first step (determination of N_i), the results from one fretting cycle simulation are used to compute material damage and surface wear. This process is repeated until the damage D_i is equal to 1. Remember that this verification is done at a distance L_M from the contact surface. At the end of the first stage, the nucleation life, N_i, and the final worn surface are obtained.

In the second step, considering the worn geometry, the CDM method is applied at the contact trailing edge (-a) to determine the initiation angle of a crack with a length equal to $2L$. Finally, a crack of length $2L$ and angle θ is modeled. The FE model will provide the stress/strain field near the crack used to apply SWT_L and determine the crack propagation angle. The factors K_I and K_{II} are also obtained, with which the propagation life can be calculated for an incremental crack size (in this case da=100μm). Finally, the total life to failure is obtained by adding the crack nucleation and propagation lifes.

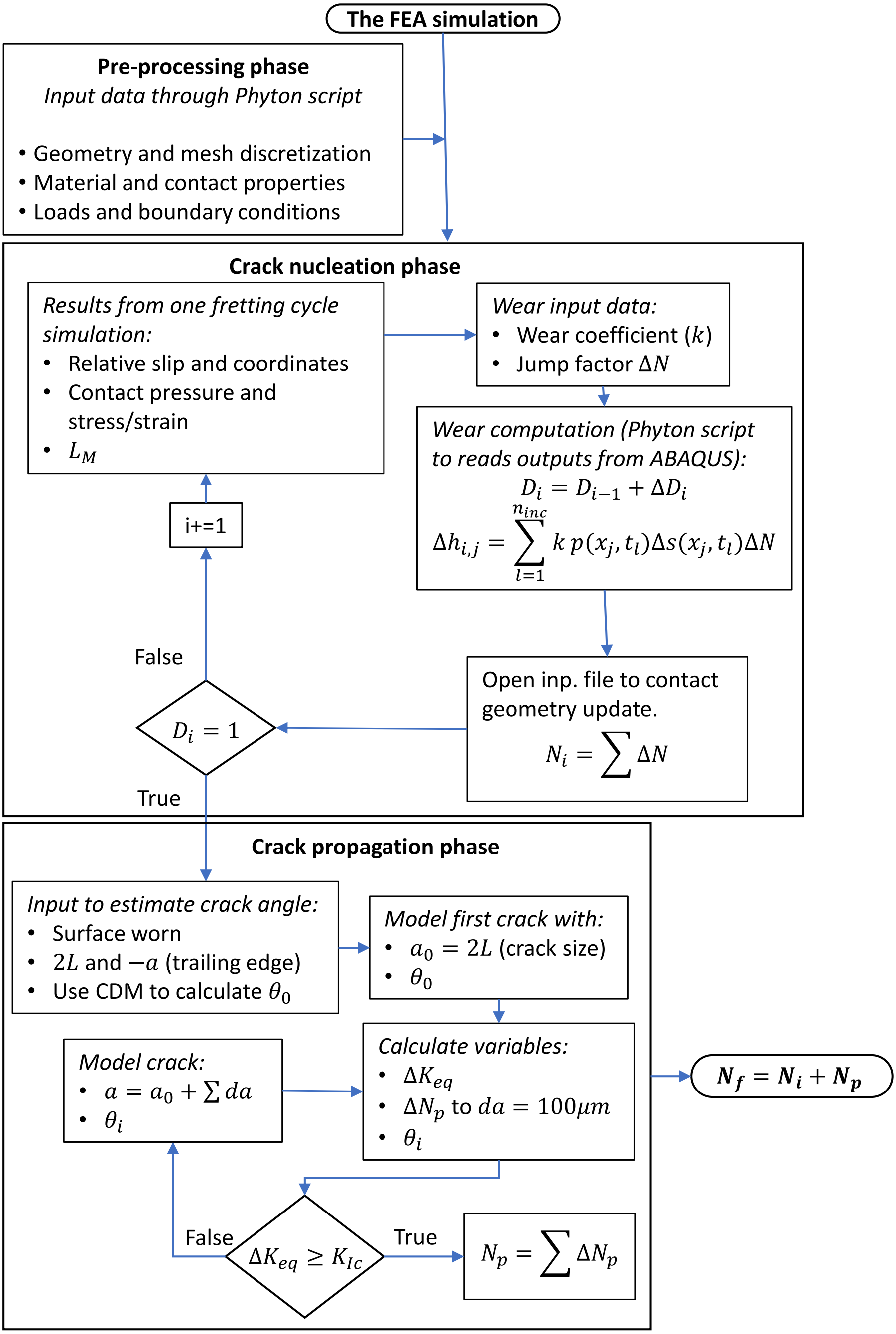
The FEA simulation
Pre-processing phase
Input data through Phyton script
• Geometry and mesh discretization
• Material and contact properties
• Loads and boundary conditions
Crack nucleation phase
Results from one fretting cycle simulation:
• Relative slip and coordinates
• Contact pressure and stress/strain
• L_M
Wear input data:
• Wear coefficient (k)
• Jump factor ΔN
Wear computation (Phyton script to reads outputs from ABAQUS):
$D_i = D_{i-1} + \Delta D_i$
$\Delta h_{i,j} = \sum_{l=1}^{n_{inc}} k\, p(x_j, t_l) \Delta s(x_j, t_l) \Delta N$
i+=1
False
$D_i = 1$
True
Open inp. file to contact geometry update.
$N_i = \sum \Delta N$
Crack propagation phase
Input to estimate crack angle:
• Surface worn
• $2L$ and $-a$ (trailing edge)
• Use CDM to calculate θ_0
Model first crack with:
• $a_0 = 2L$ (crack size)
• θ_0
Model crack:
• $a = a_0 + \sum da$
• θ_i
Calculate variables:
• ΔK_{eq}
• ΔN_p to $da = 100\mu m$
• θ_i
False
$\Delta K_{eq} \geq K_{Ic}$
True
$N_p = \sum \Delta N_p$
$N_f = N_i + N_p$

Figure 6.1: Flowchart of the numerical method proposed for estimating the life of components subjected to fretting fatigue.

6.2.2 Numerical model and boundary conditions

FE model considered in the present analysis is the same presented in Section 4.3.5. The difference lies in the element's size and the loads' application sequence. The structured mesh has linear quadrilateral elements with an approximate size of $L/2 = 9.75\mu$m. This means that it has a Gauss point at a distance of 4.87μm from the contact surface. Figure 6.2 demonstrates the load application sequence. As presented, firstly, the mean bulk fatigue load, B, is prescribed on the right side of the specimen while its bottom and left sides have their appropriate movement constraints. Secondly, the constant normal load, P, is applied on the upper surface of the pad. Finally, the tangential amplitude load, Q, is prescribed on pad's upper surface, and the amplitude of the bulk fatigue load is applied together. The ratio of tangential and fatigue loading is equal to R= -1 (fully reversed load).

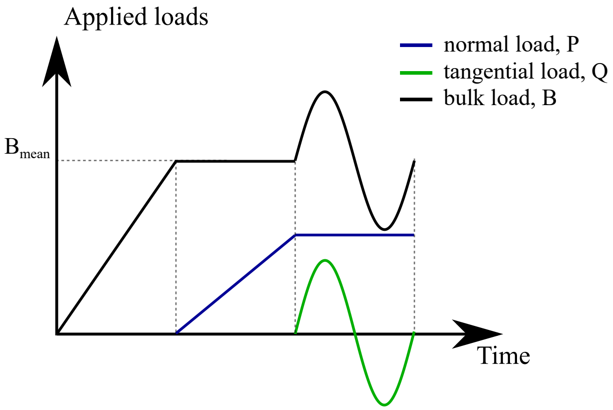

Figure 6.2: Schematic representation of the load application sequence.

The conventional FE model was used to model the crack and ABAQUS' interaction integral method, J-integral, was used to extract the individual SIFs, K_I and K_{II}. For the crack modeling, quadrilateral elements of the quarter point type are used, where the mid-node is positioned at a quarter distance from the crack tip. Contact interactions between the crack faces were also considered in the analyses, where the friction coefficient adopted for the crack faces was the same as the one observed in the fretting contact. Crack propagation analyzes were performed by redefining the crack's geometry and re-meshing the model for each crack propagation increment.

6.3 Materials and fatigue parameter calibration

The material used in this study is aluminum alloy 7075-T651. Table 6.1 summarizes all the mechanical properties necessary to carry out the wear and crack propagation simulations. The material properties that could not be obtained with the tests in Section 3.1 were found in the literature and are presented in Section 3.3. Fretting fatigue tests performed with H-L and L-H loading blocks are presented in Section 3.2. This section presents the fretting apparatus and the procedures for carrying out the tests.

Table 6.1: Al 7075-T651 properties.

Monotonic properties		
Young's modulus	E	68 GPa
Poisson's modulus	ν	0.33
Yield strength	S_y	506 MPa
Ultimate tensile strength	S_{ut}	570 MPa
Fracture toughness	K_{Ic}	26 MPa$\sqrt{m}$
Coefficient of friction	f	0.85
Wear coefficient	k_w	1.25× 10^{-8} mm^2/N
Critical distance static strength	L_s	662μm
Cyclic properties		
Threshold stress intensity factor	$\Delta K_{th_{0.1}}$	2.74 MPa$\sqrt{m}$
Fatigue limit range	$\Delta\sigma_{0.05}$	350 MPa
Paris' constant	C	$5.17 \times 10^{-7}(\frac{mm}{cycle} MPa\sqrt{m}^{m})$
Paris' constant	m	2.72
Critical distance for HCF	L	19.5μm

The S-N curve presented in Section 3.1 was obtained with tests to failure, so it had to be calibrated as shown in Figure 6.3. This procedure consists of calculating the propagation life N_p for each test of the S-N curve considering an initial crack size of $2L$. Then just subtract it to get the nucleation life N_i. Figure 6.4 presents the result of the calibration of the parameter SWT for total failure (a) and crack nucleation (b).

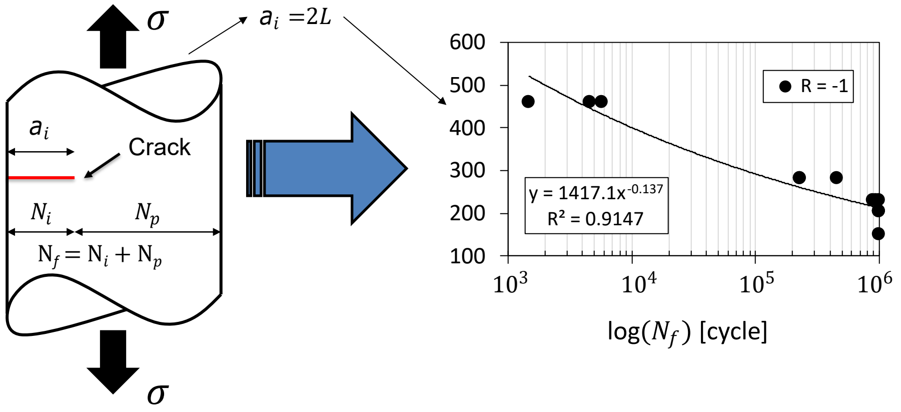

Figure 6.3: Process of calibration of uniaxial fatigue data for crack nucleation life: Al 7075-T651.

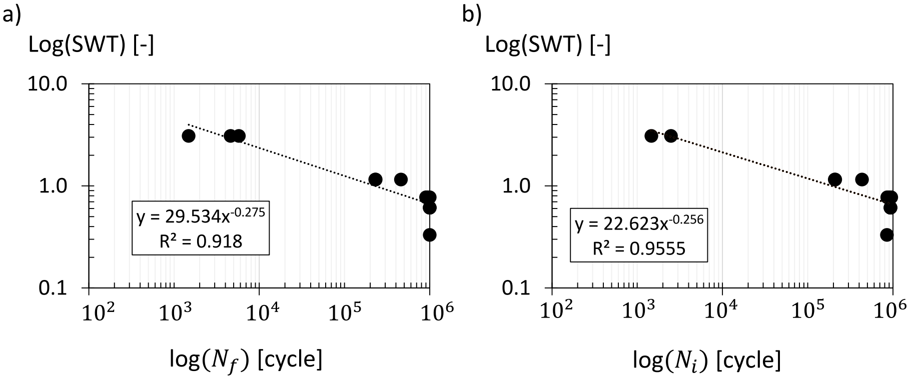

Figure 6.4: Uniaxial fatigue data for the Al 7075-T651 expressed in terms of the SWT parameter: total failure (a) and nucleation life (b).

6.4 Results and discussions

In this section, the results of the simulation of wear and crack propagation will be presented. However, first, a brief analysis of the use of critical distance as a function of life will be shown. Finally, the numerical results will be compared with the fretting fatigue under variable amplitude load tests (H-L and L-H loading blocks).

6.4.1 L in function of life: -a vs D_{max}

In Section 4.3.1 a way to apply the critical distance as a function of life together with the wear routine was proposed. In this first model, an initial value for life was defined, and with this value, the critical distance L_M was calculated. Then, at a L_M distance from the contact surface, the position (x coordinate) where the material damage was maximum (D_{max}) was sought. In this position, the stress/strain history was used to estimate the life, $N_{f,e}$, using a multiaxial fatigue model. If the estimated life was equal to the initial guess N the process was stopped, otherwise this recursive procedure was repeated until it found a value L_M that made the values $N_{f,e}$ and N converge.

However, as shown in Figure 6.5, when using this technique the size of L_M initially decreases, and at a certain moment, it starts to increase. This happens because at the beginning D_{max} is close to the trailing edge of the contact, -a, and in this region, the stress gradient tends to decrease with advancing wear, as shown in Figure 6.6. Therefore, L_M decreases in the first few cycles. However, the position where the D_{max} is located changes as the surface is worn down and the normal and shear stresses are redistributed on the contact surface. While at the edge of the contact there is a decrease in the stress gradient along the cycles, in the region where the transition of the stick and slip zone is found, there is an increase in the gradient due to the stress concentration in this region. This causes D_{max} to approach this region and at some point, the value of L_M starts to increase.

There are two problems with using this method. The first is very clear in Figure 6.5, which is the overestimation of life. When L_M is calculated in this way the crack nucleation life is much longer than when L_M is estimated using a fixed horizontal coordinate, such as the contact trailing edge, -a. The second error is in the principle of the physical phenomenon of failure. Most damage is accumulated in the first few cycles and on the edge of contact. And it is precisely at -a, or close to this value, that the first cracks appear and propagate. As the main objective of using TCD is to find effective stress for a given stress gradient, this gradient must be that observed in the region where the material

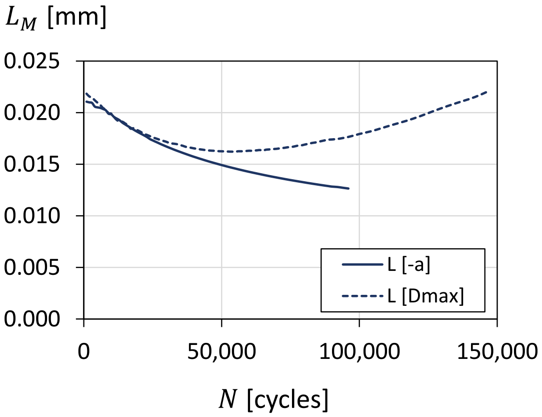

Figure 6.5: Variation of the critical distance along the cycles.

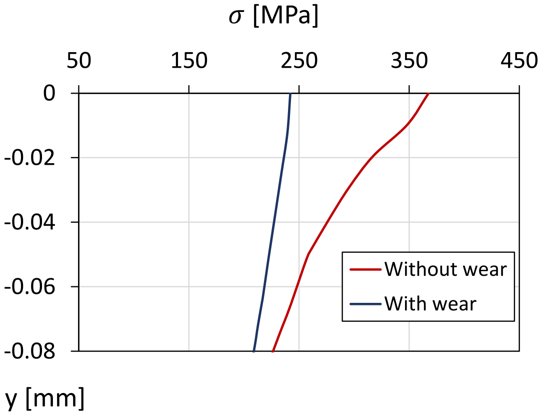

Figure 6.6: Stress gradient at the trailing edge of the contact, -a: distribution of σ_x inside of the material.

will fail. Therefore, in this chapter, L_M is estimated using a fixed x coordinate, more specifically in -a.

6.4.2 Life estimation: High and Low blocks

As mentioned before, two load blocks called High and Low blocks were defined. The only difference between them is the magnitude of the tangential load Q. Therefore, before estimating the life for the variable amplitude loads (H-L and L-H), it is necessary to estimate the life of both High and Low blocks separately.

The numerical method proposed in this chapter separates the life between the nucleation and crack propagation phases. The wear process is considered only in the crack nucleation phase. Figure 6.7(a) shows the profile of the specimen and pad before and after the wear process for the High block. The same can be seen in Figure 6.7(b) for the Low block. For both loading blocks, it is possible to clearly identify the stick and slip zones. The region where the material is removed is where the slip is observed. Since by Archard's law there is no material removal where there is no relative slip on the surface, the stick zone tends to remain intact until the end of the simulation. Note that the slip zone of the High block is slightly larger than that of the Low block. This happens because the tangential load is what causes the sliding between the surfaces, and the greater this slip, the greater the surface wear.

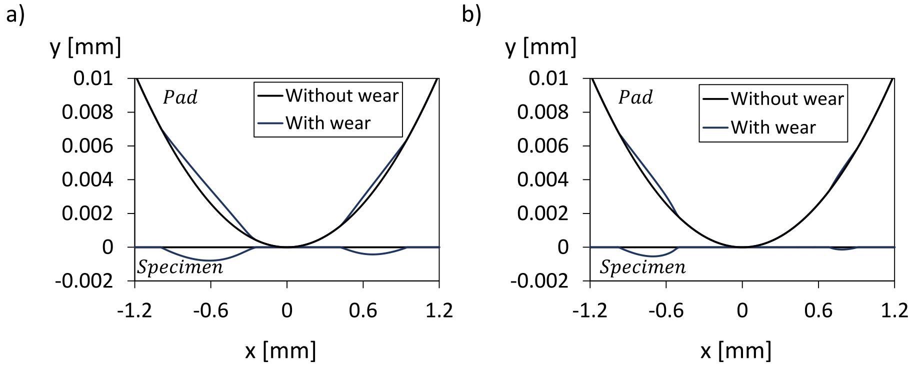

Figure 6.7: Pad and specimen profile before and after wear: High block (a) and Low block (b).

Figure 6.8(a) shows the profile of normal pressure and shear stress distribution before wear for the High block. Meanwhile, Figure 6.8(b), shows the same results for the final worn profile. Note that there is a decrease in the tensions in the slip zone, and despite the tendency to present a flatter profile, the discontinuity in the geometry due to the wear causes stress peaks to appear in the transitions between slip and stick zones. This redistribution of stresses causes the stress gradient to decrease at the edge of the contact (Figure 6.6), justifying the drop in the value of L_M.

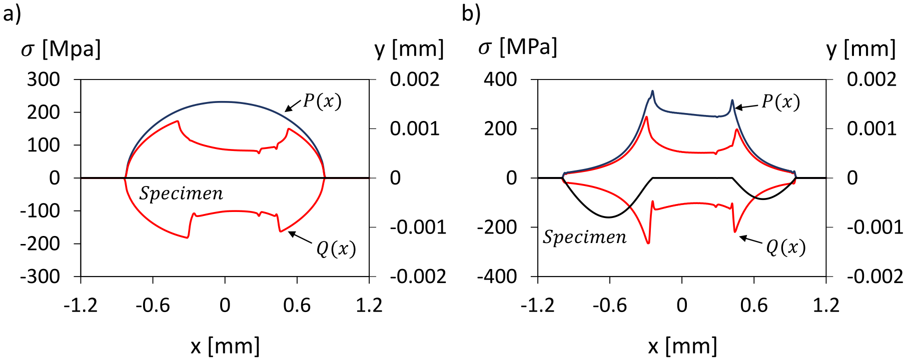

Figure 6.8: Stress distribution of High block: without wear (a) and with wear (b).

The crack initiation angle is estimated with the worn profile of both blocks. Table 6.2 summarizes the values of N_i and θ for the High and Low blocks. Remember that θ is estimated for an initial crack length of size $2L$. Note that the initial crack slope obtained numerically is almost the same as that observed experimentally, see Table 3.12. Figure 6.9(a) shows the crack propagation path for the two loading blocks. As can be seen, the numerically predicted paths are almost similar to those measured experimentally, in addition to showing the same propagation tendency for the contact central.

Table 6.2: Crack nucleation life and crack initiation angle estimated for blocks High and Low.

Load block	N_i **[cycles]**	θ_i [°]
High	96,000	11
Low	228,000	4

Figure 6.9(b) shows the propagation life, N_p, for the High and Low blocks. Note that the Low block's N_p is almost three times larger than that of the High block. This is due to the magnitude of the applied loads. The High block has a higher Q load, this makes the ΔK_{eq} higher than the Low block, as shown in Figure 6.10. Therefore, with higher ΔK_{eq}, a shorter life is observed.

In Table 6.3, the experimentally observed lifes for the tests of High and Low blocks are summarized, compared with the life obtained through the proposed

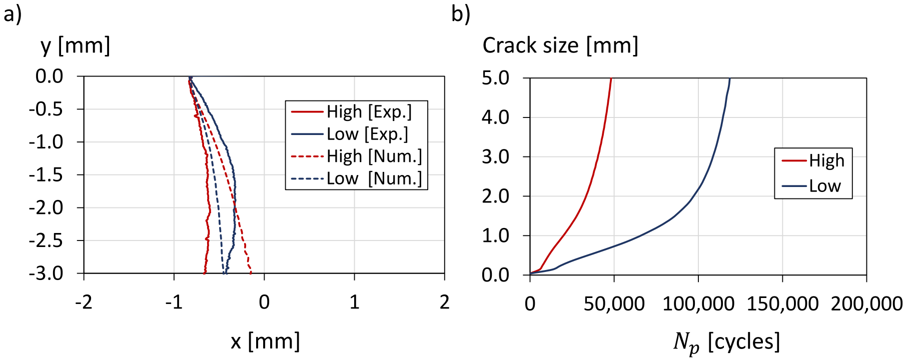

Figure 6.9: Crack propagation path (a) and life (b) prediction for High and Low blocks.

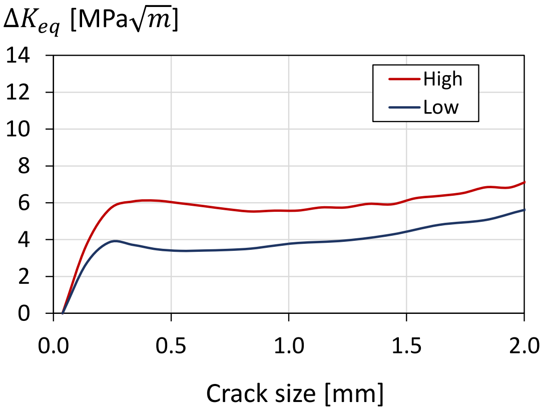

Figure 6.10: Evolution of ΔK_{eq} as the crack grows.

numerical method. Note that the proposed method has high accuracy for life estimation under conditions with constant amplitude loading, since comparing the numerical estimation with the experimental mean life the error is 1.06% for the High block and -0.05% for the Low block.

Table 6.3: Numerical life estimation for High and Low blocks.

Test.	**Load block**	$N_{f,exp}$ **[cycles]**	**Mean of** $N_{f,exp}$	$N_{i,num}$ **[cycles]**	$N_{p,num}$ **[cycles]**	$N_{f,num}$ **[cycles]**	**Error %**
FF1	High	122,037	143,281	96,000	48,800	144,800	1.06
FF2	High	146,178					
FF3	High	161,629					
FF4	Low	345,313	348,102	228,000	119,922	347,922	-0.05
FF5	Low	350,891					

6.4.3 Life estimation: H-L and L-H loading sequences

When analyzing the experimental results for the fretting fatigue under variable amplitude loading tests, it is possible to observe that there is a non-linear pattern in the experimental lifes, different from that expected when considering the use of Miner's linear damage rule. When considering Miner, as shown in Figure 3.24, the results would be within a scatter band of factor 1.5. For the numerical model proposed here, where the average error is less than 1%, the dispersion band would remain the same. However, for simpler life access techniques, the errors considering variable amplitude could be much higher.

Evaluating the experimental data presented in Section 3.2, it was possible to identify a relationship between the experimental life of each High and Low block separately and the damage generated by the first block, d_1, when applying the sequences of H-L and L-H loading. Thus, a new damage accumulation model was propose in order to consider the effect of the loading sequence:

$$D = \left(\frac{n_1}{N_1}\right)^{\beta} + \left(\frac{n_2}{N_2}\right) \tag{6.1}$$

where n_1 and n_2 are the number of cycles applied in the first and second blocks respectively. And N_1 and N_2 are the estimated lifes to failure for the loading configuration of the first and second block respectively. The β exponent can be determined as follows:

$$\beta = \left(\frac{N_h}{N_l}\right)^{\left(2.5\frac{n_1}{N_1}-1\right)} \tag{6.2}$$

where N_h and N_l are the estimated lifes of the High and Low blocks respectively. Figures 6.11(a) and (b) show the prediction of Eq. 6.1 for loading sequences H-L and L-H respectively. Note that for L-H loading the curve of the proposed damage model tends to be closer to Miner's rule. This is expected, since the L-H tests are the ones that are less influenced by the loading sequence.

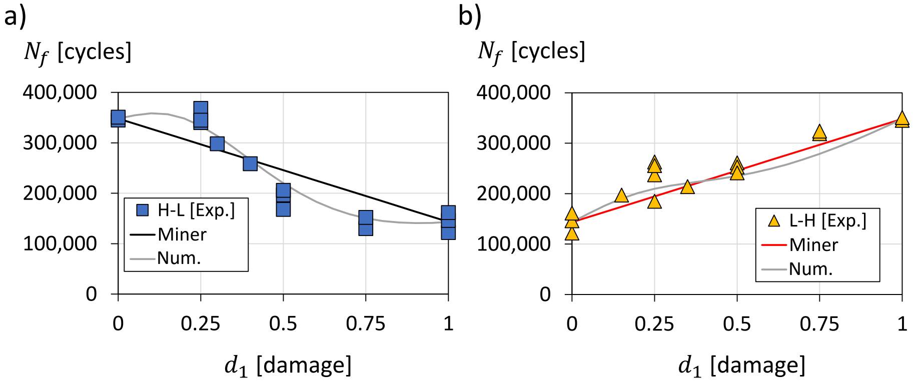

Figure 6.11: Expected results using the Numerical rule for sequences H-L (a) and L-H (b).

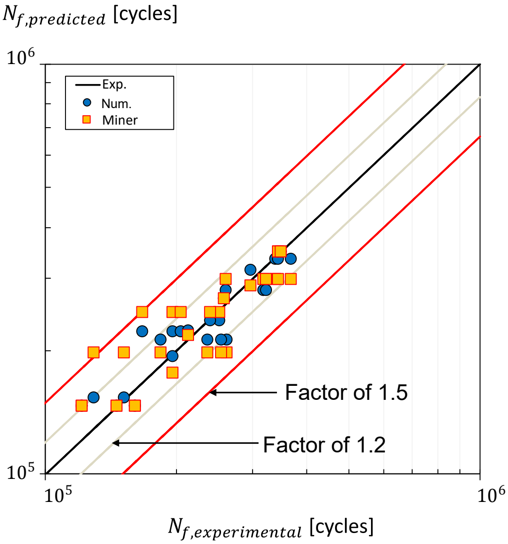

Figure 6.12: Estimated and observed fretting fatigue lives under variable amplitude loading condition: comparison between Miner's rule and Numerical damage model.

Figure 6.12 compares the results for life estimation of the H-L and L-H loading blocks when using the numerical damage model and Miner's rule. In Figure 6.12, the red squares are the data using Miner and the blue balls are the results when applying the numerical damage rule. Note that when applying Miner's rule the data are within a scatter band of factor 1.5, as expected. However, there is a significant improvement when applying the numerical model. In this case, most of the data falls within a scatter band of factor 1.2. That means the error is between 20% and -16%. Table 6.4 presents the experimental and numerical results for both damage models. Note that there is a reduction in the mean and standard deviation of life estimation error when using the numerical model.

Table 6.4: Numerical life estimation using Miner and Numerical damage rule compared with experimental results.

Test.	**Load seq.**	d_1	$N_{f,exp}$ **[cycles]**	$N_{f,Miner}$ **[cycles]**	$N_{f,Num.}$ **[cycles]**	**Miner error [%]**	**Num. rule error [%]**
FF1	High	1	122,037	144,800	144,800	18.65%	18.65%
FF2	High	1	146,178	144,800	144,800	-0.94%	-0.94%
FF3	High	1	161,629	144,800	144,800	-10.41%	-10.41%
FF4	Low	1	345,313	347,922	347,922	0.76%	0.76%
FF5	Low	1	350,891	347,922	347,922	-0.85%	-0.85%
FF6	H-L	0.8	130,014	195,581	152,109	50.43%	16.99%
FF7	H-L	0.8	152,217	195,581	152,109	28.49%	-0.07%
FF8	H-L	0.5	168,048	246,361	220,936	46.60%	31.47%
FF9	H-L	0.5	196,813	246,361	220,936	25.18%	12.26%
FF10	H-L	0.5	205,880	246,361	220,936	19.66%	7.31%
FF11	H-L	0.4	258,515	266,673	266,673	3.16%	3.16%
FF12	H-L	0.3	298,243	286,985	313,651	-3.77%	5.17%
FF13	H-L	0.3	368,431	297,142	333,412	-19.35%	-9.50%
FF14	H-L	0.3	340,000	297,142	333,412	-12.61%	-1.94%
FF15	H-L	0.3	344,765	297,142	333,412	-13.81%	-3.29%
FF16	L-H	0.8	318,965	297,142	279,049	-6.84%	-12.51%
FF17	L-H	0.8	323,986	297,142	279,049	-8.29%	-13.87%
FF18	L-H	0.5	261,076	246,361	235,779	-5.64%	-9.69%
FF19	L-H	0.5	253,089	246,361	235,779	-2.66%	-6.84%
FF20	L-H	0.5	241,193	246,361	235,779	2.14%	-2.24%
FF21	L-H	0.4	214,011	215,893	221,694	0.88%	3.59%
FF22	L-H	0.3	237,395	195,581	210,676	-17.61%	-11.26%
FF23	L-H	0.3	185,000	195,581	210,676	5.72%	13.88%
FF24	L-H	0.3	262,920	195,581	210,676	-25.61%	-19.87%
FF25	L-H	0.3	255,526	195,581	210,676	-23.46%	-17.55%
FF26	L-H	0.2	197,263	175,268	191,547	-11.15%	-2.90%
					Mean	1.49%	-0.40%
					Standard deviation	19.14%	11.79%

Chapter 7

Conclusions

"In this chapter, the methodologies used in this study and the main conclusions are summarized"

7.1 Overview

The fretting problem occurs when two bodies are in contact and there is a micro slip between them. In cases where one of the bodies is requested by a fatigue load (bulk fatigue load), there is the well-known fretting fatigue. The fatigue phenomenon is widely known and is present in a multitude of industrial applications. The introduction of fretting to the fatigue problem can further reduce the life of mechanical components, in view of a high stress gradient generated at the trailing edge of the contact.

As in any area of science, the first steps tend to be more timid and have simpler approaches. This would not be different from the studies on fretting fatigue. Therefore, the first tests always considered cyclic loads with constant amplitudes. However, it is well known that most industrial applications present complex loads with variable amplitudes over time. Currently, with the advancement of new technologies, it is possible to develop test apparatus capable of replicating this complexity in the laboratory. In the work carried out by Almeida et al. [1], a testing machine had its fretting apparatus modified, making it possible to apply loads independently and with variable amplitudes. The development of this equipment motivated this research.

Therefore, the main objective of this doctoral thesis is to investigate the effects of the loading sequence on the life of components under fretting fatigue conditions. By carrying out tests with H-L and L-H loading sequences (alternating the amplitude only of the tangential load) it would also be possible to verify the applicability of the linear damage accumulation rule known as Miner's rule. A second objective, no less important than the first, is the development of a robust numerical methodology capable of estimating the life of components subjected fretting fatigue under variable amplitude loading conditions.

In Chapter 1, this manuscript begins by presenting the fretting problem and a brief review of works carried out with variable amplitude loading. In the same chapter, the main objectives of the development of this research are also introduced. Soon after, in Chapter 2, a fundamental background was provided for understanding the main failure mechanisms involved in the fretting problem (multiaxial fatigue, mechanical contact and wear) and numerical tools used to develop the proposed numerical approach. All experimental work carried out in this doctorate is summarized in Chapter 3. It contains details about the equipment used in the tests, the results of the characterization of the 7075-T651 aluminum alloy, and mainly, the fretting fatigue under variable amplitude loading tests.

Some numerical works were developed and published even before all the experimental tests were carried out. This was done in order to validate techniques that would later be coupled to a single robust numerical method for accessing component life under frettig conditions. These works are presented in Chapters 4 and 5. Chapter 4 presents an approach where the crack nucleation and propagation life are obtained separately. In the nucleation phase, the effect of surface wear is computed and then, with the worn surface, a crack is introduced and propagated. In this work, a new approach to predict the crack path was also proposed, where the application of a critical plane model (SWT) is applied at a certain distance from the crack tip to determine the propagation angle. Finally, a study on the use of critical distance as a function of life is also carried out. In Chapter 5, a study was carried out on the effects of wear by applying two different methods to predict the crack nucleation angle in fretting problems.

Finally, in Chapter 6, all these tools are coupled in a single numerical approach. In this approach, wear is computed in the crack nucleation phase, and the critical distance as a function of life is used to check the accumulated material damage. Afterwards, the CDM is used considering a crack size of $2L$ to obtain the crack nucleation angle, which is then modeled and propagated. The sum of the nucleation and propagation lifes results in the total life to failure of the mechanical component. This chapter also introduces a new damage model (non-linear rule) that provides better results than Miner's rule to estimate the life of components subjected to loads with blocks of variable amplitude.

In the next sections, the conclusions obtained in each study carried out in this doctoral research will be presented in detail. Finally, suggestions for future numerical and experiments works are provided.

7.2 Effects of fretting wear process on fatigue crack propagation and life assessment

This research aimed to propose a numerical methodology to estimate the life of components subjected to fretting fatigue including the effects of surface wear and crack propagation. To calculate the wear, Archard's law was applied and the crack modeling was performed using the XFEM method. The conclusions are drawn as follows:

- Among the methods proposed to predict the crack trajectory, the SWT_{L_0} method stood out, obtaining a better crack trajectory than traditional methods like MTS, $K_{II} = 0$, and MERR.

- A comparative study between the parameters SWT and FS, without the presence of wear, showed that SWT presents more conservative results than FS for the material studied. Therefore, subsequent analyses including the wear effect were performed only with the SWT parameter.
- In terms of life assessment, the two simplest methodologies performed well for long lives, over 2×10^5 cycles. However, for short lives, the predictions were outside the scatter band 2. The proposed methodology including wear effect and crack propagation presented more conservative and accurate results than the other methods. All the results fell within the scatter band 2, with an error between 11% and -39%.
- It is important to note that, because of the wear effect inclusion, N_p had an average reduction of -28 %, in which all tests had a similar result. However, the tests with shorter lives (FF6 to FF9) had an average increase in N_i of 39 %, while the other tests (FF1 to FF5) showed an average reduction of -35.4 %. A similar result is seen when assessing total life.
- The analysis of the maximum friction energy dissipated during a fretting cycle showed that the wear effect was noticeably greater in tests with $E_d > 0.2\mu J/mm^2$. In these cases, this phenomenon plays a very important role in the failure mechanism of the material.
- In an attempt to generalize the results to the use of other alloys or loading configurations the Ruiz's parameter K_2 was normalized by the pressure. This way all the main loads that influence the fretting fatigue problem are included in the analysis. Therefore, it can be said that for an energy dissipation greater than $0.04\mu J/mm^2$ it is important to include the effects of wear.

This research also investigates the influence of using the critical distance, L, constant or dependent on life. The conclusions about this topic are drawn as follows:

- The methodology to compute the wear, Section 2.7, provided results consistent with the expected, where the wear profile clearly shows the separation between the slip and stick zones. It is also possible to observe that the tests with higher loads and consequently shorter lives are also those that had the most worn contact surface (FF6-FF9 tests).
- The crack path predicted with the methodology proposed in Section 2.3.5 provided results close to that observed experimentally. It was also possible to observe that the inclusion of the wear effect did not change the crack path, however, the propagation life was reduced.

- In terms of life access, in the constant L approach, only method 3 provides a life prediction within a scatter band of 2, Figure 4.29(a). The inclusion of the wear effect increases the accuracy of the life estimation, however, this improvement is more significant only in tests with short lives as they present greater energy dissipation on the surface, which therefore increases the wear effect (FF6-FF9 tests).
- On the other hand, when using $L = A(N)^B$, from the simplest one to the most robust method presented results within a scatter band of 2, Figure 4.29(b). Although method 3 has a very low mean of errors and a lower standard deviation than the other methods, Table 4.4, its computational cost is very high. Thus, the simplest method becomes the most viable since the tests are in a partial slip regime and medium or high cycling fatigue.

7.3 Early crack orientation prediction methods under fretting fatigue loading including wear effects

This paper investigates two different approaches, namely Method 1 and Method 2, to predict crack initiation direction in fretting problems subjected to partial slip conditions. In addition, the influence of including surface wear in the analysis was investigated for both methods. Experimental data from fretting tests conducted on an AA7050- T7451 alloy [2] were used for validation. In this setting, the following conclusions could be drawn:

- Method 1, which is based on the CDM in conjunction with SWT's fatigue model, provided crack initiation angle estimates in good accordance with the experimental observations. Besides, for this method, the inclusion of wear in the analyses (Method 1-B) led to nearly the same results as when wear is disregarded (Method 1-A).
- On the other hand, Method 2 proved to be less accurate in predicting crack initiation angle either with (Method 2-B) or without (Method 2-A) the inclusion of wear in the analysis. Almost all the predicted angles by this method were out of the experimental margin of error. In addition, the inclusion of wear had little effect on the estimates.
- Furthermore, it is worth mentioning that besides providing better crack initiation direction estimates, Method 1 is considerably easier to implement

and presents a very small computational cost compared to Method 2, which involves crack propagation simulation.

- Last but not least, the inclusion of wear in the analysis significantly increases computational costs while not showing any appreciable improvement in the crack initiation angle estimates. Therefore, at least for partial slip conditions and for the material here investigated, there is no need to include wear in the analyses.

7.4 Fretting fatigue under variable amplitude loading considering partial slip regime: Experimental and numerical analysis

Chapters 3 and 6 present respectively the experimental and numerical results of the study carried out on fretting fatigue under variable amplitude loading. Tests were performed with two blocks of loads (H-L and LH), where only the amplitude of the shear load is changed in each block. The normal load and the bulk fatigue load amplitude remain constant. A numerical method for life estimation and a new damage model were also proposed through these studies. In this setting, the following conclusions could be drawn:

- In the Chapter 3, several experimental tests were carried out in order to characterize the material under study. The results found are in agreement with the values in the literature. In this way, it can be said that the characterization of aluminum alloy 7075-T651 was successful.

- Fretting fatigue tests with the H-L loading sequence will show a greater sensitivity to the effect of the loading sequence than the L-H tests. For the H-L loading sequence, Figure 3.23(a), if the damage generated in the first loading block (High block) is d_1<0.3, Miner's rule is more conservative. Nonetheless, when d_1>0.3 is observed a reduction in the life if compared with the expected life by Miner's rule.

- Despite the existence of the loading effect (especially for the H-L sequence), it does not means that Miner's rule can not be used. Considering the mean experimental life of the High and Low blocks of 143,281 and 348,102 cycles respectively (Table 3.8), Figure 3.24 shows that the data are all within a scatter band of factor 1.5. In other words, Miner's rule provides estimates with a margin of error between 50% and -33%.

- The proposed numerical method for life estimation is divided between the nucleation and crack propagation phases. In the nucleation phase wear is considered and maximum damage is computed at a critical distance from the surface, L_M. An initial analysis showed that, physically, the correct way to estimate L_M is considering a fixed horizontal coordinate (near the trailing edge of the contact). Thus, L_M tends to decrease over the cycles due to surface wear and stress gradient variation.

- Table 6.2 shows the crack nucleation life and initiation angles for the High and Low blocks separately. Note that the values obtained for the angles are very close to those observed experimentally, as shown in Table 3.12. As expected, the nucleation life N_i for the High block is shorter than for the Low block, however, the surface wear is higher. This is because the load Q (responsible for the fretting process) is higher in the High block.

- The numerical results for the propagation phase are quite consistent. Likewise, the propagation life, N_p, is longer for the Low block and shorter for the High. This is because the High block has a higher initial ΔK_{eq} than the Low block. The crack path obtained was close to that observed experimentally and with a tendency of growth towards the center of the contact.

- In terms of life acessement, the proposed method presents excellent results. The error in estimating the life of both blocks (High and Low) has an error (compared to the mean experimental life) of 1.06% and -0.05% for the High and Low blocks respectively, Table 6.3.

- A new damage model that considers the effect of the loading sequence was proposed, Equation 6.1. When comparing the proposed damage model with the results obtained with Miner's rule (linear), it is possible to identify a significant improvement in the estimated life for blocks H-L and L-H, Figure 6.12. While Miner's rule gives results within a scatter band of 1.5, the Numerical damage model provides estimates of lives in a scatter band of 1.2 (errors between 20% and -16%).

- Table 6.4 shows the experimental and numerical results using Miner and the Numerical damage rule. For cases where the amplitude is constant (FF1-FF5 tests), the estimates are the same, however, the differences are quite expressive in some cases with H-L and L-H blocks. In general, the mean error and standard deviation show a reduction when applying the Numerical damage model. The mean error decreased from 1.49% to -0.4%, and the standard deviation from 19.14% to 11.79%.

7.5 Future work

7.5.1 Numerical modelling

The proposed numerical model separates the total life into two phases (crack nucleation and propagation), where the surface wear is computed in the crack nucleation phase. The wear model uses Archard's equation and, as in almost all models available in the literature, multiplies the wear computed in each simulation step by a jump factor, ΔN. In this way, it is considered that the profile of the stress distribution on the contact surface remains constant throughout ΔN cycles. This procedure is adequate and somehow reduces the simulation time, reducing the computational cost. However, for more severe loading configurations or even for materials with high wear coefficient, the value of ΔN needs to be somewhere between 100 and 2,000 cycles only. Otherwise, wear will produce surface discontinuities that increase stress peaks (especially at the contact trailing edges) making it difficult for the FE model to converge. Therefore, future works could develop an algorithm for smoothing the contact surfaces to make it possible to use ΔN above 10,000 or 20,000 cycles, drastically reducing the computational cost of wear simulations.

In the crack propagation phase, it is necessary to define the point of its initiation. In validating the CDM model, the effect of surface wear on the initiation angle estimation was investigated. However, the influence of the choice of crack nucleation point was not verified. Therefore, the next works can study what would be the results of applying the CDM model considering different positions for crack initiation. Criteria to define this position could be the coordinate where the surface damage or dissipation energy is maximum, in addition to the most common approach in the literature, which is the contact trailing edge. By doing so, it will be possible to verify not only if there is an influence on the estimation of the nucleation angle but also the path and crack propagation life.

7.5.2 Experimental

In this doctorate, fretting fatigue under variable amplitude loading tests was performed. However, the tests were performed considering only two loading blocks, that is, the amplitude is modified during the test only once. In addition, the normal load and the bulk fatigue load amplitude were kept constant in all tests.

With only two loading blocks (H-L and L-H) it was possible to observe an effect on the experimental life due to the load application sequence, mainly for the blocks of the H-L sequence. Based on these results, a new damage model was proposed to estimate lives. However, since the L-H sequence was less affected by the loading sequence, it is necessary to carry out more tests with three or four loading blocks to verify the applicability of the proposed damage model. As the number of loading blocks increases, the influence of the High block on total life may decrease.

As mentioned, the tests were performed keeping the normal load and the bulk fatigue load amplitude constant. To reinforce the validation of the proposed damage model, it is also suggested to carry out tests similar to those that were performed, but changing the amplitude of normal and bulk fatigue loads. These tests can be done by changing the amplitude of just one of the loads or even combining two or three loads to change simultaneously.

Appendix A

Technical drawing of specimens

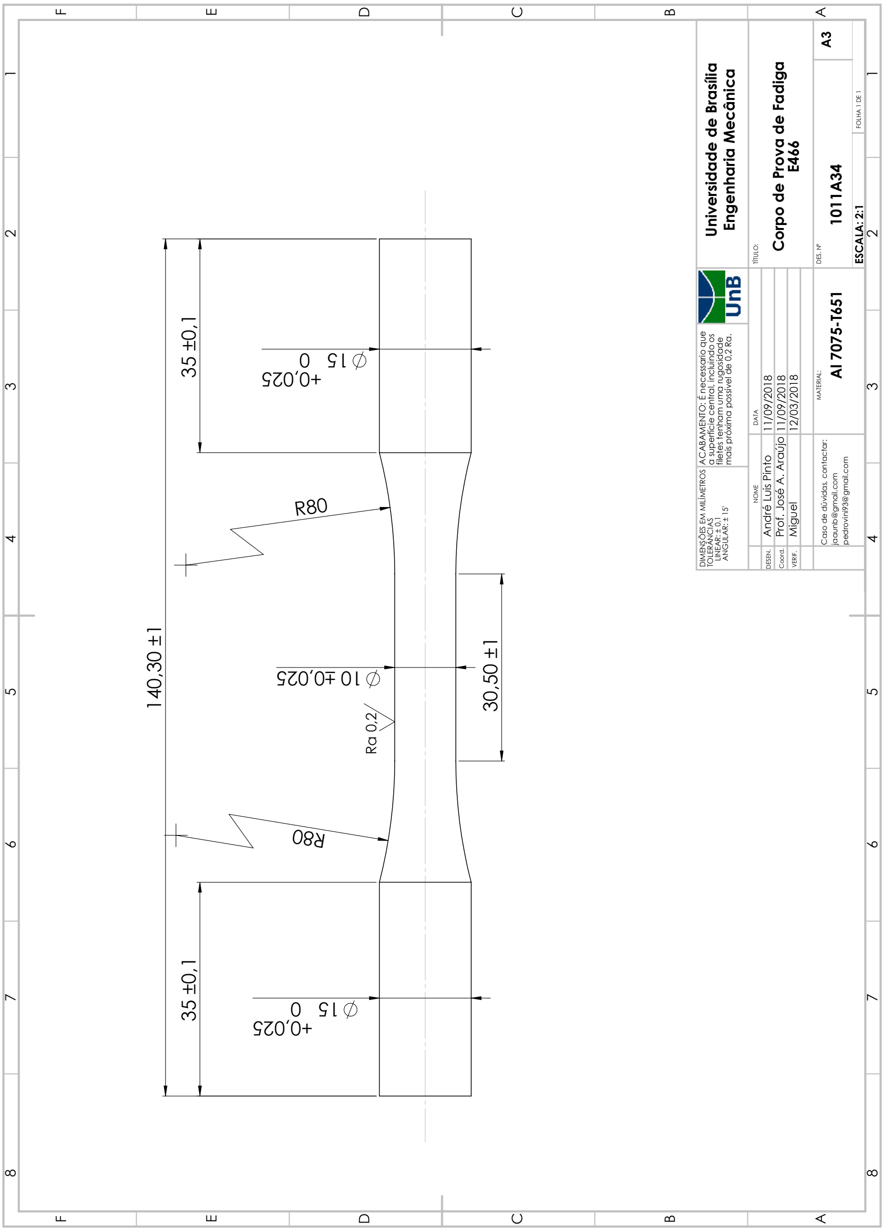
Universidade de Brasília
Engenharia Mecânica
TÍTULO:
Corpo de Prova de Fadiga
E466
DES. Nº
1011A34
A3
ESCALA: 2:1
FOLHA 1 DE 1
MATERIAL:
Al 7075-T651
DIMENSÕES EM MILÍMETROS
TOLERÂNCIAS
LINEAR: ± 0,1
ANGULAR: ± 15'
ACABAMENTO: É necessário que a superfície central incluindo os filetes tenham uma rugosidade mais próxima possível de 0.2 Ra.
UnB
NOME
DATA
DESEN.
André Luís Pinto
11/09/2018
Coord.
Prof. José A. Araújo
11/09/2018
VERIF.
Miguel
12/03/2018
Caso de dúvidas, contactar:
jaaunb@gmail.com
pedrovin93@gmail.com
35 ±0,1
∅ 15 0 +0,025
R80
140,30 ±1
∅ 10 ±0,025
Ra 0,2
30,50 ±1
R80
35 ±0,1
∅ 15 0 +0,025
A
B
C
D
E
F
1
2
3
4
5
6
7
8

Figure A.1: Technical drawing of fatigue specimen.

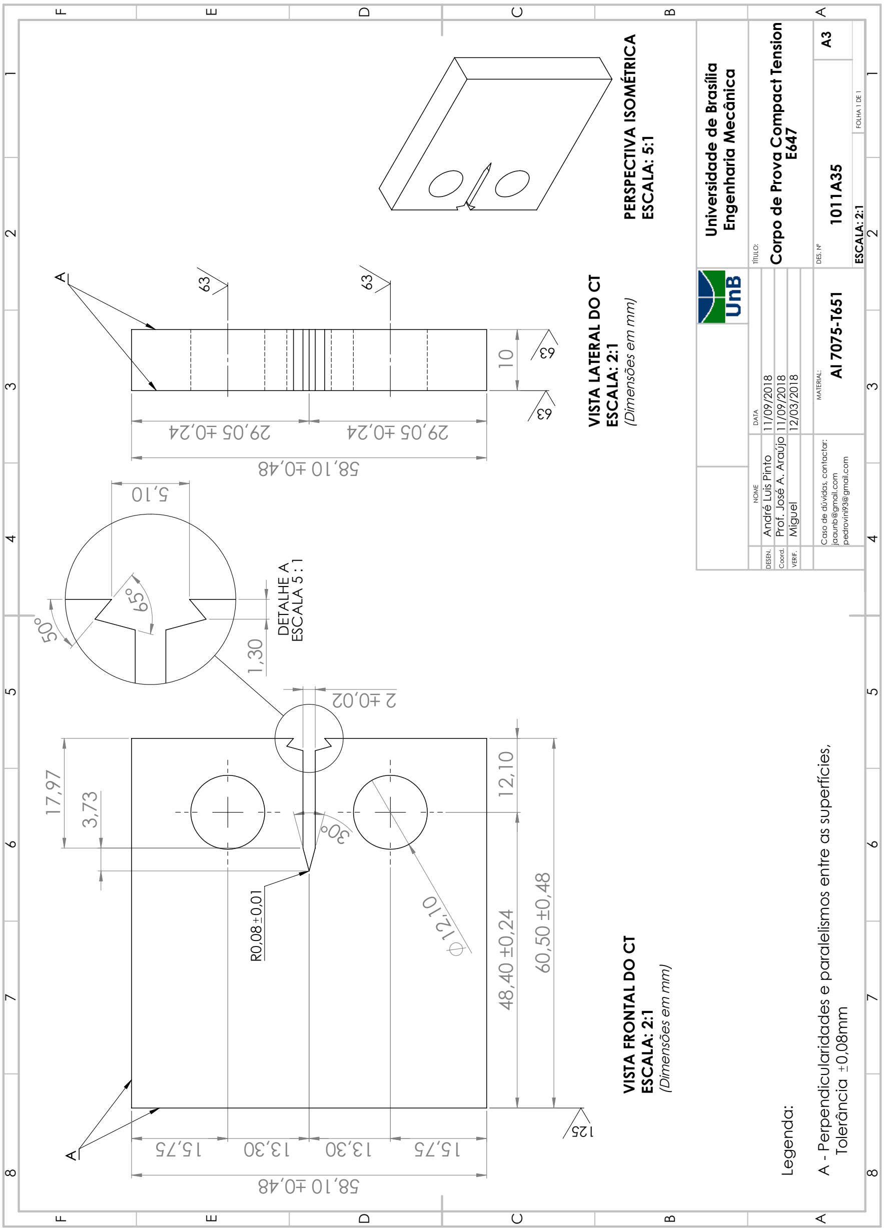
VISTA FRONTAL DO CT
ESCALA: 2:1
(Dimensões em mm)
VISTA LATERAL DO CT
ESCALA: 2:1
(Dimensões em mm)
PERSPECTIVA ISOMÉTRICA
ESCALA: 5:1
DETALHE A
ESCALA 5 : 1
58,10 ±0,48
15,75
13,30
13,30
15,75
17,97
3,73
R0,08±0,01
30°
ϕ12,10
12,10
48,40 ±0,24
60,50 ±0,48
2 ±0,02
1,30
5,10
50°
65°
29,05 ±0,24
29,05 ±0,24
58,10 ±0,48
10
63
63
63
63
125
A
A
A
Legenda:
A - Perpendicularidades e paralelismos entre as superfícies,
Tolerância ±0,08mm
Universidade de Brasília
Engenharia Mecânica
UnB
TÍTULO:
Corpo de Prova Compact Tension
E647
NOME
DATA
DESEN.
André Luís Pinto
11/09/2018
Coord.
Prof. José A. Araújo
11/09/2018
VERIF.
Miguel
12/03/2018
Caso de dúvidas, contactar:
jaaunb@gmail.com
pedrovin93@gmail.com
MATERIAL:
Al 7075-T651
DES. Nº
1011A35
A3
ESCALA: 2:1
FOLHA 1 DE 1
F
E
D
C
B
A
1
2
3
4
5
6
7
8

Figure A.2: Technical drawing of compact tension specimen.

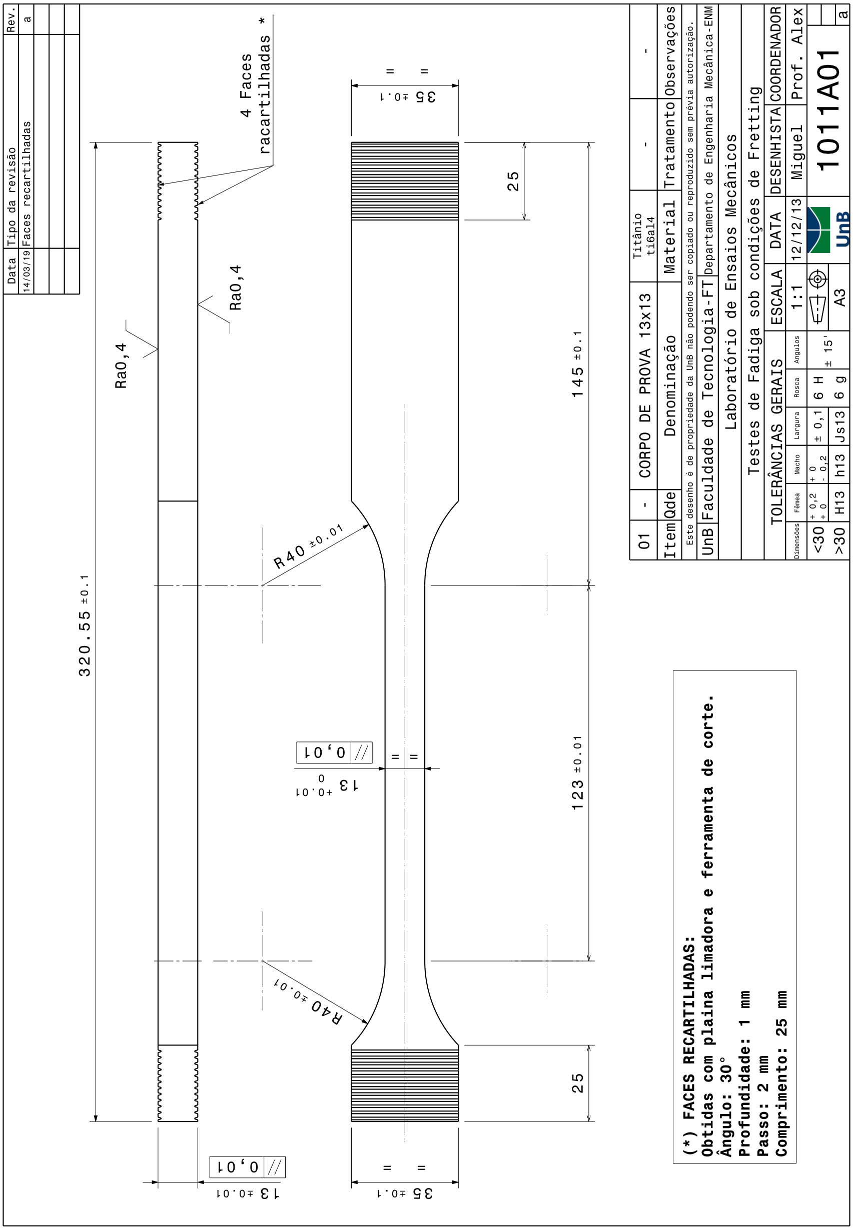
Data
Tipo da revisão
Rev.
14/03/19
Faces recartilhadas
a
4 Faces racartilhadas *
Ra0,4
Ra0,4
320.55 ±0.1
35 ±0.1
25
145 ±0.1
R40 ±0.01
R40 ±0.01
13 +0.01 0
0,01
123 ±0.01
25
13 ±0.01
0,01
35 ±0.1
01
-
CORPO DE PROVA 13x13
Titânio ti6al4
-
-
Item
Qde
Denominação
Material
Tratamento
Observações
Este desenho é de propriedade da UnB não podendo ser copiado ou reproduzido sem prévia autorização.
UnB
Faculdade de Tecnologia-FT
Departamento de Engenharia Mecânica-ENM
Laboratório de Ensaios Mecânicos
Testes de Fadiga sob condições de Fretting
TOLERÂNCIAS GERAIS
ESCALA
DATA
DESENHISTA
COORDENADOR
Dimensões
Fêmea
Macho
Largura
Rosca
Angulos
1:1
12/12/13
Miguel
Prof. Alex
<30
+ 0,2 + 0
+ 0 - 0,2
± 0,1
6 H
± 15'
>30
H13
h13
Js13
6 g
A3
UnB
1011A01
a

(*) FACES RECARTILHADAS:
Obtidas com plaina limadora e ferramenta de corte.
Ângulo: 30°
Profundidade: 1 mm
Passo: 2 mm
Comprimento: 25 mm

Figure A.3: Technical drawing of fretting fatigue specimen.

Data	Tipo da revisão	Rev.
31/03/15	Nova tolerância R70 + Nova rugosidade	a

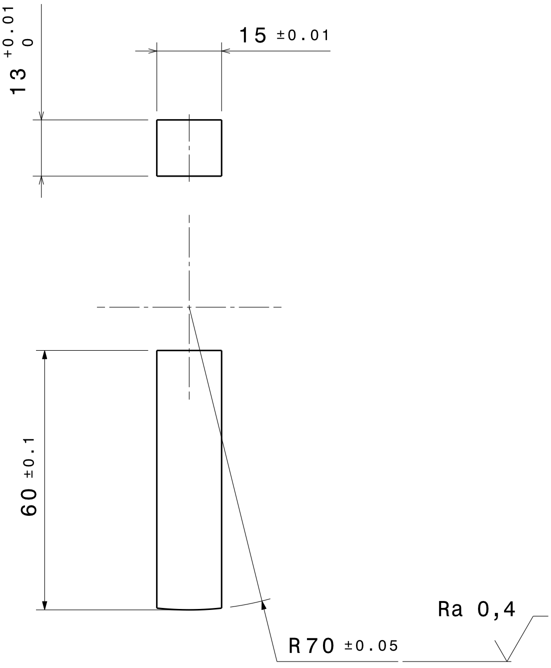

14	-	SAPATA 13x15 R70	Alumínio 7050	-	-
Item	Qde	Denominação	Material	Tratamento	Observações

Este desenho é de propriedade da UnB não podendo ser copiado ou reproduzido sem prévia autorização.

UnB	Faculdade de Tecnologia-FT	Departamento de Engenharia Mecânica-ENM

Laboratório de Ensaios Mecânicos

Testes de Fadiga sob condições de Fretting

TOLERÂNCIAS GERAIS						ESCALA	DATA	DESENHADOR	COORDENADOR
Dimensões	Fêmea	Macho	Largura	Rosca	Angulos	1:1	02/07/14	Miguel	Prof. Alex
<30	+ 0,2 + 0	+ 0 - 0,2	± 0,1	6 H	± 15'		UnB	1011B14	
>30	H13	h13	Js13	6 g		A4			a

Figure A.4: Technical drawing of pad used in fretting fatigue test.

Bibliography

[1] Almeida, G., Cardoso, R., Garcia, M., Chassaing, G., Pommier, S., and Araújo, J. Four actuators fretting fatigue rig and tests with cyclic normal load for ti-6al-4v. *Theoretical and Applied Fracture Mechanics 119* (2022), 103292.

[2] Almeida, G., Pessoa, G., Cardoso, R., Castro, F., and Araújo, J. Investigation of crack initiation path in aa7050-t7451 under fretting conditions. *Tribology International 144* (2020), 106103.

[3] Almeida, G. M. J. Ensaios e avaliação da direção de iniciação de trinca sob condições de fretting.

[4] Anderson, T. L. *Fracture mechanics: fundamentals and applications.* CRC press, 2017.

[5] Araújo, J., Castro, F., Matos, I., and Cardoso, R. Life prediction in multiaxial high cycle fretting fatigue. *International Journal of Fatigue 134* (2020), 105504.

[6] Araújo, J., and Nowell, D. Analysis of pad size effects in fretting fatigue using short crack arrest methodologies. *International Journal of Fatigue 21*, 9 (1999), 947–956.

[7] Araujo, J., and Nowell, D. The effect of rapidly varying contact stress fields on fretting fatigue. *International Journal of Fatigue 24*, 7 (2002), 763–775.

[8] Araújo, J., and Nowell, D. Mixed high low fretting fatigue of ti6al4v: Tests and modelling. *Tribology international 42*, 9 (2009), 1276–1285.

[9] Araújo, J., Susmel, L., Pires, M., and Castro, F. A multiaxial stress-based critical distance methodology to estimate fretting fatigue life. *Tribology International 108* (2017), 2–6.

[10] Araújo, J., Susmel, L., Taylor, D., Ferro, J., and Mamiya, E. On the use of the theory of critical distances and the modified wöhler curve method to estimate fretting fatigue strength of cylindrical contacts. *International Journal of Fatigue 29*, 1 (2007), 95–107.

[11] Araújo, J. A., Almeida, G., Ferreira, J., da Silva, C., and Castro, F. Early cracking orientation under high stress gradients: The fretting case. *International Journal of Fatigue 100* (2017), 611–618.

[12] Archard, J. Contact and rubbing of flat surfaces. *Journal of applied physics 24*, 8 (1953), 981–988.

[13] Ashwin, A., Lakshman, R. H., Swaroop, C. C., Vignesh, M., Vignesh, R. V., and Padmanaban, R. Predicting the wear rate of aluminum alloy aa2024-t351 using hybrid linear function and radial basis function. In *IOP Conference Series: Materials Science and Engineering* (2019), vol. 561, IOP Publishing, p. 012046.

[14] ASTM. Astm e407-07 (2015) e1, standard practice for microetching metals and alloys, 1999.

[15] Azevedo, C., Henriques, A., Pulino Filho, A., Ferreira, J., and Araújo, J. Fretting fatigue in overhead conductors: Rig design and failure analysis of a grosbeak aluminium cable steel reinforced conductor. *Engineering Failure Analysis 16*, 1 (2009), 136–151.

[16] Baietto, M.-C., Pierres, E., Gravouil, A., Berthel, B., Fouvry, S., and Trolle, B. Fretting fatigue crack growth simulation based on a combined experimental and xfem strategy. *International Journal of Fatigue 47* (2013), 31–43.

[17] BARBOSA, L. d. M. Influência da taxa de aquecimento no tratamento térmico de solubilização da liga al 7075.

[18] Barsoum, R. S. On the use of isoparametric finite elements in linear fracture mechanics. *International journal for numerical methods in engineering 10*, 1 (1976), 25–37.

[19] Belytschko, T., and Black, T. Elastic crack growth in finite elements with minimal remeshing. *International journal for numerical methods in engineering 45*, 5 (1999), 601–620.

[20] Benedetti, M., Fontanari, V., Bandini, M., and Taylor, D. Multiaxial fatigue resistance of shot peened high-strength aluminum alloys. *International journal of fatigue 61* (2014), 271–282.

[21] Benedetti, M., Fontanari, V., Santus, C., and Bandini, M. Notch fatigue behaviour of shot peened high-strength aluminium alloys: Experiments and predictions using a critical distance method. *International Journal of Fatigue 32*, 10 (2010), 1600–1611.

[22] Bhatti, N. A., and Wahab, M. A. Fretting fatigue crack nucleation: A review. *Tribology International 121* (2018), 121–138.

[23] Bohórquez, L., Vázquez, J., Navarro, C., and Domínguez, J. On the prediction of the crack initiation path in fretting fatigue. *Theoretical and Applied Fracture Mechanics 99* (2019), 140–146.

[24] Bramhall, R. *Studies in fretting fatigue.* PhD thesis, University of Oxford, 1973.

[25] Cardoso, R., Araújo, J., Ferreira, J., and Castro, F. Crack path simulation for cylindrical contact under fretting conditions. *Frattura ed Integrità Strutturale 10*, 35 (2016), 405–413.

[26] Cardoso, R., Doca, T., Néron, D., Pommier, S., and Araújo, J. Wear numerical assessment for partial slip fretting fatigue conditions. *Tribology International 136* (2019), 508–523.

[27] Cardoso, R., Ferry, B., Montebello, C., Meriaux, J., Pommier, S., and Araújo, J. Study of size effects in fretting fatigue. *Tribology International 143* (2020), 106087.

[28] Cardoso, R. A. *Numerical studies on fretting fatigue.* PhD thesis, Université Paris-Saclay and Universidade de Brasília, 2019.

[29] Cardou, A. Fretting fatigue under spectrum loading application to overhead electrical conductors: a literature review. *Université Laval - Department of Mechanical Engineering* (2002), 15.

[30] Carpinteri, A., Spagnoli, A., and Vantadori, S. Multiaxial fatigue assessment using a simplified critical plane-based criterion. *International Journal of Fatigue 33*, 8 (2011), 969–976.

[31] Cattaneo, C. Sul contatto di due corpi elasticie: Distribution locale degli sforzi. *Reconditi dell Academia Nazionale die Lincei 27* (1938), 474–478.

[32] Cattaneo, C. Sul contatto de due corpi elastici: Distribuzione locale deglisforzi. *Rendiconti dell'Accademia nazionale dei Lincei 6* (1996), 342–349.

[33] Chaboche, J.-L. Continuum damage mechanics: Part ii—damage growth, crack initiation, and crack growth. *Journal of applied mechanics 55*, 1 (1988), 65–72.

[34] Chan, S., Tuba, I., and Wilson, W. On the finite element method in linear fracture mechanics. *Engineering fracture mechanics 2*, 1 (1970), 1–17.

[35] Cheng, W., Cheng, H., Mura, T., and Keer, L. Micromechanics modeling of crack initiation under contact fatigue.

[36] Ciavarella, M. A 'crack-like'notch analogue for a safe-life fretting fatigue design methodology. *Fatigue & Fracture of Engineering Materials & Structures 26*, 12 (2003), 1159–1170.

[37] Ciavarella, M., Dini, D., and Demelio, G. Fretting fatique, surface damage or fatigue phenomonon. In *10th International Conference on Fracture, Honolulu* (2001).

[38] Committee, A. I. H., and for Metals. Heat Treating Division, A. S. *Heat treating*, vol. 4. ASM international, 1991.

[39] Cortez, R., Mall, S., and Calcaterra, J. R. Investigation of variable amplitude loading on fretting fatigue behavior of ti–6al–4v. *International Journal of Fatigue 21*, 7 (1999), 709–717.

[40] Cotterell, B., and Rice, J. Slightly curved or kinked cracks. *International journal of fracture 16*, 2 (1980), 155–169.

[41] Crossland, B. Effect of large hydrostatic pressures on the torsional fatigue strength of an alloy steel. In *Proc. Int. Conf. on Fatigue of Metals* (1956), vol. 138, Institution of Mechanical Engineers London, pp. 12–12.

[42] de Oliveira Miranda, A. C., Meggiolaro, M. A., De Castro, J. T. P., and Martha, L. F. Fatigue life prediction of complex 2d components under mixed-mode variable amplitude loading. *International journal of fatigue 25*, 9-11 (2003), 1157–1167.

[43] Deng, Q., Bhatti, N. A., Yin, X., and Wahab, M. A. The effect of a critical micro-void defect on fretting fatigue crack initiation in heterogeneous material using a multiscale approach. *Tribology International 141* (2020), 105909.

[44] Ding, J., Houghton, D., Williams, E., and Leen, S. Simple parameters to predict effect of surface damage on fretting fatigue. *International Journal of Fatigue 33*, 3 (2011), 332–342.

[45] Ding, J., Leen, S., and McColl, I. The effect of slip regime on fretting wear-induced stress evolution. *International journal of fatigue 26*, 5 (2004), 521–531.

[46] Dini, D., Nowell, D., and Dyson, I. N. The use of notch and short crack approaches to fretting fatigue threshold prediction: Theory and experimental validation. *Tribology international 39*, 10 (2006), 1158–1165.

[47] Doca, T., and Pires, F. A. Finite element modeling of wear using the dissipated energy method coupled with a dual mortar contact formulation. *Computers & Structures 191* (2017), 62–79.

[48] Dowling, N. E. *Mechanical behavior of materials: engineering methods for deformation, fracture, and fatigue.* Prentice Hall international, 1993.

[49] Dowling, N. E. *Mechanical behavior of materials: engineering methods for deformation, fracture, and fatigue.* Pearson, 2012.

[50] E19-19, A. *Standard Test Methods for Rockwell Hardness of Metallic Materials.* 2019.

[51] E466, A. *Standard practice for conducting force controlled constant amplitude axial fatigue tests of metallic materials.* 2015.

[52] E647, A. *Standard Test Method for Measurement of Fatigue Crack Growth Rates.* 1999.

[53] E739-10, A. *Standard Practice for Statistical Analysis of Linear or Linearized Stress-Life and Strain-Life Fatigue Data.* 2015.

[54] E8/E8M-16, A. *Standard Test Methods For Tension Testing Of Metallic Materials.* 2016.

[55] Eden, E., Rose, W., and Cunningham, P. The endurance of metals: experiments on rotating beams at university college, london. *Proceedings of the Institution of Mechanical Engineers 81*, 1 (1911), 839–974.

[56] Endo, K., and Goto, H. Initiation and propagation of fretting fatigue cracks. *Wear 38*, 2 (1976), 311–324.

[57] Erdogan, F., and Sih, G. On the crack extension in plates under plane loading and transverse shear.

[58] Ewing, J. A., and Humfrey, J. Vi. the fracture of metals under repeated alternations of stress. *Philosophical Transactions of the Royal Society of London. Series A, Containing Papers of a Mathematical or Physical Character 200*, 321-330 (1903), 241–250.

[59] Fadel, A. A., Rosa, D., Murça, L., Fereira, J., and Araújo, J. Effect of high mean tensile stress on the fretting fatigue life of an ibis steel reinforced aluminium conductor. *International Journal of Fatigue 42* (2012), 24–34.

[60] Fantetti, A., Tamatam, L., Volvert, M., Lawal, I., Liu, L., Salles, L., Brake, M., Schwingshackl, C., and Nowell, D. The impact of fretting wear on structural dynamics: Experiment and simulation. *Tribology International 138* (2019), 111–124.

[61] Fatemi, A., and Socie, D. F. A critical plane approach to multiaxial fatigue damage including out-of-phase loading. *Fatigue & Fracture of Engineering Materials & Structures 11*, 3 (1988), 149–165.

[62] Findley, W. N. A theory for the effect of mean stress on fatigue of metals under combined torsion and axial load or bending. *Journal of Engineering for Industry 81*, 4 (1959), 301–305.

[63] Fleming, M., Chu, Y., Moran, B., and Belytschko, T. Enriched element-free galerkin methods for crack tip fields. *International journal for numerical methods in engineering 40*, 8 (1997), 1483–1504.

[64] Fouvry, S., Liskiewicz, T., Kapsa, P., Hannel, S., and Sauger, E. An energy description of wear mechanisms and its applications to oscillating sliding contacts. *Wear 255*, 1-6 (2003), 287–298.

[65] Fouvry, S., Nowell, D., Kubiak, K., and Hills, D. Prediction of fretting crack propagation based on a short crack methodology. *Engineering Fracture Mechanics 75*, 6 (2008), 1605–1622.

[66] Gandiolle, C., and Fouvry, S. Fretting fatigue crack propagation rate under variable loading conditions. *Frattura ed Integrità Strutturale 10*, 35 (2016), 232–241.

[67] Giannakopoulos, A., Lindley, T., and Suresh, S. Aspects of equivalence between contact mechanics and fracture mechanics: theoretical connections and a life-prediction methodology for fretting-fatigue. *Acta materialia 46*, 9 (1998), 2955–2968.

[68] Giannakopoulos, A., Lindley, T., Suresh, S., and Chenut, C. Similarities of stress concentrations in contact at round punches and fatigue at notches: implications to fretting fatigue crack initiation. *Fatigue & fracture of engineering materials & structures (Print) 23*, 7 (2000), 561–571.

[69] Giner, E., Sukumar, N., Denia, F., and Fuenmayor, F. Extended finite element method for fretting fatigue crack propagation. *International Journal of Solids and Structures 45*, 22-23 (2008), 5675–5687.

[70] Gordelier, S., and Chivers, T. A literature review of palliatives for fretting fatigue. *Wear 56*, 1 (1979), 177–190.

[71] Gough, H. J., and Pollard, H. The strength of metals under combined alternating stresses. *Proceedings of the institution of mechanical engineers 131*, 1 (1935), 3–103.

[72] Griffith, A. Philosophical transactions of the royal society of london. *Series A, containing papers of a mathematical or physical character 221* (1921), 163–198.

[73] Guillaumin, V., and Mankowski, G. Localized corrosion of 2024 t351 aluminium alloy in chloride media. *Corrosion Science 41*, 3 (1998), 421–438.

[74] Hattori, T., Nakamura, M., and Watanabe, T. Simulation of fretting-fatigue life by using stress-singularity parameters and fracture mechanics. *Tribology international 36*, 2 (2003), 87–97.

[75] Hayashi, K., and Nemat-Nasser, S. Energy-release rate and crack kinking under combined loading.

[76] Henshell, R., and Shaw, K. Crack tip finite elements are unnecessary. *International journal for numerical methods in engineering 9*, 3 (1975), 495–507.

[77] Hertz, H. Journal fur die rein und angewandte mathematik (crelle's journal). *Ueber die Beruhrung fester elastischer Korper 92* (1882), 156–171.

[78] Hertzberg, R. W., and Hauser, F. E. Deformation and fracture mechanics of engineering materials.

[79] Hertzberg, R. W., and Manson, J. A. *Fatigue of engineering plastics.* Academic press, 1980.

[80] Hills, D., and Nowell, D. Mechanics of fretting fatigue. solid mechanics and its applications vol. 30, 1994.

[81] Hills, D. A. Mechanics of fretting fatigue. *Wear 175*, 1-2 (1994), 107–113.

[82] Hills, D. A., and Nowell, D. *Mechanics of fretting fatigue.* Dordrecht: Kluwer Academic Publishers, 1994.

[83] Hojjati Talemi, R. *Numerical modelling techniques for fretting fatigue crack initiation and propagation.* PhD thesis, Ghent University, 2014.

[84] Hojjati-Talemi, R., Wahab, M. A., De Pauw, J., and De Baets, P. Prediction of fretting fatigue crack initiation and propagation lifetime for cylindrical contact configuration. *Tribology International 76* (2014), 73–91.

[85] Inglis, C. E. *Applied mechanics for engineers.* CUP Archive, 1963.

[86] Irwin, G. *Fracture encyclopedia of physics VI* (1958).

[87] Johnson, K. L. *Contact mechanics.* Cambridge university press, 1987.

[88] Jordano, G., Navarro, C., Vázquez, J., and Domínguez, J. Measuring wear in a fretting test with a confocal microscope. In *Key Engineering Materials* (2018), vol. 774, Trans Tech Publ, pp. 461–466.

[89] Kantimathi, A., and Alic, J. The effects of periodic high loads on fretting fatigue. *Journal of Engineering Materials and Technology 103*, 3 (1981), 223–228.

[90] Kim, K., and Yoon, M.-J. Fretting fatigue simulation for aluminium alloy using cohesive zone law approach. *International Journal of Mechanical Sciences 85* (2014), 30–37.

[91] Kinyon, S. E., and Hoeppner, D. W. Spectrum load effects on the fretting behavior of ti-6al-4v. In *Fretting Fatigue: Current Technology and Practices.* ASTM International, 2000.

[92] Kondo, Y., Sakae, C., Kubota, M., Kitahara, H., and Yanagihara, K. Fretting fatigue under variable loading below fretting fatigue limit. *Fatigue & Fracture of Engineering Materials & Structures 29*, 3 (2006), 191–199.

[93] Kouanga, C., Jones, J., Revill, I., Wormald, A., Nowell, D., Dwyer-Joyce, R., Araújo, J., and Susmel, L. On the estimation of finite lifetime under fretting fatigue loading. *International Journal of Fatigue 112* (2018), 138–152.

[94] Lamacq, V., Dubourg, M., and Vincent, L. A theoretical model for the prediction of fretting fatigue crack initial growth angles and sites. *Tribology Int 30*, 6 (1997), 391–400.

[95] Lapidus, L., and Pinder, G. F. *Numerical solution of partial differential equations in science and engineering.* John Wiley & Sons, 2011.

[96] Lazzarin, P., Tovo, R., and Meneghetti, G. Fatigue crack initiation and propagation phases near notches in metals with low notch sensitivity. *International Journal of Fatigue 19*, 8-9 (1997), 647–657.

[97] Lemaitre, J. A continuous damage mechanics model for ductile fracture. *Journal of engineering materials and technology 107*, 1 (1985), 83–89.

[98] Li, X., Zuo, Z., and Qin, W. A fretting related damage parameter for fretting fatigue life prediction. *International journal of Fatigue 73* (2015), 110–118.

[99] Lindley, T. Fretting fatigue in engineering alloys. *International journal of fatigue 19*, 93 (1997), 39–49.

[100] Lykins, C. D., Mall, S., and Jain, V. An evaluation of parameters for predicting fretting fatigue crack initiation. *International Journal of Fatigue 22*, 8 (2000), 703–716.

[101] Martín, V., Vázquez, J., Navarro, C., and Domínguez, J. Fretting-fatigue analysis of shot-peened al 7075-t651 test specimens. *Metals 9*, 5 (2019), 586.

[102] Mary, C. *Simulation expérimentale de l'usure du contact aube-disque de compresseur sous sollicitations de fretting.* PhD thesis, Ecole Centrale de Lyon, 2009.

[103] Massingham, M., and Irving, P. The effect of variable amplitude loading on stress distribution within a cylindrical contact subjected to fretting fatigue. *Tribology international 39*, 10 (2006), 1084–1091.

[104] McColl, I., Ding, J., and Leen, S. Finite element simulation and experimental validation of fretting wear. *Wear 256*, 11-12 (2004), 1114–1127.

[105] McDowell, J. Fretting corrosion tendencies of several combinations of materials. In *Symposium on fretting corrosion* (1952), ASTM International.

[106] Melenk, J. M., and Babuška, I. The partition of unity finite element method: basic theory and applications. In *Research Report/Seminar für Angewandte Mathematik* (1996), vol. 1996, Eidgenössische Technische Hochschule, Seminar für Angewandte Mathematik.

[107] Mindlin, R. D. Compliance of elastic bodies in contact. *J. Appl. Mech., ASME 16* (1949), 259–268.

[108] Miner, M. J. appl. mech. *Cumulative damage in fatigue 12* (1945), 159.

[109] Miner, M. A. Cumulative damage in fatigue. *Journal of Applied Mechanics 12* (1945), 159–164.

[110] Moës, N., Dolbow, J., and Belytschko, T. A finite element method for crack growth without remeshing. *International journal for numerical methods in engineering 46*, 1 (1999), 131–150.

[111] Mohrbacher, H., Celis, J.-P., and Roos, J. Laboratory testing of displacement and load induced fretting. *Tribology international 28*, 5 (1995), 269–278.

[112] Moran, B., and Shih, C. A general treatment of crack tip contour integrals. *International journal of fracture 35*, 4 (1987), 295–310.

[113] Muskhelishvili, N. Some basic problems of mathematical theory of elasticity, published in russian in (1933). *English translation, P. Noordhoff and Co* (1953).

[114] MUTOH, Y., TANAKA, K., and KONDOH, M. Fretting fatigue in jis s45c steel under two-step block loading: Solid-mechanics, strength of materials. *JSME international journal 30*, 261 (1987), 386–393.

[115] MUTOH, Y., TANAKA, K., and KONDOH, M. Fretting fatigue in sup9 spring steel under random loading. *JSME international journal. Ser. 1, Solid mechanics, strength of materials 32*, 2 (1989), 274–281.

[116] Navarro, C., Muñoz, S., and Dominguez, J. On the use of multiaxial fatigue criteria for fretting fatigue life assessment. *International Journal of fatigue 30*, 1 (2008), 32–44.

[117] Navarro, C., Vázquez, J., and Domínguez, J. Nucleation and early crack path in fretting fatigue. *International Journal of fatigue 100* (2017), 602–610.

[118] Neu, R. W., Pape, J. A., and Swalla, D. R. Methodologies for linking nucleation and propagation approaches for predicting life under fretting fatigue. In *Fretting fatigue: current technology and practices.* ASTM International, 2000.

[119] Neuber, H. Forschg ing-wes. *Bd 7* (1936), 271.

[120] Newman Jr, J., Phillips, E. P., and Swain, M. Fatigue-life prediction methodology using small-crack theory. *International Journal of fatigue 21*, 2 (1999), 109–119.

[121] Nishihara, T., Kawamoto, M., et al. The strength of metals under combined alternating bending and torsion with phase difference. *Memories of the College of Engineering, Kyoto Imperial University 11*, 85 (1945), 112.

[122] Nishioka, K., and Hirakawa, K. Fundamental investigations of fretting fatigue:(part 2, fretting fatigue testing machine and some test results). *Bulletin of JSME 12*, 50 (1969a), 180–187.

[123] Nishioka, K., and Hirakawa, K. Fundamental investigations of fretting fatigue: part 3, some phenomena and mechanisms of surface cracks. *Bulletin of JSME 12*, 51 (1969b), 397–407.

[124] Nishioka, K., and Hirakawa, K. Fundamental investigations of fretting fatigue: Part 4, the effect of mean stress. *Bulletin of JSME 12*, 51 (1969c), 408–414.

[125] Nishioka, K., and Hirakawa, K. Fundamental investigations of fretting fatigue:(part 5, the effect of relative slip amplitude). *Bulletin of JSME 12*, 52 (1969d), 692–697.

[126] Nishioka, K., and Kenji, H. Fundamental investigations of fretting fatigue: Part 6, effects of contact pressure and hardness of materials. *Bulletin of JSME 15*, 80 (1972), 135–144.

[127] Nowell, D. *An analysis of fretting fatigue.* PhD thesis, University of Oxford, 1988.

[128] Nowell, D., Dini, D., and Hills, D. Recent developments in the understanding of fretting fatigue. *Engineering Fracture Mechanics 73*, 2 (2006), 207–222.

[129] Palmgren, A. Die lebensdauer von kugellargern. *Zeitshrift des Vereines Duetsher Ingenieure 68*, 4 (1924), 339.

[130] Paris, P., and Erdogan, F. A critical analysis of crack propagation laws.

[131] Peterson, R. Methods of correlating data from fatigue tests of stress concentration specimens. *Stephen Timoshenko Anniversary Volume* (1938), 179.

[132] Pinto, A. L., Araújo, J. A., and Talemi, R. Effects of fretting wear process on fatigue crack propagation and life assessment. *Tribology International 156* (2021), 106787.

[133] Pinto, A. L., Cardoso, R., Talemi, R., and Araújo, J. A. Fretting fatigue under variable amplitude loading considering partial and gross slip regimes: Numerical analysis. *Tribology International 146* (2020), 106199.

[134] Poncelet, J. V. *Introduction à la mécanique industrielle, physique ou expérimentale.* Thiel, 1839.

[135] Rajasekaran, R., and Nowell, D. Fretting fatigue in dovetail blade roots: Experiment and analysis. *Tribology International 39*, 10 (2006), 1277–1285.

[136] Rice, J. R. A path independent integral and the approximate analysis of strain concentration by notches and cracks.

[137] Rice, J. R., and Rosengren, G. Plane strain deformation near a crack tip in a power-law hardening material. *Journal of the Mechanics and Physics of Solids 16*, 1 (1968), 1–12.

[138] Rizzo, F. J. An integral equation approach to boundary value problems of classical elastostatics. *Quarterly of applied mathematics 25*, 1 (1967), 83–95.

[139] Roebben, G., Steen, M., Bressers, J., and Van der Biest, O. Mechanical fatigue in monolithic non-transforming ceramics. *Progress in materials science 40*, 4 (1996), 265–331.

[140] Ruiz, C., Boddington, P., and Chen, K. An investigation of fatigue and fretting in a dovetail joint. *Experimental mechanics 24*, 3 (1984), 208–217.

[141] Ruiz, C., and Chen, K. C. Life assessment of dovetail joints between blades and discs in aero-engines. *Mechanical Engineering Publications,* (1986), 187–194.

[142] SÁ, M. V. C. Estudo sobre o comportamento em fadiga da liga de alumínio 7050-t7451 na presença de entalhe e carregamento axial-torcional.

[143] Schütz, W. A history of fatigue. *Engineering fracture mechanics 54*, 2 (1996), 263–300.

[144] Shih, C., Moran, B., and Nakamura, T. Energy release rate along a three-dimensional crack front in a thermally stressed body. *International Journal of fracture 30*, 2 (1986), 79–102.

[145] Sines, G. Failure of materials under combined repeated stresses with superimposed static stresses. Tech. rep., California. Univ., Los Angeles, 1955.

[146] Smith, R., Watson, P., and Topper, T. A stress-strain parameter for the fatigue of metals. *Journal of Materials 5*, 4 (1970), 767–778.

[147] Socie, D. Multiaxial fatigue damage models. *Journal of Engineering Materials and Technology 109*, 4 (1987), 293–298.

[148] Socie, D. Critical plane approaches for multiaxial fatigue damage assessment. In *Advances in multiaxial fatigue*. ASTM International, 1993.

[149] Socie, D., and Marquis, G. B. *Multiaxial fatigue.* Society of Automotive Engineers Warrendale, PA, 2000.

[150] STARKE JR, E., and HORNBOGEN, E. Precipitation hardening: From alfred hilm to the present. *HIRSCH, J.; SKROTZKI, B.; GOTTSTEIN, G. Aluminum Alloys, Their Physical and Mechanical Properties. Weinheim: Wiley-VCH 1* (2008).

[151] Suresh, S. Mechanics and micromechanisms of fatigue crack growth in brittle solids. *International journal of fracture 42*, 1 (1990), 41–56.

[152] Suresh, S. *Fatigue of materials.* Cambridge university press, 1998.

[153] Susmel, L. *Multiaxial notch fatigue.* Elsevier, 2009.

[154] Susmel, L., and Lazzarin, P. A bi-parametric wöhler curve for high cycle multiaxial fatigue assessment. *Fatigue & Fracture of Engineering Materials & Structures 25*, 1 (2002), 63–78.

[155] Susmel, L., and Taylor, D. A novel formulation of the theory of critical distances to estimate lifetime of notched components in the medium-cycle fatigue regime. *Fatigue & Fracture of Engineering Materials & Structures 30*, 7 (2007), 567–581.

[156] Susmel, L., and Taylor, D. On the use of the theory of critical distances to predict static failures in ductile metallic materials containing different geometrical features. *Engineering Fracture Mechanics 75*, 15 (2008), 4410–4421.

[157] Szolwinski, M. P., and Farris, T. N. Mechanics of fretting fatigue crack formation. *Wear 198*, 1-2 (1996), 93–107.

[158] Talemi, R. H. Numerical measures of non-proportionality degree in incomplete contact subjected to fretting fatigue loading. *Theoretical and Applied Fracture Mechanics 90* (2017), 33–42.

[159] Tanaka, K. Engineering formulae for fatigue strength reduction due to crack-like notches. *International Journal of Fracture 22*, 2 (1983), R39–R46.

[160] Taylor, D. Geometrical effects in fatigue: a unifying theoretical model. *International Journal of Fatigue 21*, 5 (1999), 413–420.

[161] Taylor, D. The theory of critical distances. *Engineering Fracture Mechanics 75*, 7 (2008), 1696–1705.

[162] Taylor, D., and Wang, G. The validation of some methods of notch fatigue analysis. *Fatigue & fracture of engineering materials & structures 23*, 5 (2000), 387–394.

[163] Tomlinson, G. The rusting of steel surfaces in contact. *Proceedings of the Royal Society of London. Series A, Containing Papers of a Mathematical and Physical Character 115*, 771 (1927), 472–483.

[164] Troshchenko, V., Dragan, V., and Semenyuk, S. Fatigue damage accumulation in aluminium and titanium alloys subjected to block program loading under conditions of stress concentration and fretting. *International journal of fatigue 21*, 3 (1999), 271–279.

[165] Vantadori, S., Almeida, G. M. J., Fortese, G., Pessoa, G. C. V., and Araujo, J. A. Early fretting crack orientation by using the critical plane approach. *International Journal of Fatigue 114* (2018), 282–288.

[166] Vantadori, S., Fortese, G., Ronchei, C., and Scorza, D. A stress gradient approach for fretting fatigue assessment of metallic structural components. *International Journal of Fatigue 101* (2017), 1–8.

[167] Vázquez, J., Navarro, C., and Domínguez, J. Experimental results in fretting fatigue with shot and laser peened al 7075-t651 specimens. *International Journal of Fatigue 40* (2012), 143–153.

[168] Vingsbo, O., and Söderberg, S. On fretting maps. *Wear 126*, 2 (1988), 131–147.

[169] Warlow-Davies, E. Fretting corrosion and fatigue strength: brief results of preliminary experiments. *Proceedings of the Institution of Mechanical Engineers 146*, 1 (1941), 32–38.

[170] Waterhouse, R. . Fretting fatigue. *International materials reviews 37*, 1 (1992), 77–98.

[171] Waterhouse, R. Fretting wear. *Wear 100*, 1-3 (1984), 107–118.

[172] Whitney, J. M., and Nuismer, R. Stress fracture criteria for laminated composites containing stress concentrations. *Journal of composite materials 8*, 3 (1974), 253–265.

[173] Withey, P. A. Fatigue failure of the de havilland comet i. *Engineering failure analysis 4*, 2 (1997), 147–154.

[174] Wright, G., and O'Connor, J. The influence of fretting and geometric stress concentrations on the fatigue strength of clamped joints. *Proceedings of the Institution of Mechanical Engineers 186*, 1 (1972), 827–835.

[175] Zabala, A., Infante-García, D., Giner, E., Goel, S., Endrino, J. L., and Llavori, I. On the use of the theory of critical distances with mesh control for fretting fatigue lifetime assessment. *Tribology International 142* (2020), 105985.

[176] Zhao, T., and Jiang, Y. Fatigue of 7075-t651 aluminum alloy. *International Journal of Fatigue 30*, 5 (2008), 834–849.

[177] Zienkiewicz, O. C., and Taylor, R. L. The finite element method, 4th edn., vol. 1. *Basic Formulation and Linear* (1989).

[178] Zuo, P., Srinivasan, D. V., and Vassilopoulos, A. P. Review of hybrid composites fatigue. *Composite Structures 274* (2021), 114358.

Curriculum Vitae

Personal

Name: André Luis Pinto
Date and place of birth: 21st of January 1993, Goianésia, Brazil
Citizenship: Brazilian
Email: andreluis.pinto@kuleuven.be, andreluiseng.mecanica@gmail.com

Education

2016-2017: Master of Mechanical Science,
University of Brasilia, UnB
2011-2015: Bachelor of Mechanical Engineering,
Evangelical University of Goiás, UniEVANGÉLICA

Publications

A.1 A1 - Peer reviewed journal publications

1. **Pinto, A. L.**, Cardoso, R. A., Talemi, R., Araújo, J. A. (2020). Fretting fatigue under variable amplitude loading considering partial and gross slip regimes: Numerical analysis. *Tribology International*, 146, 106199.
2. **Pinto, A. L.**, Araújo, J. A., Talemi, R. (2021). Effects of fretting wear process on fatigue crack propagation and life assessment. *Tribology International*, 156, 106787.
3. **Pinto, A. L.**, Talemi, R., Araújo, J. A. (2022). Fretting fatigue total life assessment including wear and a varying critical distance. *International Journal of Fatigue*, 156, 106589.
4. **Pinto, A. L.**, Cardoso, R. A., Talemi, R., Araújo, J. A. (2022). Early crack orientation prediction methods under fretting fatigue loading including wear effects. *International Journal of Fatigue*, 161, 106893.
5. **Pinto, A. L.**, Talemi, R., Araújo, J. A. (2022). Fretting fatigue under variable amplitude loading considering partial slip regime: Experimental and numerical analysis. **In progress**.

A.2 P1 - Peer reviewed Publications in conference proceedings

1. **Pinto, A. L.**, Cardoso, R. A., Talemi, R., Araújo, J. A. (2022). Early crack orientation prediction methods under fretting fatigue loading. *Procedia Structural Integrity*, 39, 409-418.

A.3 C1 - Publications in conference proceedings

1. **Pinto, A. L.**, Cardoso, R. A., Talemi, R., Araújo, J. A. (2019). Fretting fatigue under variable amplitude loading considering partial and gross slip regimes: Numerical analysis. *9th International Symposium on Fretting Fatigue (ISFF9)*, Seville.
2. Talemi, R., **Pinto, A. L.**, Araújo, J. A. (2020). Effects of tribological behaviour on fatigue fracture of materials. *2nd Korea-Tribology International Symposium (K-TRIB2020)*, Seoul, Korea.
3. **Pinto, A. L.**, Cardoso, R. A., Talemi, R., Araújo, J. A. (2022). Early crack orientation prediction methods under fretting fatigue loading. *7th International Conference on Crack Paths (CP2021)*, online.
4. **Pinto, A. L.**, Talemi, R., Araújo, J. A. (2022). Fretting fatigue under variable amplitude loading considering partial slip regime: Numerical/experimental analysis. *10th International Symposium on Fretting Fatigue (ISFF10)*, Leuven.

FACULTY OF ENGINEERING TECHNOLOGY
DEPARTMENT OF MATERIALS ENGINEERING
METALS PERFORMANCE INNOVATION LABORATORY
Gebroeders De Smetstraat 1
B-9000 Ghent
andreluis.pinto@kuleuven.be
http://www.mtm.kuleuven.be/onderzoek/scalint/ndt